A vector based approach for high frequency prospective correction of rigid body motion in Magnetic Resonance Imaging (MRI).

Adam Marthinus Johannes van Niekerk

Department of Human Biology

University of Cape Town

This thesis is submitted for the degree of

Doctor of Philosophy in Biomedical Engineering

February 2019

I would like to dedicate this thesis to Jennifer Couperthwaite, who thankfully decided to become Mrs van Niekerk (my wife) late in 2017, and my fantastic parents.

Declaration

I hereby declare that the work on which this thesis is based is my original work (except where acknowledgements indicate otherwise) and that neither the whole work nor any part of it has been, is being, or is to be submitted for another degree in this or any other university. I authorise the University to reproduce for the purpose of research either the whole or any portion of the contents in any manner whatsoever.

I confirm that I have been granted permission by the University of Cape Town's Doctoral Degrees Board to include the following publication in my thesis, and where co-authorships are involved, my co-authors have agreed that I may include the publication:

- A method for measuring orientation within a magnetic resonance imaging scanner using gravity and the static magnetic field (VectOrient), [with permission from Andre van der Kouwe and Ernesta Meintjes, © 2017 IEEE, January].

Signed by candidate

Adam Marthinus Johannes van Niekerk
February 2019

Preface

The ideas presented in this thesis originate from my background in inertial measurement. In my final year of undergraduate studies, I built a stabiliser for a light-weight camera where one of the most difficult challenges was to build an actuator fast enough to correct small vibrations. Upon completing this project and starting my masters in biomedical engineering, I attended an introductory lecture on Magnetic Resonance Imaging (MRI). I was immediately interested in translating what I had learnt into MRI. The ‘camera’ (MRI scanner) was stationary, but had this ‘magical’ ability to view the subject from anywhere. This was mechanically simple and the static magnetic field would be an ideal vector reference. This would enable fast and reliable orientation estimates independent of the imaging pulse sequence.

Ernesta Meintjes, who gave the introductory lecture, (after some convincing) agreed to supervise my project and has expertly guided me ever since. This initial observation allowed me to develop a working prototype for measuring subject orientation within a year from when my coursework had ended. Interfacing this device with the scanner was then implemented with help from my co-supervisor, Andre van der Kouwe, during a research visit to the Anthinoula A. Martinos centre in Boston. Measuring position while maintaining the advantages of the new orientation measurement method was, however, more challenging and my project soon evolved from a masters into a doctorate, culminating in this thesis.

This thesis is structured around three independent articles that are preceded by an introduction that outlines and motivates this research, and proceeded by a conclusion that discusses the objectives that were achieved and describes some potential future developments. I drafted all the articles, sourced the components, conceptualised the ideas, designed the printed circuit boards, fabricated/soldered all the devices, performed all the experiments and analysed all the data. The co-authors (Ernesta and Andre) gave scientific and editorial input.

The second chapter was published in the IEEE Transaction in Medical Imaging (TMI) early in 2017. This publication describes the development of my first prototype and demonstrates it’s potential application to prospective motion correction. I developed the filter used to combine the measurements as well as performed all the experiments. Andre taught me a great deal about sequence development and let me build on an ethernet client he had previously written to feedback orientation data to the scanner. Ernesta and Andre helped me in the experimental design used to validate this new method.

After completing this work I spent many hours working on measuring translation using fast navigators. In the end these attempts were unsuccessful, but I learnt a great deal about the formation of the MR signal, multiple receive coils and the gradients. While I was in Boston, Andre, Paul Wighton and Dylan Tisdall were working on an approach that uses pickup coils to measure subject pose. It would take me another year to realise exactly how complementary my orientation measurement technique is to this method. The drawbacks of synchronising to the imaging pulse sequence and complex calibration seemed insurmountable at the time, especially because I was trying to find an easy-to-use, wireless solution.

The article presented in the third chapter shows how these challenges were overcome with a novel hybrid device that is capable of wireless synchronisation to the imaging pulse sequence. This manuscript has been submitted to the IEEE-TMI and is currently under review.

The manuscript in the fourth chapter refines this method. For this work I developed a linear *Kalman* filter to track system and sensor biases in real time enabling cable free prospective motion correction of a gradient echo pulse sequence without any scanner specific calibration. This article presents *in vivo* data and forms a combined validation of the ideas developed in the previous two chapters. We plan on submitting this article to the journal of Magnetic Resonance in Medicine (MRM) in the near future.

To keep this document short and concise I have excluded detailed descriptions of the device designs and only included aspects that aren’t obvious to someone trained in this field. For all filters/algorithms I have drawn flow charts summarising their implementation, these figures represent the code exactly as it has been implemented on the embedded devices.

Acknowledgements

I would like to acknowledge my supervisors Ernesta and Andre, for helping me abandon my bad ideas and believing in the better ones. Andrew Wilkinson for letting me use his lab's network analyser, and teaching me the basics of high frequency RF (when I clearly had no idea). Sam Ginsberg for pointing me in the direction of good printed circuit board manufacturers and letting me use some of his lab's soldering equipment, especially the stereoscope. Dylan Tisdall for the use of some of his abstraction layers, his quaternion class and helpful discussions. Paul Wighton for helping me get to grips with sequence programming and some great advice. And the (ISMRM) motion correction study group, for all that I have learnt from its many experts. Last but not least to Jennifer, for her patience and support, especially during those periods when I was simultaneously debugging hardware, firmware and software (where the success correlated well with my mood).

I would also like to acknowledge the organisations that funded this research. The National Institutes of Health under grants R01HD085813, R01HD093578, R21AG046657, R01HD071664, R21MH096559 and R21AA020037, the Bertarelli Foundation, the NRF/DST through the South African Research Chairs Initiative and the University of Cape Town through the RCIPS Explorer fund EX15-009 and the Sir Robert Kotze Fellowship.

Abstract

Magnetic Resonance Imaging (MRI) is remarkable in that it is possible to obtain image resolutions much smaller than the wavelength of the radiated signal. This is achieved through the use of specialised gradient coils that linearly manipulate the magnitude of the magnetic field within the imaging volume. The instantaneous signal received from the subject represents a periodically varying map based on the duration and magnitude (moment) of the previously applied gradient fields. Representing an object as the sum of periodic maps is difficult and as a result many unique gradient moments are required to form an image. When the subject moves the periodic maps are no longer coherent and the constructive/destructive interference becomes invalid. The artefacts are dependent on how and when motion occurred, and manifest as ghosting, ringing and blurring of the image. This thesis describes a novel approach to measuring and correcting for motion as the data are acquired. A small device was constructed that combines observations from a magnetometer (static magnetic field [z]) and an accelerometer (earth's gravitational field [y]) with an angular rate sensor to determine its orientation with respect to the imaging coordinate frame (VectOrient). It was precise enough to track the subject's heart beat and breathing and accurate to within one degree. A gradient field probe was then designed for position encoding. The probe measured the rate of change of the gradient magnetic fields using three mutually orthogonal pickup coils. Assuming linear gradients and using Maxwell's equations, with negligible rates of change of curl and divergence, it was possible to accurately model the three dimensional vector fields that the gradients produce, eliminating the need for a laborious manual calibration. Sub-microsecond synchronisation was achieved by detecting radio frequency pulses in the imaging sequence with a small resonant circuit. This combined with a 2.4 GHz radio link enabled the probe to be wireless. Finally, the pickup coil observations were combined with the vector based orientation estimates and the gradient field model to achieve efficient multidimensional position, orientation and inter-gradient-delay encoding with a 880 μs pulse sequence insert. The Wireless Radio frequency triggered Acquisition Device (WRAD) tracks involun-

tary and deliberate subject motion, improving image quality without scanner specific calibration.

Table of contents

List of figures

List of tables

Chapter 1

Introduction

1.1 Motivation

Magnetic Resonance Imaging (MRI) offers unique contrasts that enable better insight into patient disease without the risks associated with ionising radiation. This versatility and safety has allowed researchers to better understand the effects of disease on the form and function of the human body. This is particularly true for the study of the human brain where MRI has better spatial sensitivity than electroencephalography (EEG) for the study of function and better soft tissue contrast than computed tomography (CT) for morphometry. In this research we focus on the measurement and correction of rigid body head motion. In all imaging modalities a change in subject pose during the exposure/encoding time results in image artefacts. These artefacts are more complex in MRI because the image is encoded as a multi-dimensional spectrum. The problem is exacerbated by the fact that the encoding required to produce images with sufficient spatial resolution for analysis, takes of the order of minutes. As a result MRI is vulnerable to motion, causing rescan rates as high as 19.8 % in a clinical setting [1]. Methods of reducing the prevalence of motion artefacts in MRI can be generalised into the three complementary categories of preparation, acceleration and correction. Preparation is dependent on how each subject responds to the MRI scanner environment and is difficult to control. Non subjective methods such as constricting or sedating the subject are typically avoided (especially in research settings), because of the associated risks. Accelerating image acquisitions has been achieved with advances such a parallel imaging (using receive coil sensitivity profiles for image encoding), multi-band imaging (acquiring multiple slices simultaneously) and multi-contrast imaging (combining multiple sequences into one continuous acquisition). Improvements in scanner performance, particularly of the gradient coils and static magnetic field, have also resulted in notably faster image encoding. This acceleration is however not always used to reduce scan time. Clinicians and scientists often opt to increase the spatial resolution of image acquisitions resulting in only slightly shorter acquisition times. With higher spatial resolutions the correction of subject motion becomes even more important because involuntary motion associated with breathing and cushion relaxation could degrade image quality, and in some cases the acceleration technique makes the image reconstruction more susceptible to motion. Many methods exist for detecting and correcting motion, however few have made an impact on clinical routine.

1.1.1 Retrospective and Prospective motion correction

In clinical MRI one of the most successful techniques for correction motion is PROPELLER [2]. The centre of k-space is oversampled, resulting in a trade-off between motion robustness and scan time. This method is only applicable to a few 2D imaging sequences and can fail for strong through-plane motion. Recent work has extended this idea to 3D by taking advantage of simultaneous multi slice acceleration [3] to achieve higher effective resolution in a shorter time than a traditional 3D RARE acquisition. Alternatively researchers have proposed interleaving lower resolution acquisitions (*navigators*) with the imaging pulse sequence. Navigator methods are well suited to acquisitions with sequence 'dead-time' such as the magnetisation prepared rapid gradient echo (MPRAGE) pulse sequence, where 3D FatNavs (2 mm, isotropic, 1152 ms) have been used to create exceptionally high quality images at 7 T by detecting and correcting the small involuntary drift of well trained subjects without increasing scan time [4]. In these methods the images are corrected retrospectively (after the image was acquired) and as a result have very little impact on the imaging pipeline. The original and motion corrected images are available, which is important for clinical imaging (this guarantees that image quality is never degraded). In prospective motion correction the imaging pulse sequence is updated in real time to 'follow' the subject. Pose measurements that are fed back to the scanner are treated as the true subject pose, any variance in the measurements will irrevocably degrade image quality. Prospective motion correction does however have advantages over retrospective techniques in that more severe motion can be corrected for, this is especially important in slab/slice selective pulse sequences where motion can influence the tissue magnetisation history. It is also important in spectroscopy where the anatomical region from which data are collected changes and there is no way to tell, since no images are collected during MRS. Also, in measurements where the signals are spatially encoded to achieve some sort of weighting (such as diffusion) - incorrect weighting of the signal would then cause the measurements to be erroneous. The signal that would have been achieved with the correct weighting cannot be determined by correcting the position retrospectively. Navigators can be used for prospective motion correction by measuring changes in subject pose (PROMO [5] - 45 ms, vNav [6] - 275 ms) and the homogenity of the static magnetic field [7] relative to a reference acquisition. These approaches have limited temporal resolution because they take relatively long to acquire, however they can be highly accelerated through parallel imaging techniques by taking advantage of the shell-like nature of the fat signal from the head (FatNavs) with pulse durations as short as 6.4 ms reported with collapsed-FatNavs [8]. The sequence dependence of navigators and their relationship with the tissue magnetisation does however make predicting their precision challenging. The highly optimised navigator pulse series also results in rapid changes in the tone of the pulse sequence which can be unsettling to some subjects.

1.1.2 Marker based methods

The work of this thesis falls under the category of marker based techniques. One of the earliest developments in this field was to construct small RF coils that surround a sample and perform localised MR experiments [9]. By determining the precession frequency of the sample for 3 unique gradient combinations the location of the marker within the imaging volume could be determined. To measure changes in orientation, 3 markers were rigidly constrained relative to each other and a least squares fit is used to determine the rotation between states [10]. This affects the minimum size of the apparatus the subject must wear. Although wireless markers have been developed [11] that magnetically couple to the receive coils, an independent RF transmit is important for realising sequence independence [12], which requires cables in the scanner bore and the associated risks. Low-cost wireless markers can be tracked using optical methods [13] that are sequence independent, with recent developments showing marker-less motion tracking. Introducing a camera into the MR environment does however pose significant hardware design challenges such as cross-calibration and line-of-sight.

1.1.3 The research gap

Existing approaches that use external hardware allow for exceptionally precise and accurate subject pose measurement at temporal resolutions typically not possible using navigator based methods, however this often comes at the cost of increased complexity that does not translate well into a clinical setting. The need for high precision is important to ensure the data feedback to the scanner does not degrade image quality [14]. On the other hand, subject motion is small in the confined space of a receive coil, and as a result the accuracy of the measurements is less important [15] and could be traded for ease of use. We therefore identified the need for a single wireless marker that can be placed anywhere on the subject and used immediately, to precisely determine subject pose, without calibration. If motion correction is not required the scanner should be returned to its original state easily, the marker should therefore be a 'stand-alone' marker that does not require any connections to the MRI scanner hardware or external data acquisition device.

To achieve this we proposed a battery powered marker that uses vector observations of the exceptionally stable static magnetic and earth's gravitational fields to determine orientation to high precision independently of the pulse sequence. Although determining position with gradient field spatial encoding would require no scanner specific calibration, measuring the superposition of the gradient fields on the static magnetic field requires exceptionally sensitive sensors/electronics that are challenging to make wireless [16]. We therefore measure the rate of change of the gradient fields using pickup coils. This way the three dimensional gradient encoding is visible, reducing the pulse diversity required for position encoding (no longer require three unique gradient combinations). Although existing pickup coil implementations are wired and require complex calibration [17], we predict that the vector based orientation could enable a calibration free implementation because analysing the signal is simplified in a known measurement frame. Interpreting gradient waveforms requires synchronisation to the pulse sequence time domain, which can be achieved by detecting the RF transmit pulses in the imaging pulse sequence with a small resonant circuit. Finally the smart marker could communicate the measurements out of the scanner bore using a 2.4 GHz radio link that is far from the frequency bands used in MRI allowing for a wireless implementation.

1.2 Document Overview

This thesis is written in the form of 3 articles (one chapter for each). Although these articles are written so that they can stand alone, they have a logical flow. The first chapter is an original published paper that describes vector based orientation tracking from a single marker. The second article introduces wireless synchronisation and digitisation of the rate of change of the gradient waveforms. The final article combines vector based orientation with the gradient slew vector measurements using a linear field model and a Kalman filter to enable prospective motion correction. Each article answers its own research questions, where the success of the main ideas are mandatory to proceed to the next question (article). The logical flow therefore follows as shown in Figure 1.1.

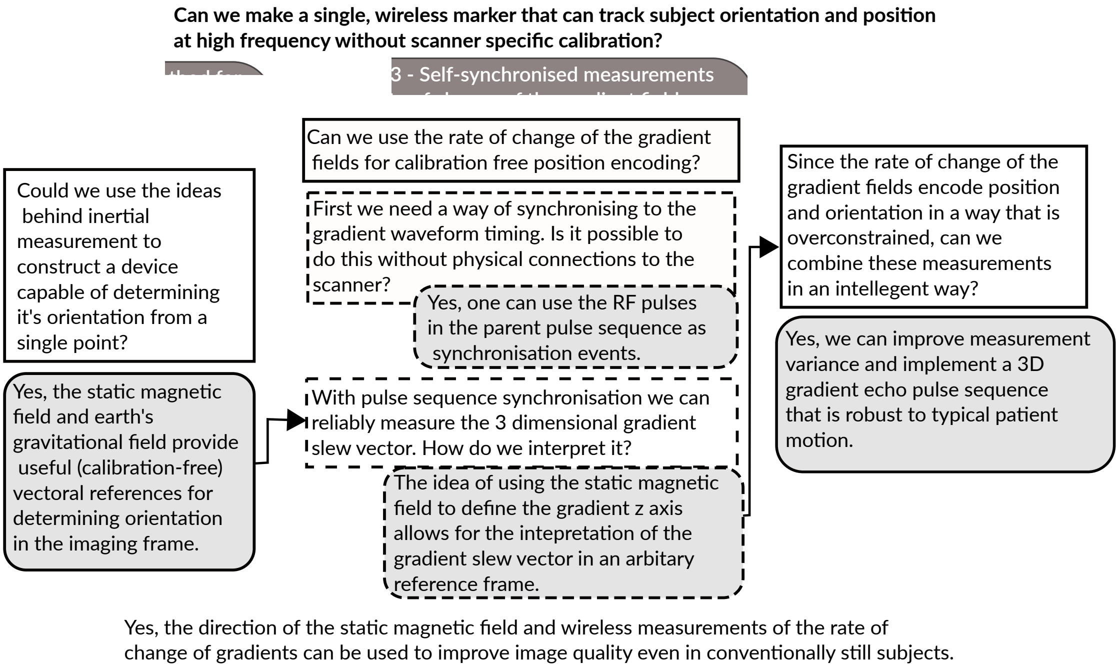

Fig. 1.1 An overview of each chapter and the core research questions answered in this work.

1.3 Background

For the following section a notation for rotation matrix multiplication, in a right handed coordinate system, is introduced. A pre-multiplication of a vector (v) in an arbitrary frame B by the rotation matrix ${}^{A}_{B}\mathbf{R}$ therefore transforms the vector into frame A:

$$ {}^{A}_{B}\mathbf{R}\,{}^{B}\boldsymbol{v} = {}^{A}\boldsymbol{v}. $$

The gradient coils spatially manipulate the frequency of the MR signal in three mutually orthogonal directions. These coils define the basis set of the gradient coordinate frame (G) that is fixed with regards to orientation and position with an origin that is commonly referred to as the ISO-centre. The aim of prospective motion correction is to move/update the field of view (FOV) so that its moves with the subject so that they appear as if they were stationary throughout the image acquisition. The orientation of the FOV is controlled by performing a rotation of the gradient waveform shapes. The position of the FOV is then selected by introducing linear phase rolls into the discrete sampling of the MR signal, and a frequency change in the RF pulse for changes in the slice direction in 2D pulse sequences. In MRI it is therefore logical to express a change in the (FOV) as a rotation about the iso-centre into a frame that we call the imaging frame (I), which defines the phase, read and slice directions, followed by a translation. An implication of this is that if a pure rotation of the FOV is required that is not centred on the iso-centre, a change in the sampling of the MR signal and RF

Fig. 1.2 Coordinate frames and measuring a change in subject pose. The change in the local frame from the start of the scan $\mathbf{ij}$ to some arbitrary time point later $\mathbf{i}'\mathbf{j}'$ indicates the FOV needs to undergo a rotation α and translation δ.

pulse [2D] (position) will be necessary (this is often the case because subjects typically rotate their heads about the base of their skull). Figure 1.2 introduces these frames and an additional frame called the local frame L. The local frame is the coordinate frame of a marker/device that is rigidly attached to the subject. The local frame is therefore the coordinate frame in which the devices developed in this work measure their respective signals. For now it is assumed that the device can measure the position and orientation of the local coordinate frame with respect to the gradient coordinate frame (G). When the subject moves the local frame transforms from L ($\mathbf{ij}$) to L' ($\mathbf{i'j'}$). The change in orientation (α) of the local and the imaging frames should be identical to achieve the correct FOV orientation:

$$
{}^{L'}_{L}\mathbf{R} = {}^{L'}_{G}\mathbf{R}{}^{G}_{L}\mathbf{R} = {}^{I'}_{I}\mathbf{R} \tag{1.1}
$$

The conjugate of the orientation at the start of the scan ${}^{G}_{L}\mathbf{R}(t_0)$ is saved as a reference and is left hand multiplied by the current orientation of the device ${}^{L'}_{G}\mathbf{R}(t_i)$ at each update step to find the change in orientation ${}^{I'}_{I}\mathbf{R}$. This is then applied to the initial orientation of the field of view ${}^{I}_{G}\mathbf{R}$ selected by the radiographer at the start of the scan. Calculating the change in translation is slightly more complicated because of the challenges associated with centres of rotation. At the start of the scan the device measures a reference position which can be represented by the sum of the location of the centre of the field of view $\boldsymbol{c}$ plus the location of the device $\boldsymbol{d}$ in the FOV frame:

$$
{}^{G}\boldsymbol{p}(t_0) = {}^{G}\boldsymbol{c} + {}^{G}\boldsymbol{d},
$$

which is transformed into the initial imaging frame:

$$
{}^{I}_{G}\mathbf{R}{}^{G}\boldsymbol{p}(t_0) = {}^{I}\boldsymbol{c} + {}^{I}\boldsymbol{d}. \tag{1.2}
$$

The device continues to measures its location thereafter:

$$
{}^{G}\boldsymbol{p}(t_i) = {}^{G}\boldsymbol{\delta} + {}^{G}\boldsymbol{c'} + {}^{G}\boldsymbol{d'},
$$

which is rotated into the current imaging frame for each update:

$$
{}^{I'}_{I}\mathbf{R}{}^{I}_{G}\mathbf{R}{}^{G}\boldsymbol{p}(t_i) = {}^{I'}\boldsymbol{\delta} + \left({}^{I'}\boldsymbol{c'} + {}^{I'}\boldsymbol{d'}\right). \tag{1.3}
$$

The rigid body constraint means that:

$$ {}^{I}\boldsymbol{c} + {}^{I}\boldsymbol{d} = {}^{I'}\boldsymbol{c'} + {}^{I'}\boldsymbol{d'} \tag{1.4} $$

One can then solve for the change in the position of the FOV $\left({}^{I'}\boldsymbol{\delta}\right)$ in Eq. 1.3 using Eqns 1.2 and 1.4:

$$ {}^{I'}\boldsymbol{\delta} = {}^{I'}_{I}\mathbf{R}^{I}_{G}\mathbf{R}^{G}\boldsymbol{p}(t_i) - {}^{I}_{G}\mathbf{R}^{G}\boldsymbol{p}(t_0), \tag{1.5} $$

To update the FOV location one simply adds ${}^{I'}\boldsymbol{\delta}$ to the initial FOV location ${}^{I'}\boldsymbol{c}$. The implications of Eq. 1.5 are that errors in the change in orientation of the local frame would be visible in the position estimates and the absolute position in the gradient coordinate frame is required to determine the change in position of the FOV. If there is variance in the orientation it will be amplified by the distance between the device and the iso-centre, causing a stronger variance of the change in position applied to the FOV. Stable orientation estimates are therefore very important for the successful implementation of prospective motion correction when measuring changes in subject position at a location that is not at (far from) the iso-centre.

Chapter 2

A Method for Measuring Orientation using Gravity and the Static Magnetic Field.

Abstract

In MRI brain imaging, subject motion limits obtainable image clarity. Due to the hardware layout of an MRI scanner, gradient activations can be used to rapidly detect position. Orientation, however, is more difficult to detect and is commonly calculated by comparing the position measurements of multiple spatially constrained points to a reference dataset. The result is increased size of the apparatus the subject must wear, which can influence the imaging workflow. In optical based methods marker attachment sites are limited due to the line of sight requirement between the camera and marker, and an external reference frame is introduced. To address these challenges a method called VectOrient is proposed for orientation measurement that is based on vector observations of gravity and the MRI scanner's static magnetic field. A prototype device comprising of an accelerometer, magnetometer and angular rate sensor shows good MRI compatibility. Phantom scans of a pineapple with zero scanner specific calibration achieve comparable results to a rigid body registration algorithm with deviations less than 0.8 degrees over 28 degree changes in orientation. Dynamic performance shows potential for prospective motion correction as rapid changes in orientation (peak 20 degrees per second) can be corrected. The pulse sequence implemented achieves orientation updates with a latency estimated to be less than 12.7 ms, of which only a small fraction ($<$1 ms) is used for computing orientation from the raw

sensor signals. The device is capable of quantifying subject respiration and heart rates. The proposed approach for orientation estimation could help address some limitations of existing methods such as orientation measurement range, temporal resolution, ease of use and marker placement.

2.1 Introduction

Magnetic resonance imaging (MRI) is vulnerable to subject motion due to the time required to acquire the data needed for image reconstruction. The signal is spatially encoded by manipulating the magnitude of the magnetic field in three orthogonal directions at different times during the signal acquisition. Typically, the acquisition needs to be repeated for many different magnetic field gradients as the physical space within the scanner is encoded in the spatial frequency domain (k-space). Any motion that occurs during image acquisition results in the signal being mapped to incorrect locations causing ghosting and blurring and manifest as artefacts in the resulting images. To further complicate the problem, the magnetic susceptibility of the imaged region usually varies over 'material' boundaries such as tissue-air (sinuses), and tissue-cerebral spinal fluid (ventricles). As a result motion affects the homogeneity of the main magnetic field, because shimming to correct for these susceptibility changes is pose specific.

Advances in acquisition technologies now allow for sub-millimetre spatial encoding of the physical space within the MRI scanner in only a few minutes. Due to an increase in required imaging resolution minute motion and physiological movements (such as the cardiac and respiration cycles) play a limiting role in obtainable image clarity even for healthy subjects who move very little [18]. Subject motion has therefore become a critical aspect in high resolution imaging and remains one of the biggest challenges in difficult to scan populations such as the old and very young where sedation is generally impractical, expensive and in the case of research not admissible due to ethical reasons.

Physically, the spatial encoding of the magnetic field within the MRI scanner is fixed with respect to translation, having a point of zero effect known as the gradient isocentre. Any combination of the x, y and z gradients is therefore physically constrained to a rotation about this single point. Translations in image space are implemented by imposing phase rolls across the corresponding direction in the k-space representation of the measured signal. Therefore identical gradient waveforms (except gradients which select a region in space if slice-selective, but do not play a role in spatial encoding) will be used to image identical field of views (FOVs) at two different locations (same orientation) in the MRI scanner. If an object changes orientation within an MRI scanner and one applies an incorrectly oriented version of the pulse sequence, magnetisation will be different and contrast will be affected as the relative magnitude of the magnetic field at each point on the object has changed. Translation is a macro effect that introduces a bias in the frequency and phase of the net signal received from the imaged object proportional to the applied gradient vector. Each time a gradient waveform is played out a constant frequency offset needs to be interpreted correctly to ensure correct image encoding. Any error in translation between the measurement frame and the pulse sequence frame will manifest in a phase roll as each point is sampled in the incorrect reference frame. Incorrect interpretation of how the signal is received is independent of the gradient waveform shapes and will therefore have no effect on the magnitude of the MR signal (in an idealised MRI scanner).

Retrospective motion correction techniques rely on correcting/adjusting image/k-space after the data has been collected. Besides effects caused by discretely sampling the signal such as aliasing, the effects of translation can be corrected retrospectively if it is known (and the correct spins were excited). Retrospective correction of orientation, even if the motion was tracked perfectly, would still have errors due to spin history effects and an inconsistently sampled k-space grid [19]. Rapid correction of orientation is therefore paramount to ensuring stability of the magnitude of the raw MR signal as the physical formation of the image is directly related to orientation; rotating k-space rotates the image by the same angle. This has led to the development of prospective motion correction in which motion parameters are tracked and corrections are applied to the pulse sequence as frequently as possible during the image acquisition. Prospective motion correction is realised by altering the way in which the linear combination of the x,y and z gradients contribute to the predefined waveforms (orientation) of the pulse sequence and the relative frequency at which the raw MR signal is demodulated (translation) to effectively follow a rigid object as it moves within the MRI scanner. In the case of neuro-imaging the brain is modelled as rigid, even though small amplitude (50μm) plastic deformation is present [20].

2.1.1 Measuring Orientation using Gradient Encoding.

In most cases orientation is measured using the gradient coil system of the MRI scanner. These techniques inherit the co-ordinate frame of the imaging sequence allowing them to be calibration free. Intuitively one can use the same principles used for image acquisition to track orientation in the image domain. Low resolution 3D image acquisitions [7] (vNav) or a series of 3 orthogonal 2D spiral acquisitions [5] (PROMO) are inserted into the existing pulse sequence. These approaches then co-register subsequent lower resolution images to an initial reference image to measure the change in subject pose. The information rich dataset can also be used to correct for changes in the homogeneity of the scanner's magnetic field. These methods do, however, have limited temporal resolution and can fail during rapid motion or completely miss small periodic motion. Fast k-space navigators [21] overcome some of the temporal resolution limitations of these techniques, at the cost , however, of increased sequence dependence or the need for reference datasets that can affect the accuracy of motion measurements. Free induction decay navigators [22] form a useful tool for detecting motion and have recently been shown to produce sufficient accuracy for prospective motion correction [42]. These methods are, however, dependent on an accurate map of the receive coil sensitivity profiles and training datasets making tracking performance difficult to predict between subjects and motion profiles.

External hardware can be introduced to improve the robustness of orientation estimates of k-space navigator approaches, such as active markers [11] or inductive coils [17]. These approaches overcome some of the challenges of measuring orientation in the frequency domain (k-space) by physically encoding orientation using translation measurements of multiple points. A linear combination of gradients can only encode position in one direction at any instant in time. Three different (preferably orthogonal) gradient pulses can be inserted into the pulse sequence to measure the position of one or multiple points in the gradient co-ordinate frame. To fully constrain the orientation a minimum of 3 points (active markers) or 2 points and the direction of the gradient flux vector (inductive coils) are required to uniquely define the orientation of the tracked object. The requirement for 3 unique gradient activations that would not normally be present in the imaging pulse sequence means that motion measurement is restricted as new activations could affect the quality of the resulting image. This is especially true in Echo Planar Imaging (EPI) sequences where long uninterrupted echo trains are required. Gradient tones [23] allow a reduction in pulse sequence impact, however this comes at the cost of reduced achievable slew rate and still requires multiple markers.

2.1.2 Sequence Independent Approaches.

Sequence independent methods measure motion parameters using external hardware, such as optical motion tracking [13]. Independence of the pulse sequence allows for versatile and rapid acquisition of motion parameters. The use of a camera to track an in-bore marker which has a limited measurement range does however introduce new challenges such as camera mounting, MR compatibility, marker line-of-sight, lighting and the introduction of a new reference frame that has to be calibrated to a fixed camera position making it time consuming to set up [24].

2.1.3 Challenges in Orientation Measurement.

The pulse sequence modifications required for gradient based methods and increased complexity of current sequence independent techniques have resulted in prospective motion correction using external hardware having a limited impact in clinical MRI even though it has been proven to be effective. In most current external motion tracking techniques orientation is not measured directly. Rapid translation measurements of multiple points are used to encode orientation ([11],[13],[17],[25]). The distance between each of the points must be kept constant throughout the image acquisition for comparison to the initial positions to remain valid. To achieve the same precision for orientation as translation measurements these points should enclose the entire imaging volume, making the apparatus the subject has to wear large. To address this challenge specialised retrogate markers have been implemented which spatially encode orientation on the marker itself using *Moire patterns* ([26]). In this method there is still however a tradeoff between size and precision and restriction of line of sight makes the marker more vulnerable to motion relative to the subject.

2.1.4 VectOrient - An alternative approach.

An orientation measurement technique requiring just a single marker would complement existing methods, and could, if combined with a single translation measurement, allow for rigid body motion correction from a single point. Knowledge of orientation greatly reduces the challenges associated with k-space navigator design and could benefit self-navigated pulse sequences or complement retrospective techniques. We demonstrate here a vector based approach to orientation measurement that does not require spatially encoding orientation. The device relies on measuring the direction of the static magnetic field and gravity. The magnetic field vector and gravity are both observable from any point within the scanner bore which allows one to mount the marker anywhere on the ‘rigid’ body of interest, in any orientation, because there are no restrictions on measurement range or line-of-sight. The vectors are also both well defined relative to the scanner gradient co-ordinate system. The proposed orientation tracking method is therefore calibration free, to the extent that the scanner's construction is accurate, whilst remaining sequence independent.

2.2 Theory

The MRI environment is unique in that there exists a static magnetic field that is exceptionally stable over time. A small Hall effect magnetometer can be used to measure this vector very precisely due to the large magnitude of the physical field. A single vector observation, in this case the scanner's static magnetic field, constrains the sensor's orientation relative to any frame in which that vector is known to a single degree of freedom about the axis of the observed vector. To fully define the sensor's orientation relative to the reference frame another measurement that is not parallel/anti-parallel to the existing observation is required. During an MRI scan, the patient spends the majority of the time at rest. During these periods the accelerometer gives an estimate of the direction of gravity in the sensor frame. It is important to note that the accelerometer measures the resultant of the forces acting on a proof mass and not the total acceleration:

$$\vec{a} = \frac{\vec{F}_{body} - m_{proof}\vec{g}}{m_{proof}}$$

Therefore, during periods when the patient is still ($F_{body} = 0$), the accelerometer measures:

$$\vec{a} = -\vec{g}$$

Even though the sensor itself is in equilibrium and not accelerating. This fully constrains the sensor's orientation in a reference frame where both the directions of $\vec{B_0}$ and $\vec{g}$ are known, in fact the problem is now over constrained.

Fig. 2.1 describes a conventional MRI scanner layout in which gravity ($\vec{g}$), which lies normal to the patient bed, and the static magnetic field ($\vec{B_0}$), which runs axially along the scanner bore, are almost perfectly orthogonal to each other. As part of the main magnet installation as specified by the 3 T Skyra (Siemens, Erlangen, Germany) used in this work, pendulums are used for aligning the scanner YZ plane to gravity.
This justifies two assumptions made for the scanner reference frame:

- Gravity lies on the YZ plane of the gradient fields.

- The static magnetic field and the gradient Z-axis are parallel, misalignment would cause gradient torques increasing the scanner noise.

2.2.1 From Vector Observations to Orientation

Based on the assumptions made one can define the following reference matrix $\mathbf{H}$ without any calibration between the sensor and scanner frames:

$$\bar{\mathbf{h}}_{\mathbf{1}} = \frac{\vec{B}_0 \times \vec{g}}{\|\vec{B}_0 \times \vec{g}\|}$$

$$\bar{\mathbf{h}}_{\mathbf{2}} = \frac{\vec{B}_0 \times \bar{\mathbf{h}}_{\mathbf{1}}}{\|\vec{B}_0 \times \bar{\mathbf{h}}_{\mathbf{1}}\|}$$

$$\bar{\mathbf{h}}_{\mathbf{3}} = \frac{\vec{B}_0}{\|\vec{B}_0\|}$$

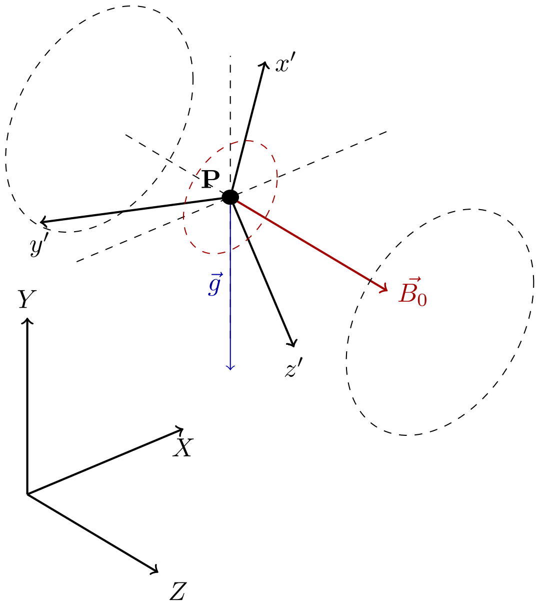

Fig. 2.1 Sensor frame ($x'y'z'$) relative to the scanner co-ordinate frame (XYZ), the large dotted circles represent the MRI scanner bore. The ground lies parallel to the XZ plane.

$$\mathbf{H} = \begin{pmatrix} \bar{\mathbf{h}}_\mathbf{1} \\ \bar{\mathbf{h}}_\mathbf{2} \\ \bar{\mathbf{h}}_\mathbf{3} \end{pmatrix} = \begin{pmatrix} 1 & 0 & 0 \\ 0 & 1 & 0 \\ 0 & 0 & 1 \end{pmatrix}$$

One can then form a matrix M from the data obtained from the accelerometer $\vec{a}$ and magnetometer $\vec{m}$ which are observations of $\vec{B_0}$ and $\vec{g}$ in the sensor frame:

$$\bar{\mathbf{m}}_\mathbf{1} = \frac{\vec{m} \times -\vec{a}}{\|\vec{m} \times -\vec{a}\|}$$

$$\bar{\mathbf{m}}_\mathbf{2} = \frac{\vec{m} \times \bar{\mathbf{m}}_\mathbf{1}}{\|\vec{m} \times \bar{\mathbf{m}}_\mathbf{1}\|}$$

$$\bar{\mathbf{m}}_\mathbf{3} = \frac{\vec{m}}{\|\vec{m}\|}$$

$$\mathbf{M} = \begin{pmatrix} \bar{\mathbf{m}}_\mathbf{1} \\ \bar{\mathbf{m}}_\mathbf{2} \\ \bar{\mathbf{m}}_\mathbf{3} \end{pmatrix}$$

It follows that in this special case the rotation matrix representing the rotation from the scanner frame to the sensor frame is identical to the matrix formed by the observed normalised vectors:

$$\mathbf{M} = \mathbf{RH} = \mathbf{RI} = \mathbf{R} \tag{2.1}$$

The result shows that vector observations can be used to form an orthonormal rotation matrix representing the orientation of the device in the scanner frame with very few computations. It also intuitively shows the importance of the orthogonality of the vectors. As the vectors lie more parallel to each other, the effect of noise on the unit vectors increases. During periods of motion, measurements of the direction of gravity using the accelerometer become unreliable due to accelerations of the sensor frame. These external accelerations are dealt with through a combined approach of constraining and filtering. The acceleration estimates are constrained as described above; notice that $\bar{\mathbf{m}}_\mathbf{2}$ is formed using the vector cross product rather than just selecting gravity as the negative Y-axis. The accelerometer measurement now only affects the orientation about the axis of the static magnetic field. The acceleration measurements are then used to track biases in an angular rate sensor with a slow temporal response of 10-20 seconds removing the effect of small local accelerations. This is achieved by implementing a complementary filter that combines angular rate, magnetometer and acceleration measurements.

2.2.2 Sensor fusion

A *Mahony* [27] non-linear complementary filter (Fig. 2.2) was selected to fuse the sensor measurements. The observer proposed assumes an angular rate sensor model as follows:

$$\mathbf{\Omega}_a(t) = \mathbf{\Omega}_r(t) + \mu_\omega(t) + \omega_0 \tag{2.2}$$

Where $\mathbf{\Omega}_a(t)$ is the measured angular rate and $\mathbf{\Omega}_r(t)$ is the real/corrected angular rate, which is integrated to give the orientation estimate. The integral feedback of the filter is expected to track the slow drift in gyro bias ($\omega_0' \approx \omega_0$) and the proportional feedback compensates for noise and gyro imperfections ($\mu_\omega'(t) \approx \mu_\omega(t)$). Quaternion

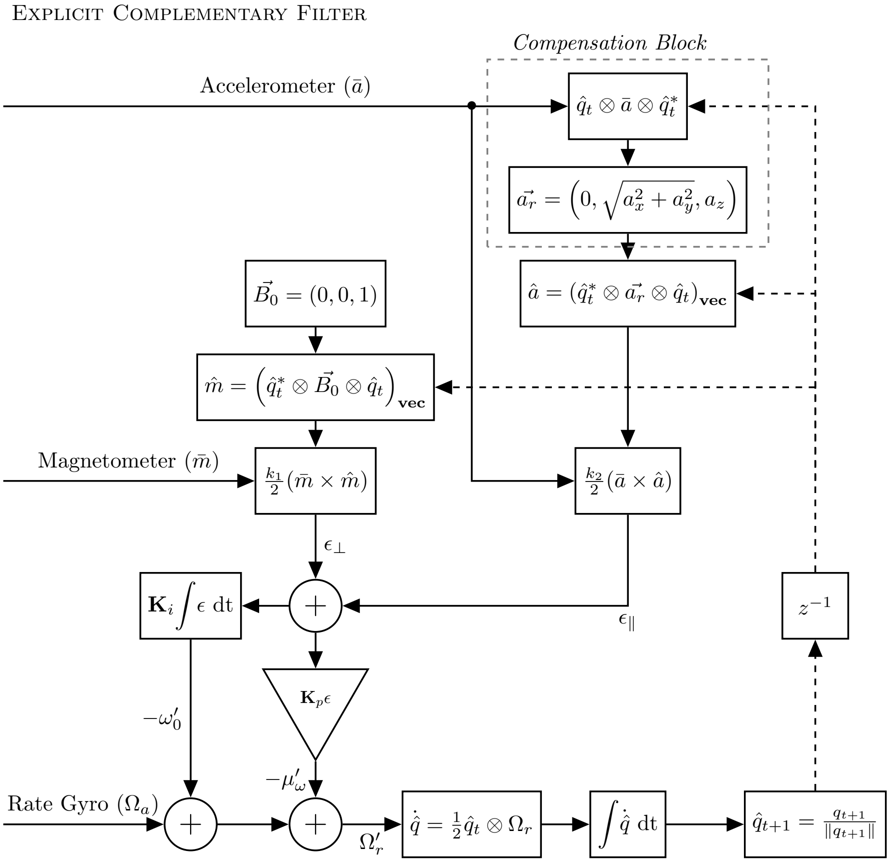

Fig. 2.2 Explicit (vector based) complementary filter with angular rate gyro bias compensation. $\hat{q}$ symbol designates a unit quaternion and $\otimes$ represents quaternion multiplication. All vectors are unit in magnitude and the $\times$ symbol represents the vector cross product. The output of the filter $\hat{q}_{t+1}$ represents the scanner co-ordinate system (scs) with respect to the device co-ordinate system (dcs). Primes denote estimates of the gyro bias (ω_0') and imperfections (μ_ω').

representation of orientation was selected to allow for a more efficient execution of the algorithm on an embedded device.

2.2.3 Constraining the gravity error term

Madgwick [28] initially proposed a compensation technique to reduce the observer's sensitivity to magnetic field inhomogeneities in the application of motion tracking in rehabilitation. Apparent fluctuations in the earth's magnetic field, caused by nearby ferrous materials, cause drifts in the magnetic field vector which could affect the attitude of the output estimate. The error term generated by the magnetometer was therefore constrained to only affect the heading estimate. In the modified version proposed (Fig. 2.2, *Compensation block*), acceleration parallel to the observed $\vec{B_0}$ field and any slight non-orthogonality between gravity and the static magnetic field are accounted for, this allows for the assumption of gravity lying on the $\mathbf{YZ}$ plane instead of a more restricted constraint of gravity having to be parallel to the gradient $\mathbf{Y}$-axis (see Fig. 2.1). The formation of the reference acceleration vector ($\vec{a_r}$) has the same effect as the cross product ($\bar{\mathbf{m_2}}$) in the formation of $\mathbf{R}$ in Eqn 2.1. By enforcing the unit constraint on the result one can efficiently calculate the compensated acceleration reference $\vec{a_r}$ because only the z-component of the rotated vector is required ($\sqrt{x^2+y^2} = \sqrt{1^2 - z^2}$).
Using quaternion algebra:

$$\begin{aligned} a_r^z &= \bar{a}^x(2q^xq^z - 2q^wq^y) \\ &\quad + \bar{a}^y(2q^yq^z + 2q^wq^x) \\ &\quad + \bar{a}^z(1 - 2q^xq^x - 2q^yq^y) \end{aligned} \tag{2.3}$$

Where:
$q^{w,x,y,z}$ are the elements (w scalar and x, y, z vector) of the unit quaternion representing the current estimate of the orientation.
$\bar{a}^{x,y,z}$ is the acceleration measured in the sensor frame.
a_r^z is the z component of the new reference vector that ensures the error term is parallel to the $\vec{B_0}$ field.

2.2.4 Filter gain selection

The implementation of the proposed observer is unique in MRI in that there exists an exceptionally stable observation of the magnetic field. Referring to Fig. 2.2 we select

$k_1 >> k_2$. The purpose of the gyro is mainly to improve the orientation estimates about the MRI scanner's Z-axis, during periods of motion when $\bar{a} \neq \bar{g}$. The purpose of tracking the gyro imperfections using the magnetometer is that as the orientation of the sensor frame rotates the Z-axis errors project onto the axes on the orthogonal plane. This effect was reported by [27] where a single vector observation of gravity was used to track gyro bias about the heading axis. In the present work the magnetometer complements the acceleration measurements to achieve better performance about the $\vec{B_0}$ field (Z-axis). The gains k_{1-2} are selected to be high enough such that the vector observations are weighted as highly as possible without increasing the uncertainty in the output over each time step. As a starting point the gain is selected to ensure convergence of the output and the field vector estimate at a maximum rate:

$$k_{1-2} < \frac{\tau_\omega^2}{\sigma_\theta^2} \times \mathrm{t_s} \qquad (2.4)$$

Where:
$\sigma_\theta^2(\mathrm{rad}^2)$ is the variance in the direction of the unit vector observations. $\tau_\omega(\frac{\mathrm{rad}}{\sqrt{\mathrm{s}}})$ is the gradient of the Allan deviation curve corresponding to the angular random walk (ARW) of the angular rate gyro.
$\mathrm{t_s}$ is the filter iteration period.
The noise on the magnetometer σ_θ^2 is estimated as being zero mean and axis symmetric [29] and is calculated over a finite period. A similar process is followed for the selection of the accelerometer feedback gain. The data used for the variance calculation is taken from within an MRI scanner while it is active and the sensor is left motionless. It therefore includes the vibrations caused by eddy current interactions which are not considered subject motion.
The integral and proportional gains (K_i, K_p) are chosen to add up to 1 where the ratio controls the response of the filter. To prevent integral windup the rate gyro biases and initial orientation are estimated at the system start. This requires the device to be held still from 2 until 4 seconds after power up. The initial orientation is estimated from Eqn. 2.1 and the biases are computed as a running average over the initialisation period. This step can be skipped and the filter will converge, albeit much slower about the axis of the static magnetic field (20 s with typical gain settings [$k_2 = 1.5$]).

2.2.5 Sensor Models

In reality the vector observations obtained from the sensors are not ideal, distorting the measurements from a spherical surface onto an ellipsoid, Fig. 2.3. A two step calibration of the sensors was implemented based on the following sensor models. For the accelerometer:

$$\mathbf{a}_a = \mathrm{T}_a^{3\times 3}(\bar{\mathbf{a}}\|(\vec{g} + a\vec{(t)})\| + \vec{\mu}_a) + \mathbf{a}_0 \tag{2.5}$$

The affine transform $\mathbf{T}_a^{3\times 3}$ and offset $\mathbf{a}_0$ represent the accelerometer imperfections and are modeled as being time invariant. These include x,y and z axis misalignment within the sensor structure, gain variations of the sensor elements and other linear effects. Un-modeled accelerations $a\vec{(t)}$ are expected to be of a higher frequency than the random walk caused by integrating noise in the angular rate gyro and would therefore be eliminated by the low pass effect of the complementary filter.
The magnetometer is modeled as follows:

$$\mathbf{m}_a = \mathrm{T}_m^{3\times 3}\bar{\mathbf{m}}(B_s) + \vec{\mu}_m + \mathbf{m}_0 \tag{2.6}$$

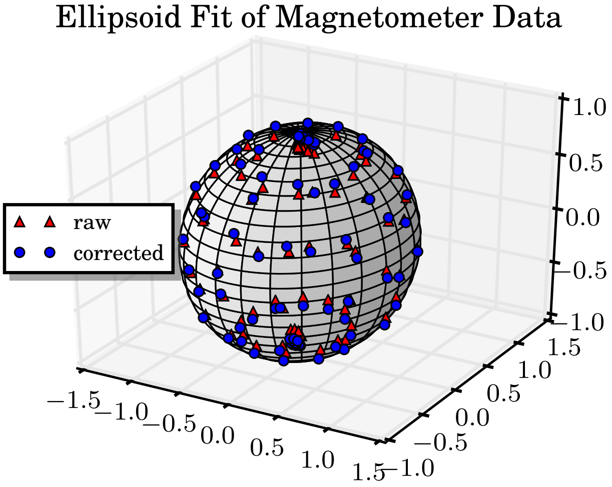

Fig. 2.3 Circles are the calibrated data fit to a unit sphere. Notice the scaling of the uncalibrated (raw) triangles in the vertical axis. This could be expected as the z-axis sensing element is structurally different to the ones lying on the plane of the integrated circuit.

Where,

$$B_s = \|\vec{B_0} + \vec{G_{prs}}(t)s(x,y,z) + \vec{B_1}(t)\|$$

The direction of the superposition of magnetic fields lies very close to the gradient z-axis. This is because the static magnetic field is many orders of magnitude stronger than the time varying gradients. The radio frequency pulses, which are orthogonal to the z-axis, are negligible because of their small magnitude and high frequency. The magnetometer is slightly more vulnerable to distortion due to hard and soft iron effects. The matrix $\mathbf{T}_m^{3\times3}$ models these effects along with other linear effects similar to the correction matrix used for the accelerometer. A once-off calibration sequence is therefore implemented similar to [30]. The individual sensor offsets and transformations are calculated by fitting a set of data points (preferably evenly distributed) to an ellipsoid using a constrained least squares algorithm Fig. 2.3. The calibration matrix then maps the fitted ellipsoid onto a unit sphere. The calibrated and scaled unit vectors form the accelerometer $\bar{\mathbf{a}}$ and magnetometer $\bar{\mathbf{m}}$ inputs to the observer (Fig. 2.2).

2.3 Materials and Methods

The following section describes the development of the orientation tracking hardware prototype (Figure 2.4). The computationally light-weight explicit complementary

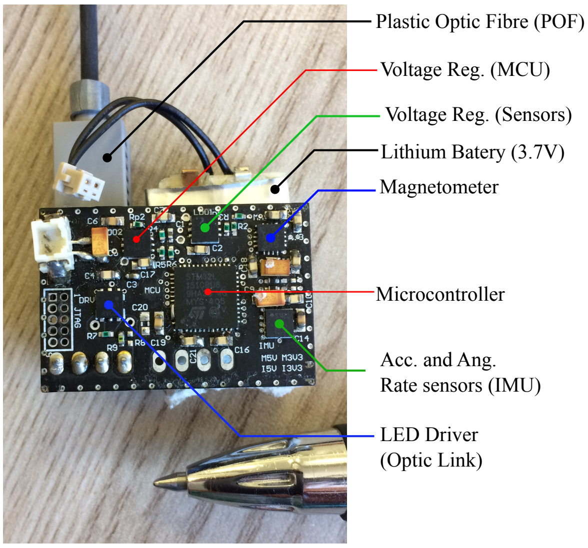

Fig. 2.4 Prototype hardware. The larger IC in the centre is the Micro-controller. Underneath left is the optical transmitter. Right of the MCU are the sensors.

filter was implemented on a low power embedded device. A consumer grade inertial measurement unit (which contains the 3-axis accelerometer and angular rate gyro sensors) was used in the prototype design allowing for a low cost implementation. The magnetometer was however a more specialised part as the magnetic field strengths are far greater in the MRI scanner. Commercial parts are optimised for earth's field navigation. The use of the vector (cross-product) to generate the error function was much more computationally efficient because no formation of an unfiltered orientation quaternion was required. The MRI scanner passed both the RF noise and spike quality assurance tests supplied with the MRI scanner (3T, Skyra, Siemens, Erlangen, Germany) while the device was streaming orientation data from within the receive coil. The device artefacts penetrate approximately 10-15 mm into the image in the gradient

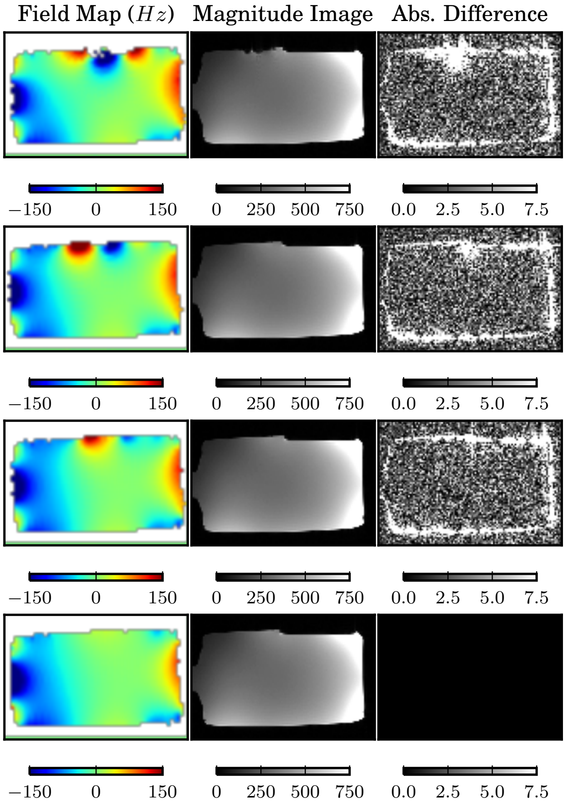

Fig. 2.5 From top to bottom rows the device was placed directly against the cylindrical phantom; 10 mm normal to the top surface; 20 mm normal to the top surface; and finally imaged without the device present. The gradient echo images (TR 10 ms, TE 5 ms, voxel size [P 0.7 mm, R 0.7 mm, S 1 mm]) were obtained in a different series of scans with the same sensor offsets relative to the phantom surface. All difference images are computed relative to the magnitude image acquired without a device.

echo pulse sequence implemented as can be seen in Figure 2.5 and therefore only has a significant effect on the signal strength in the skull/fat signal when mounted as shown in Figure 2.6.

2.3.1 Printed Circuit Board (PCB) design considerations

A four layer stack was used in the PCB layout. Signal traces on the top layer were routed to the inner layers as close to the integrated circuit footprints as possible. The remaining area was filled with a solid copper pour to shield the signals from the high power magnetic fields within the MRI scanner. The bottom layer was selected to be a solid pour with vias connecting the top and bottom layers around the periphery of the PCB in an attempt to make a Faraday cage around the signal traces. There was a trade off between the amount of copper used, which would interact with the gradient fields causing eddy currents which would vibrate the circuit as can be seen in Fig. 2.7, and the amount of radio frequency (RF) shielding. The 32-bit micro-controller is clocked at 32 MHz from an internal RC (resistor-capacitor) oscillator eliminating the need for an external quartz crystal. Quartz crystals are generally packaged in ferro-magnetic materials which can result in large image artefacts. This did however affect the maximum baud rate achievable over the serial link due to uncertainties in the oscillation frequency. A hot air solder levelling (HASL) finish was used for the footprints which is free from nickel (a major source of field interaction). Non-magnetic capacitors (in small values) and resistors were used where possible. Power supply filtering was achieved using 10 μF tantalum capacitors in a plastic casing. Integrated circuits in certain quad flat no-leads (QFN) packages were free of nickel and could be used for the device's construction. A single cell, aluminium foil, lithium polymer battery pack with copper terminals was used to power the device (150 mAh) allowing 4 hours of continuous operation.

2.3.2 Plastic Optic Fibre Communication

The prototype uses a plastic fibre optic cable for uni-directional asynchronous serial communication with a laptop situated in the scanner control room (460800 bps). For improved performance data were transmitted in binary format of a fixed length. Each transmission contained 4 32-bit floating point values ($\hat{q}$), 9 16-bit integers ($\bar{a}, \bar{m}, \bar{\omega}$) followed by a line-feed (0x0A) and carriage return (0x0D) for a total of 36 bytes. Data packets were transmitted at 300 packets/s to the laptop. A python thread would then poll the operating systems serial buffer ensuring no more than one packet was buffered at a time to improve latency. A real-time (60 fps) 3D representation of the orientation of the device is displayed on the laptop with data logging capabilities. The laptop is connected to the local scanner switch (1 Gigabit TCP/IP) allowing the scanner control computer to query the laptop for the latest orientation estimate. The latency for the laptop response to a scanner query was found to be less than 1 ms based on the scanner's μs clock (although this is dependent on the laptop's state).

2.4 Results

The prototype device was tested to ensure safe and correct operation under scanning conditions. The alignment of the sensor and scanner co-ordinate frames was evaluated using high resolution 3D registrations. The potential for prospective motion correction (if combined with a translation measurement technique) was evaluated using controlled changes in orientation without translations. Finally, the application of the device to physiological motion measurement is presented.

2.4.1 MRI compatibility

To simulate a realistic positioning relative to the gradient iso-centre the device was mounted on a healthy subject's forehead (Fig. 2.6). All scans involving volunteers were

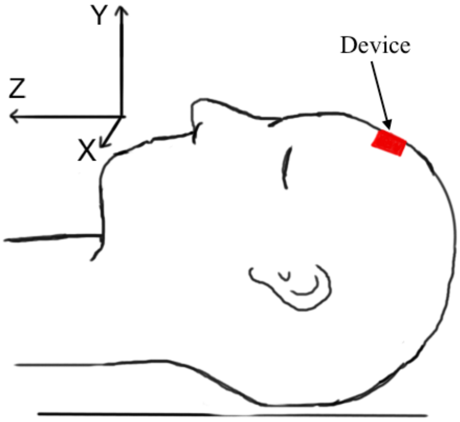

Fig. 2.6 The sensor was mounted on the patient's forehead using double sided tape for the human physiological data acquired. Due to the small size of the device and small magnitude of the gradient torques, no abnormal heating (typically $\approx 0.2°\mathrm{C}$) could be detected using the embedded (Magnetometer and IMU) temperature sensors. In some cases the ground plane temperature decreased during scanner operation.

conducted in accordance with protocols approved by the Faculty of Health Sciences Human Research Ethics Committee of the University of Cape Town. The data were collected in real time (300 Hz) during a 3D gradient echo pulse sequence. The angular rate gyro showed a slight bias (+- 4 dps) dependent on the sensor's orientation relative to the static magnetic field, however the filter successfully tracks the biases

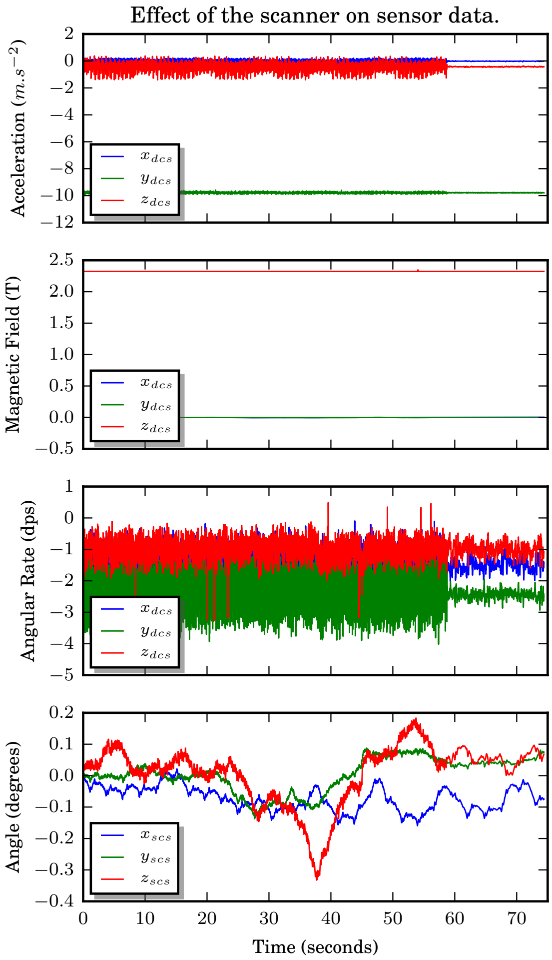

Fig. 2.7 Effect of gradient activity on accelerometer and angular rate measurements. Data were logged during an MR acquisition (first 58 s, gradient echo pulse sequence) and continued after the pulse sequence had ended (roughly last 15 s of the plot). The relatively high temporal resolution signal, present while the scanner is active, is periodic and well correlated with the repetition time (TR; 10 ms) of the imaging pulse sequence. This is most likely caused by eddy current interactions with the static magnetic field causing vibrations of the scanner bed and/or PCB. Secondary effects could include diodes in the measurement circuit rectifying induced currents or field interactions with the micro-electromechanical elements. Data displayed was recorded while attached to a subject, hence the visible involuntary changes in orientation.

with no noticeable effects on the output orientation. Interestingly these spurious biases are largely orthogonal to the static magnetic field and are therefore mitigated by the high precision magnetometer observation. Sufficient resolution of the subject's orientation is achieved to view the cardiac and respiration cycles. Referring to the data shown in the lowest plot of Fig. 2.7 it is evident that the device achieves the best performance about the axes tracked using the magnetometer. The z-axis shows the poorest performance due to the noise induced by field interactions even though the gradient interactions on the accelerometer dominate in the z-direction. This highlights the importance of the compensation block in the filter (Fig. 2.2).

2.4.2 Measurement Accuracy

To test the validity of the reference frame assumptions made, such as gravity and the static magnetic field being predefined in the imaging co-ordinate system due to the scanner's construction, orientation estimates were fed back to a 3D spoiled gradient echo pulse sequence (TR 10 ms, TE 8 ms, voxel size [P 0.7 mm, R 0.7 mm, S 2 mm]) without any scanner specific calibration. The orientation of the imaging pulse sequence was updated using orientation estimates from the sensor hardware. A pineapple phantom mounted on a mechanical 'wobbler' was used as the subject. The centre of rotation of the wobbler was aligned to the gradient iso-centre to minimise the amount of uncorrected translation. The wobbler allows for controlled changes of the pineapple's orientation (+- 15^o) about a single axis at a time. The laptop logged the orientation estimate sent to the scanner control computer for each query. Each data point therefore corresponds to one TR of the imaging pulse sequence (first column of Fig. 2.8.)
For each movement of the pineapple, 3 images were obtained:

1. An image at the initial orientation.
2. An orientation 'corrected' image where the phantom was moved to a new orientation approximately 8 s into the acquisition. This was done early in the acquisition to ensure most of the data were captured in a frame defined by the device, giving a true representation of sensor frame errors.
3. An image at the final orientation.

To estimate the accuracy of the sensor defined co-ordinate frame the resulting 'orientation corrected' images (2) were compared to the result from a widely used 3D registration tool '*mri robust register*' [31]. Firstly, image (3) was registered to image (1). The registered image was then subtracted from image (1) and the absolute value of the difference at each voxel computed. The resulting difference image is plotted in the third column of Fig. 2.8 to illustrate the magnitude of registration errors arising from the rigid body fit. To reduce the impact of uncorrected translations on the difference image between the sensor corrected image (2) and original image (1), a translation only registration was implemented using the same software tool. Finally, the sensor corrected difference image was obtained by subtracting the (translation only) shifted image (2) from the initial image (1) (column 2 of Fig. 2.8). The orientation sensor showed comparable performance to the registration algorithm with peak differences occurring in similar locations. These changes are most likely as a result of inhomogeneities in the static field, and changes in RF receive sensitivity caused by motion. In all cases the registration algorithm converged to well within the recommended limits. The resulting transforms from the registrations were also compared to the change in orientation measured by the orientation sensing hardware (Table 2.1). The magnitude of the angle measured by the hardware was consistently smaller than that of the registration algorithm (within a maximum difference of 0.8 degrees). The difference in axis of rotation is a result of misalignment between the measurement frames. The offset between the rotation axes was however very consistent over different angles for each of the controlled rotations and could be corrected by applying the measured deviations. This correction was not applied to the data presented here, so as to demonstrate the performance without scanner-specific calibration. However, this correction could be used as a method for real-time calibration when used alongside slower navigated methods. It was found that the reference frame errors were mostly in the positive x and negative z axes (both within 2 degrees, in our installation).

Table 2.1 Change in Orientation in the Scanner Frame

Dataset	**Registration (deg.[axis])**	**Sensor (deg.[axis])**
Test 0	13.56(-0.064,0.110,-0.992)	13.31(-0.062,0.089,-0.994)
Test 1	28.59(0.006,-0.193,0.981)	28.23(0.002,-0.169,0.986)
Test 2	28.46(-0.304,0.359,-0.883)	27.62(-0.315,0.322,-0.893)
Test 3	4.08(-0.018,1.000,0.012)	3.85(-0.051,0.998,-0.022)
Test 4	14.96(0.004,-1.000,-0.011)	14.18(0.033,-0.999,0.032)

2.4.3 Evaluation of Dynamic Performance

The ability to correct for varying degrees of motion was evaluated with a series of dynamic scans. The pulse sequence parameters were changed to allow a shorter TR in this case (TR 7.5 ms, TE 3.76 ms, voxel size [P 0.7 mm, R 0.7 mm, S 4 mm]). The latency for each orientation update is determined by the pulse sequence repetition

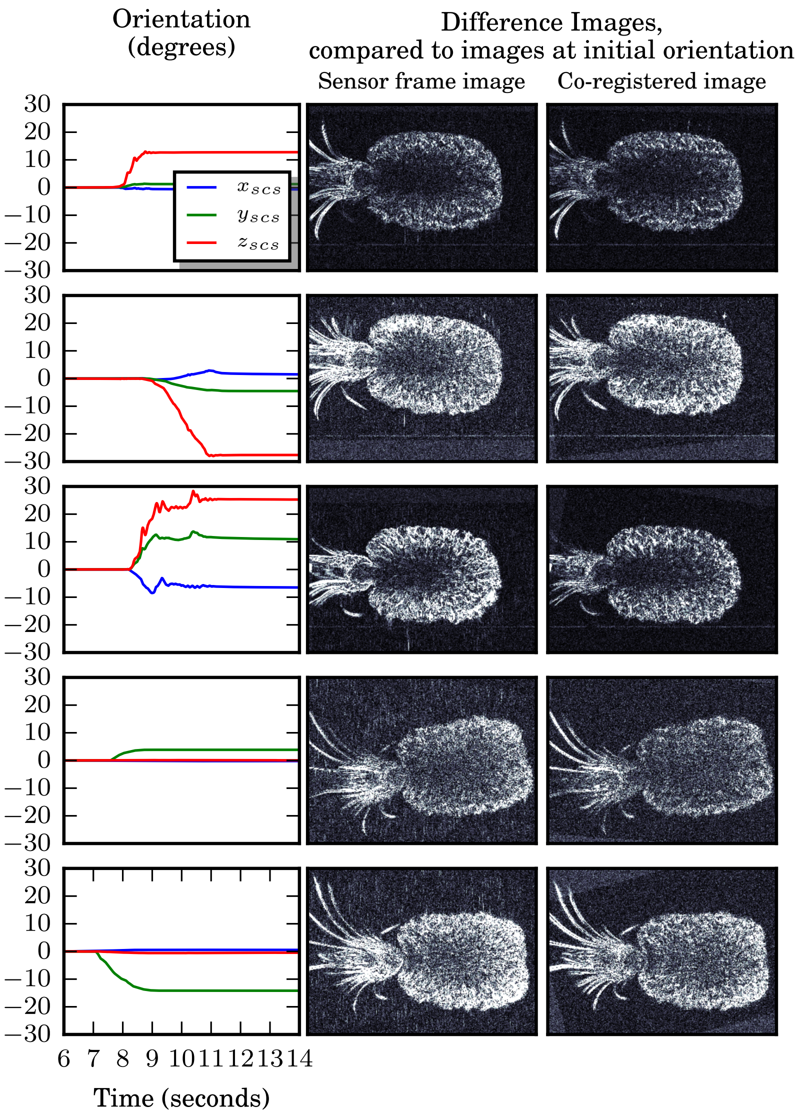

Fig. 2.8 Comparison of the sensor frame to a high resolution registration. All images are scaled 0-25% relative to the first uncorrupted image at the initial positions to more clearly show subtle differences. The first column shows the change in orientation applied to the pineapple for each of the 5 tests. The motion of tests 0-2 were achieved by hand, hence the more shaky changes.

time (TR), the period between data ready pulse on the sensor pin and data transmission of the orientation data ($t_{\text{filt}} \approx 900\,\mu\text{s}$), the laptop response delay ($t_{\text{delay}} < 1\,\text{ms}$) and the frequency of the asynchronously transmitted data (300 Hz), therefore:

$$t_{\text{latency}} < \left(\frac{1}{300} + \text{TR} + t_{\text{filt}} + t_{\text{delay}}\right) = 12.7\,\text{ms}.$$

It is important to note that the dependence on pulse sequence repetition time is only due to practical limitations of updating the gradient co-ordinate frame once per readout and ensuring the gradient control buffer does not underflow. The quoted latency is an estimate of the maximum delay expected. Due to the undetermined nature of TC/IP, in some cases the delay (t_{delay}) would be longer than expected. In order to detect any unexpected delays the pulse sequence would log any instances in

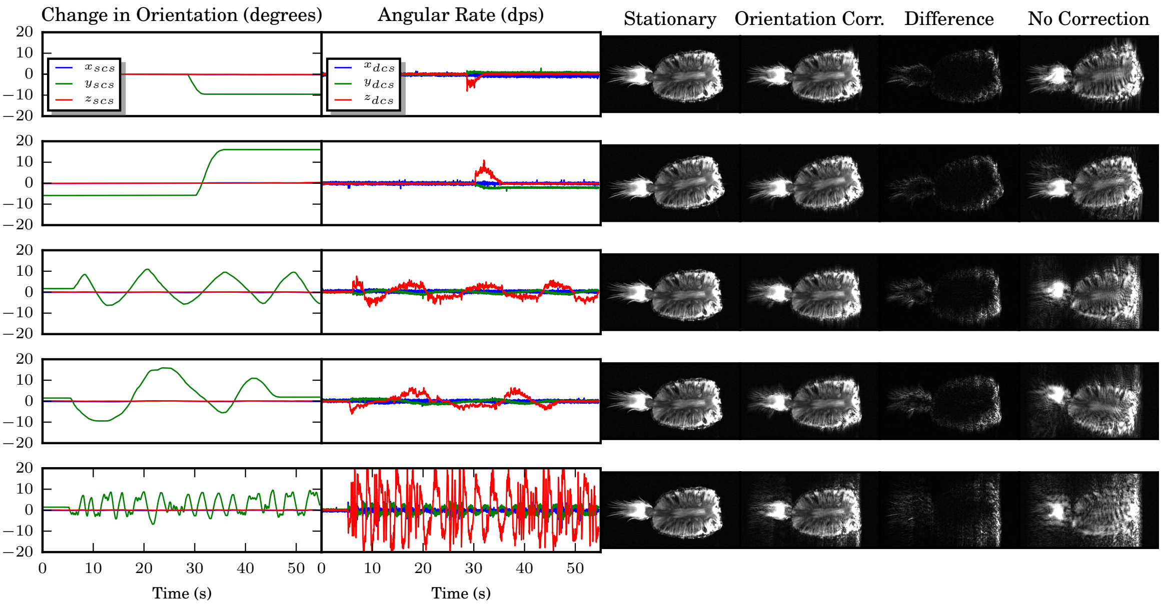

Fig. 2.9 Evaluation of dynamic performance for the potential application of prospective motion correction. The change in orientation is plotted relative to the very first scan in the series presented (top, left). The angular rate gives an indication of the severity of the motion. Difference images present absolute values from a voxel-wise subtraction of the stationary and orientation corrected images. In each case the ‘No correction’ image was collected under replicated motion, similar in amplitude and timing without orientation updates applied. In the final row the prospective orientation correction begins to fail as more blurring artefacts are present. This row does however represent an exceptional case with 26 changes of ≈10° and 40 changes of 3°-5° over a 50 second scan.

which the query for orientation was not serviced in time for the next sequence update, indicating a latency of greater than 2 TRs (15 ms). In the data presented (Figure 2.9) this only occurred a maximum of 2 times out of the $228 \times 32 = 7296$ lines acquired for that image. In each case the total acquisition time was 55 s. The results from least (top) to most (bottom) severe motion are presented in Figure 2.9.

2.4.4 In Vivo Involuntary Changes in Orientation

Raw data in all 3 axes showed a strong correspondence to a 4 channel electro-cardiogram (ECG) signal obtained (Fig. 2.10) while a subject lay motionless within the MRI scanner. High and Bandpass filtering the signal with a zero-phase digital filter allowed for the separation of 'cardiac' and 'respiration' signals respectively. The ballisto-cardiographic nodding motion detected here could be due to skin motion pulsations from small subcutaneous blood vessels or blood pressure fluctuations in the carotid arteries. Aortic valve regurgitation can result in a visible head motion such as *Corrigan* and *de Mussets* signs. The nodding pulsations detected could be due to a similar phenomenon at a much smaller scale in the healthy subjects scanned.

2.5 Discussion

Field interactions with the sensing device are the major contributor to noise in the orientation estimates and image artefacts (in close proximity to the device). The sensor PCB and battery size therefore play a significant role in the performance of the orientation estimates. The initial prototype could be improved by reducing the overall size of the hardware. The high precision required for prospective motion correction is vulnerable to non-rigid sensor motion relative to the imaged object. The use of a plastic fibre optic cable was not ideal for sensor mounting where the stiff cable could mechanically induce spurious changes in the sensor position. This was however an experimental layout of the hardware which showed very good MRI compatibility where a standoff distance of only 10 mm was sufficient to eliminate most visible image artefacts (Figure 2.5) in the gradient echo sequence implemented. Alternative communication techniques could include wireless electromagnetic approaches which are well outside the operating frequency of the MRI scanner or wireless optical techniques. It is important for the communication protocol to achieve a low latency and high frequency as we noticed angular rates of change as large as 20 dps during 'normal' subject motion which would correlate to 0.15 degrees per TR of the gradient echo sequence implemented in this paper. In order to achieve sub voxel resolution motion correction in structural scans without rejecting any data, one would require exceptionally high temporal resolution sequence updates. The data streamed from the device includes angular rate

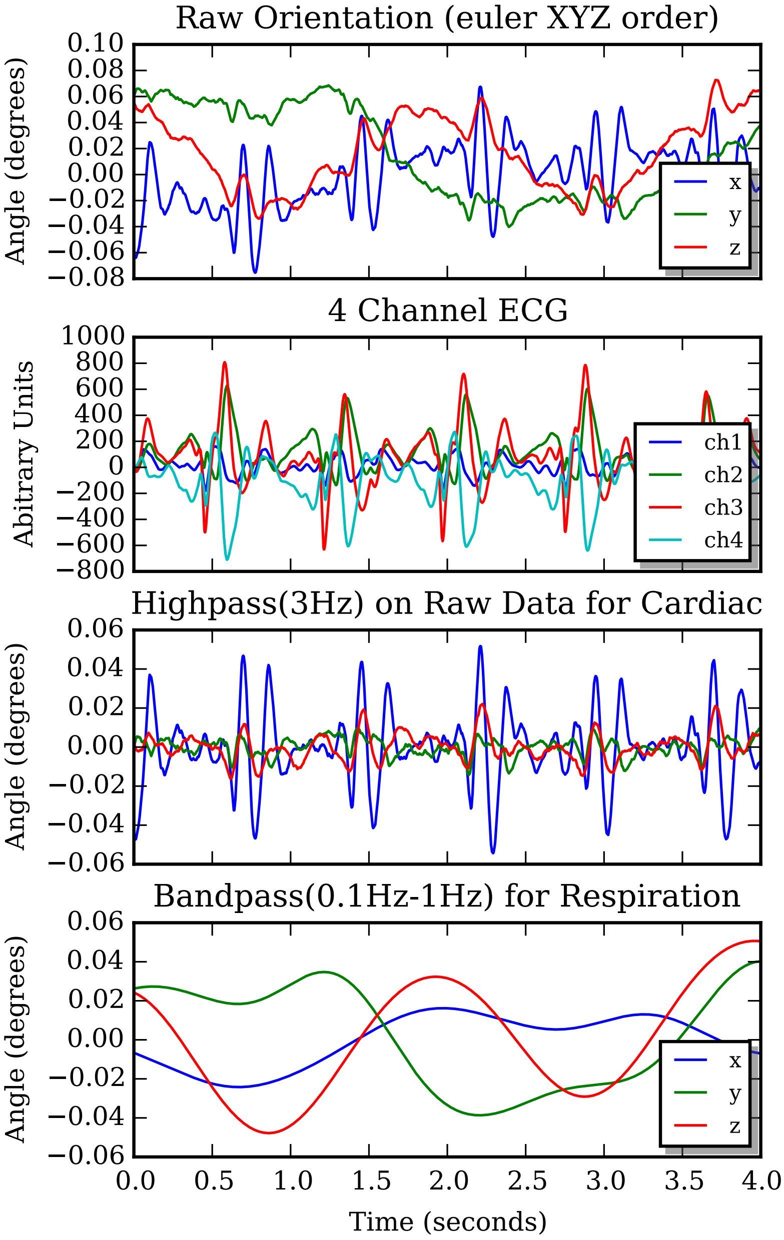

Fig. 2.10 The sensor array is able to pick up a unique patient signature which correlates well with their pulse and respiration. The data presented above was acquired while the MRI scanner was inactive with the marker attached to the subject's forehead. A 3 Hz high-pass filter was selected to reduce base line drift from respiratory motion in the plot of orientation data representing involuntary cardiac motion.

and acceleration which could be used to predict the future position/orientation of the subject for improved performance. There is a strong correlation between the change in the subject's head orientation and the translation of the subject in the field of view. The majority of the subject motion occurs whilst their head remains in contact with the cushion within the MR receiver coil and can be estimated as rolling motion. Cardiac and respiration contribute to pulsatile motion in healthy subjects on the order of 0.14 degrees peak to peak. When imaging the frontal pole that lies approximately 150 mm from the subject's contact point these signals would correspond to voxel blurring over an arc length of 0.4 mm for involuntary motion, highlighting the importance of precise orientation estimation. The high temporal resolution estimates would therefore be well suited for combining with slower navigator based approaches where the orientation estimates, patient motion model and slower navigator data could be combined for a complete prospective motion correction solution.

2.6 Conclusion

The method presented for orientation measurement can be set up in an untouched scanner in a few minutes with no alterations to the scanner hardware. The technique uses mostly consumer grade integrated circuit components and as a result implementation costs were low, less than US$ 1 000 for three completed prototypes as presented here. The method can correct for large changes in orientation at a high temporal resolution (each line of k-space) with minimal impact on the imaging pulse sequence. The method has shown the potential to detect small periodic changes in orientation such as the subject's breathing and pulse which could be valuable for gating of imaging pulse sequences which are susceptible to blood flow or respiration. The calibration free implementation presented has the potential to make prospective motion correction using external hardware more relevant to a clinical environment, where measuring orientation has restricted marker placement and size or is reliant on pulse sequence modifications. The new method (VectOrient) implemented in this work was capable of correcting very rapid motion, achieving a latency of less than 12.7 ms to an accuracy of within 0.8 degrees over +-15 degree rotations. The precision of the angular rate sensor and magnetometer allows the quantification of subject pulse. Most of the latency in the current implementation comes from communication and the sequence update framework, where processing of the sensor signal contributes to less than a millisecond of the total delay. VectOrient would therefore have the potential to ensure robust encoding of the magnitude of the raw MR signal even during high angular rates of change (> 20 dps) if low latency access to the gradient amplifier rotation matrix was made available.

Chapter 3

Self-synchronised measurements of the rate of change of the gradient field.

Abstract

In this work a device is developed that is capable of wireless synchronisation to the pulse sequence time frame with sub-microsecond precision. This is achieved by detecting radio frequency pulses in the parent pulse sequence using a small resonant circuit. The device incorporates a 3 axis pickup coil, that is constructed using conventional printed circuit board (PCB) manufacturing techniques, to measure the rate of change of the gradient waveforms with respect to time. Using Maxwell's equations, assuming negligible rates of change of curl and divergence, a model of the expected gradient derivative (*slew*) vector field is presented. The device includes a 3-axis hall effect magnetometer that allows for the measurement of the direction of the static magnetic field in the device coordinate frame. The magnetometer measurement is combined with the pickup coil voltages and slew vector field model to precisely measure the orientation (0.1 degrees about pickup coil axis) and position (less than 0.1 mm) with a pulse series lasting 880 μs. The gradient pulses are designed to be sinusoidal enabling the detection of a phase shift between the time frame of the pickup coil digitisation circuit and the gradient amplifiers. Signal processing is done by a low power micro-controller on the device and the results are transmitted out of the scanner bore using a low latency 2.4 GHz radio link. The device identified an unexpected 40 kHz oscillation relating to the switching frequency of the gradient amplifiers that is predominantly in the direction of the static magnetic field. The new Radio frequency triggered Wireless Acquisition Device (WRAD) enables users to probe the scanner gradient waveforms with minimal

hardware set-up and shows promise for future developments in prospective motion correction.

3.1 Introduction

Previously authors have described concomitant (Maxwell) gradient fields and the influence they have on image formation in phase contrast MR [32], non-cartesian MR; such as spiral acquisitions [33], diffusion tensor imaging [34] and low field MR ([35], [36], [37]). In these studies the influence of orthogonal gradient fields superimposed on the the static magnetic is of interest as this results in image distortions. In this work we are concerned with the rate of change of the gradient waveforms with respect to time (slew). When measuring the rate of change of the magnetic fields within the scanner the temporally stationary static magnetic field falls away making the component orthogonal to the static magnetic field (which produces concomitant fields) and conventional gradient *slews* equally visible. The slew is therefore a vector quantity which encodes the MRI scanner imaging volume in more than one spatial direction at a time with a single gradient excitation. Theoretically this means that the slew vector more efficiently encodes position than any frequency based technique that resolves the gradient fields into a scalar quantity. This information is useful when tracking subject motion as position and orientation estimates are possible, as is done with the *Endoscout* tracking system [17]. In the *Endoscout* implementation no model is applied to the data, instead a reference dataset is fitted to the sensor (pickup coil) signals using a minimisation algorithm. This can result in unpredictable sensor noise and as a result varying performance based on location in the scanner bore.

Maxwell's equations may be constrained to describe the gradient magnetic fields by assuming negligible curl and zero divergence within the imaging volume. With respect to gradient slew the time derivative of the divergence is zero and we assume negligible change in curl to develop a similar system of equations. By combining the gradient slew vector with a vector observation of the direction of the static magnetic field we show that a closed form solution to displacement and orientation in the gradient co-ordinate frame is possible.

The voltage induced across a 3D pickup coil (which is relatively simple to construct) relates to the slew rate of the gradient waveforms at that instant in time. The hardware used to digitise the pickup potential effectively introduces new analogue to digital (ADC) sampling events defined in the pulse sequence time frame. Preferably the signal acquisition windows are kept very short (<1 ms) to minimise any influence on the parent (imaging) pulse sequence timing. The device is therefore required to be precisely synchronised to the imaging pulse sequence to allow correct interpretation of the gradient waveform derivative (slew). For this purpose most modern MRI scanners have optical synchronisation capabilities allowing external events to be triggered at precise intervals as specified by the pulse sequence programmer. When introducing external hardware, which requires physical connections to the MRI scanner, new challenges arise that can affect the imaging work-flow.

In this work the use of a synchronisation signal from the scanner control computer and the associated cabling is avoided. Instead the detection of the radio frequency (RF) pulses of the parent pulse sequence are used as synchronisation events. A **W**ireless **R**adio frequency triggered **A**nalogue signal acquisition **D**evice (WRAD) is developed. One major advantage of using RF pulses is the ease of portability between different imaging pulse sequences as the RF pulses conveniently define the contrast of the acquisition. RF pulses are detected using a wireless resonant marker tuned to the precession frequency of the MRI scanner. A passive detuning circuit ([11]) is modified to charge a tank capacitor while maintaining effective detuning. In order to communicate the data acquired by the WRAD out of the scanner, a 2.4 GHz radio link is developed. Real-time data visualisation of the acquired signals is possible with short high data-rate packet transfers, avoiding overlap with critical sections of the parent pulse sequence (during sampling of the MR signal). The method is validated by introducing sinusoidal gradient play-outs into the imaging pulse sequence. The potential induced in a 3D printed circuit board (PCB) pickup coil is filtered, amplified, sampled (using a 12-bit ADC) and analysed in real-time using the WRAD's on-board micro-controller. To evaluate the efficacy of the method a 3D spoiled gradient echo pulse sequence is modified to play out 3 sinusoidal pulses, one in each of the gradient axes. The deviation of the phase of the sinusoidal potential induced across the pickup coil on the WRAD and the gradient waveform played out in the pulse sequence time domain are compared to allow real-time measurement of timing offsets between the WRAD and pulse sequence time frames. Once accurate synchronisation is achieved the relationship between position in the gradient co-ordinate frame and the slew vector is examined.

3.2 Theory

For a well constructed MRI scanner we can assume that the gradients are uniform within the imaging volume allowing us to describe the spatially varying magnetic field

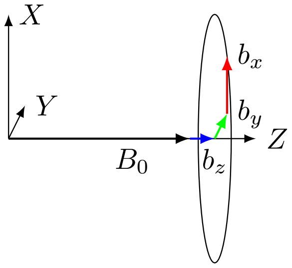

Fig. 3.1 The gradient coordinate system and the resultant magnetic field at an arbitrary point. The b_z component of the gradient fields are referred to as conventional gradients and the orthogonal terms (b_x, b_y) produce the concomitant field. Not drawn to scale.

($\boldsymbol{b}$) by the following general equation (Figure 3.1):

$$\boldsymbol{b} = \frac{\partial \boldsymbol{b}}{\partial \boldsymbol{p}}\boldsymbol{p} + B_0\boldsymbol{z}, \tag{3.1}$$

where $\boldsymbol{p}$ is the position relative to the iso-centre.
The gradient slew can be represented by the scalar derivative of eqn. 3.1 with respect to time:

$$\boldsymbol{s} = \frac{\partial \dot{\boldsymbol{b}}}{\partial \boldsymbol{p}}\boldsymbol{p} + \frac{\partial \boldsymbol{b}}{\partial \boldsymbol{p}}\dot{\boldsymbol{p}} \tag{3.2}$$

The first term is caused by the flux produced due to gradient slew and the second term is proportional to the velocity of the pickup coil through the magnetic field produced by the gradients. Considering the capabilities of a modern MRI scanner with slew rates of hundreds of tesla per metre per second and imaging gradient strengths of tens of milli-tesla per meter ($\frac{\partial \boldsymbol{b}}{\partial \boldsymbol{p}} \ll \frac{\partial \dot{\boldsymbol{b}}}{\partial \boldsymbol{p}}$) it is reasonable to neglect this term. The first term can then be re-written in matrix form:

$$\begin{pmatrix} s_x \\ s_y \\ s_z \end{pmatrix} = \begin{pmatrix} \frac{\partial \dot{b}_x}{\partial x} & \frac{\partial \dot{b}_x}{\partial y} & \frac{\partial \dot{b}_x}{\partial z} \\ \frac{\partial \dot{b}_y}{\partial x} & \frac{\partial \dot{b}_y}{\partial y} & \frac{\partial \dot{b}_y}{\partial z} \\ \frac{\partial \dot{b}_z}{\partial x} & \frac{\partial \dot{b}_z}{\partial y} & \frac{\partial \dot{b}_z}{\partial z} \end{pmatrix} \begin{pmatrix} x \\ y \\ z \end{pmatrix} \tag{3.3}$$

The last row represents the slew parallel to the static magnetic field, a desired result of the conventional imaging gradients which spatially manipulate the precession frequency of the spins for image formation. We can then determine which of the spatially varying slew terms are coupled to ‘imaging’ gradients/slews by considering *Maxwell’s* equations. Assuming negligible change in displacement current and true current densities results in an expected *curl* of $\mathbf{0}$:

$$\nabla \times \dot{\boldsymbol{b}} = \mathbf{0},$$

coupling the following terms:

$$\frac{\partial \dot{b}_x}{\partial z} = \frac{\partial \dot{b}_z}{\partial x} = \dot{g}_x, \quad \frac{\partial \dot{b}_y}{\partial z} = \frac{\partial \dot{b}_z}{\partial y} = \dot{g}_y, \quad \frac{\partial \dot{b}_x}{\partial y} = \frac{\partial \dot{b}_y}{\partial x}.$$

To manipulate the magnitude of the static magnetic field B_0 a gradient slew in the z direction is required. To achieve a field directed along z which spatially varies relative to position in the x direction ($\dot{g}_x$) a perpendicular gradient slew in the x direction which spatially varies relative to the z displacement is required. Similarly to manipulate the field in the z direction with y spatial encoding ($\dot{g}_y$) a secondary slew in the y direction is required which spatially varies relative to z displacement. Intuitively these equations agree with the flux expected from *Golay* coils used in the construction of the X and Y gradients. Neither of the terms in the final equation are useful to image encoding, considering the amount of energy spent on creating the gradient fields it is expected that the gradient design would attempt to minimise these terms $\left(\frac{\partial \dot{b}_x}{\partial y} = \frac{\partial \dot{b}_y}{\partial x} \approx 0\right)$ as they would represent misalignment or asymmetry of the gradient axes. To constrain the remaining terms we incorporate the divergence equation ($\nabla \cdot \dot{\boldsymbol{b}} = \mathbf{0}$) giving:

$$\frac{\partial \dot{b}_x}{\partial x} + \frac{\partial \dot{b}_y}{\partial y} + \frac{\partial \dot{b}_z}{\partial z} = 0$$

Due to the cylindrical symmetry of the MRI scanner we expect that $\left(\frac{\partial \dot{b}_x}{\partial x} = \frac{\partial \dot{b}_y}{\partial y}\right)$, it follows that:

$$\frac{\partial \dot{b}_x}{\partial x} = \frac{\partial \dot{b}_y}{\partial y} = -\frac{\partial \dot{b}_z}{2\partial z} = -\frac{\dot{g}_z}{2}$$

To efficiently encode displacement in the z-direction, a coupled orthogonal slew on the xy plane is required. Using these constraints we can now write Equation 3.3 taking into account the gradient waveforms coupled to those controlled by the pulse sequence designer:

$$\boldsymbol{s} = \mathbf{S}\boldsymbol{p} = \begin{pmatrix} -\frac{\dot{g}_z}{2} & 0 & \dot{g}_x \\ 0 & -\frac{\dot{g}_z}{2} & \dot{g}_y \\ \dot{g}_x & \dot{g}_y & \dot{g}_z \end{pmatrix} \begin{pmatrix} x \\ y \\ z \end{pmatrix} \tag{3.4}$$

The gradients names (g_x, g_y, g_z), that come from the one dimensional encoding they produce for image formation, can be misleading when interpreting the multi-dimensional slew vectors they produce. Interestingly the z-gradient simultaneously encodes displacement in all 3 directions. The x, y gradients produce a slew vector lying on the xz and yz planes respectively. The following spatial encoding vectors, one for each gradient, are introduced for later developments:

$$\boldsymbol{f}^{XZ} = \frac{\boldsymbol{s}^X}{\dot{g}_x} = \begin{pmatrix} z \\ 0 \\ x \end{pmatrix}, \quad \boldsymbol{f}^{YZ} = \frac{\boldsymbol{s}^Y}{\dot{g}_y} = \begin{pmatrix} 0 \\ z \\ y \end{pmatrix},$$

and

$$\boldsymbol{f}^{Zxy} = \frac{\boldsymbol{s}^Z}{\dot{g}_z} = \begin{pmatrix} -\frac{x}{2} \\ -\frac{y}{2} \\ z \end{pmatrix}. \tag{3.5}$$

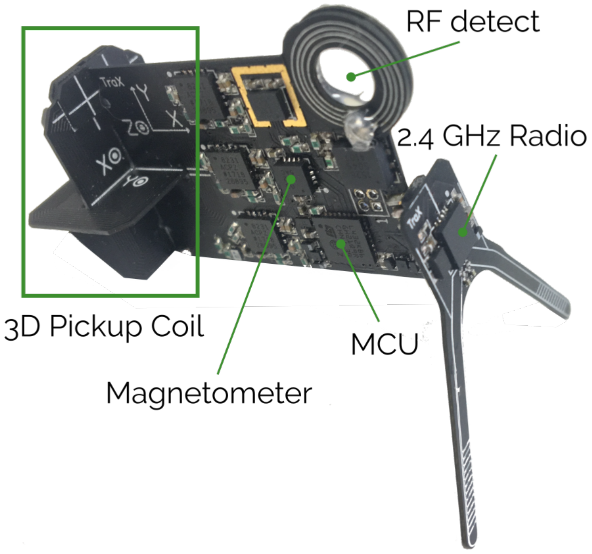

Fig. 3.2 The 2.4 GHz dipole antenna is designed to saddle the bridge of the subject's nose. The main printed circuit board (PCB) would therefore lie close to the sagittal plane. This allows maximum flux for the 2D RF detection antenna. The microcontroller unit (MCU) and analogue circuitry are also on the sagittal plane to minimise cross sectional area relative to the nearest RF receiver elements. The pickup coil is constructed from 3 PCB fabricated inductors (Z axis on the main PCB, X and Y on separate PCBs) each precisely cut with slots to allow them to be mounted mutually orthogonal to each other, representing the principal axes of the WRAD co-ordinate frame.

3.3 Methods

The WRAD hardware was designed and fabricated using standard electronic components, however care was taken in selecting packages that contain minimal nickel. The pulse sequence was implemented on a 3 T Skyra MRI scanner (Siemens, Erlangen, Germany). The device (Figure 3.2) comprises 5 main circuits (excluding the micro-controller):

- The RF detection circuit for producing synchronisation pulses.
- The analogue amplification and filtering circuit for processing the pickup voltages before digitisation.
- The micro-controller with built in 12-bit analog digital converter for signal processing and digital communication with the magnetometer and 2.4 GHz radio.
- The wireless transmission circuit to communicate results out of the MRI scanner.
- The 3-axis hall effect magnetometer for measuring the direction of the static magnetic field.

The device was constructed using a 2-layer printed circuit board 0.6 mm thick, measuring 40 mm over its largest dimension. The device is powered by a rechargeable non-magnetic lithium ion battery (250 mAh). The device draws approximately 35 mA during operation, allowing 3-4 hours of continuous operation without risk of damaging the battery.

3.3.1 RF detection circuit

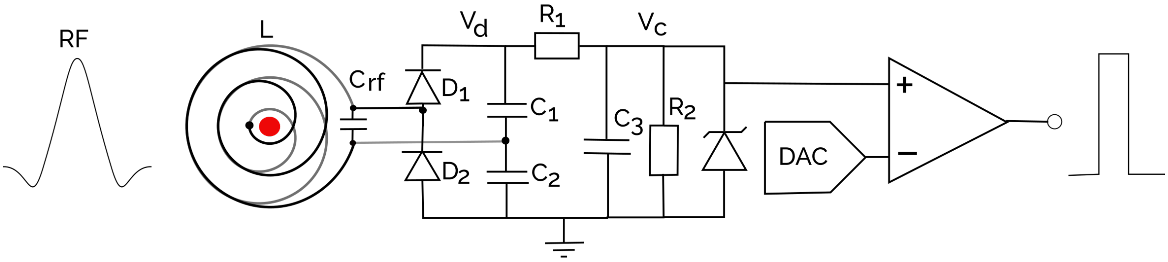

Fig. 3.3 RF detection circuit used to rectify high power radio frequency pulses to trigger ADC events.

A resonant marker (Figure 3.3) comprising a PCB inductor (L) and tuning capacitor (C_{rf}) was constructed. The resonant circuit was tuned using a circular loop connected to handheld antenna analyser. The sample (red dot) was constructed from a glass sphere filled with polyethylene glycol (PEG). The high frequency RF signal is rectified using the diodes (D_1 and D_2) and charging capacitors (C_1 and C_2) which are connected in series, doubling the peak-to-peak AC signal. This configuration is commonly known as a *Delon Doubler*. The doubled potential (V_d) then charges the tank capacitor C_3 through R_1. As the diodes become more conductive the capacitance changes, detuning the resonant portion of the circuit. R_1 controls the charge current of the capacitor and forms a potential divider with R_2. The selection of R_2 controls the discharge rate of C_3 adjusting the pulse width of the detection pulse. The Zener diode protects the comparator in case the divided potential (V_c) exceeds the input threshold. A high speed 12-bit digital to analog converter (DAC) is connected to the negative terminal of the comparator allowing real-time adjustment of the detection threshold. The comparator is built into the microcontroller and has a programmable hysteresis level (15 mV) which, when combined with the low pass nature of the charge circuit, avoids any bouncing of the digital output signal.

3.3.2 Pickup Coil

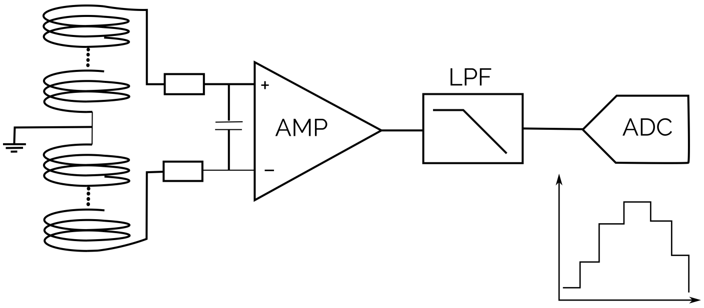

Fig. 3.4 Pickup coil amplification and analogue filter circuit for a single axis.

The pickup coil circuit (Figure 3.4) was designed with 18 turns, 9 on each side of the PCB. An active analogue low pass filter (LPF, 3 pole *Butterworth*) with a cut-off frequency of 32 kHz is applied to the signal before sampling at 200 kHz. The WRAD ADC sample frequency was chosen to align to the gradient raster timing of the scanner. Two ADC samples on the WRAD correspond to one time step in the MRI scanner's gradient raster time frame (10 μs, for our system) so that $N_{\mathrm{WRAD}} = 2N_{\mathrm{GRT}}$. The first pole placed before the instrumentation amplifier (AMP) is used to eliminate any high frequency signals, such as RF, before amplification. The instrumentation amplifier has a programmable gain setting (k) of 1 - 128 in powers of 2.

Flux to induced voltage The design presented in Figure 3.2 represents one of 3 mutually orthogonal planar pickup coils, each measuring the magnitude of the flux normal to its surface (x, y, z). These combined form a 3D slew sensor. The electric field ($\boldsymbol{e}$) induced in a conductor with a time varying field can be described as:

$$\oint_{\partial\Sigma} \boldsymbol{e} \cdot \mathrm{d}\boldsymbol{\ell} = -\frac{\mathrm{d}}{\mathrm{d}t} \iint_{\Sigma} (\boldsymbol{b} + B_0 \boldsymbol{z}) \cdot \mathrm{d}\boldsymbol{a},$$

which for the case of a planar conductor with unit normal $\boldsymbol{n}$, which is wound in a left handed fashion, results in the induced voltage:

$$v = -a\left(\mathbf{S}\boldsymbol{p} \cdot \boldsymbol{n} + [\boldsymbol{b}(\boldsymbol{p}) + B_0\boldsymbol{z}] \cdot \frac{\partial \boldsymbol{n}}{\partial t}\right), \tag{3.6}$$

where a is a constant scaling factor that relates to the geometric properties of the pickup coil and incorporates the instrumentation amplifier gain (k). The second term is as a result of angular rate of change ($\boldsymbol{\omega}$) of the pickup coil in the static magnetic field:

$$\frac{\partial \boldsymbol{n}}{\partial t} = [\boldsymbol{\omega}]_{\times} \boldsymbol{n}, \tag{3.7}$$

where the $[\cdot]_{\times}$ operator converts a vector into a 3 by 3 skew matrix representing the vector cross product.

In this case the static magnetic field is not negligible and the induced voltage could affect results, however the gradient pulses used to induce the potential are generally very short (160 μs, in this work). The expected change in angular rate of change over such a short period is expected to be negligible so that this term can be treated as a small constant offset that can be eliminated or separated for measurement (if a useful 2 axis angular rate sensor is desired).

3.3.3 Pulse Sequence Design

A pulse sequence with sinusoidal waveforms played out in each gradient axis was designed for pickup coil excitation (Figure 3.5). With a gradient raster time of 10 μs, one revolution/period (at 6.25 kHz) of the gradient excitation has a duration of 16 samples. The waveform design ensures perfect symmetry of the discrete waveform with 4 samples for each quarter rotation. An extra quarter rotation before and after each readout window (RX, RY, RZ) ensures the waveform remains sinusoidal if there is an offset between the WRAD sample time and the MRI scanner gradient raster time (40 μs, non-hatched regions Figure 3.5). The initial and final ramp (quarter rotation) of

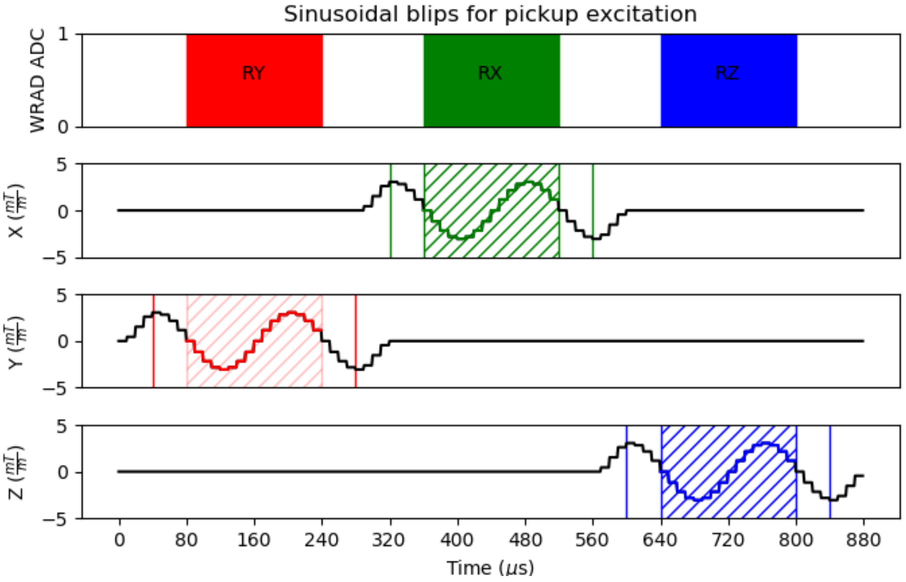

Fig. 3.5 Sinusoidal gradient waveforms lasting a total of 880 μs with highlighted ADC acquisition windows. The hatched regions show the desired ADC timing and the outer bounded regions the maximum allowable timing offset in which the waveforms remain sinusoidal, effectively forming a buffer for any offset between the WRAD and gradient time frames.

each waveform is implemented using a shifted cosine function at double the frequency and half the amplitude, to maintain the designed slew rate of the measured excitation. This ensures that the time derivative of the gradient play-out is smooth, allowing for a linear response from the analogue filter. The results presented were obtained with a peak slew rate of 60 T/m/s with each readout lasting a total of 160 μs (Figure 3.5). All parameters of the waveform are implemented to be user adjustable along with the protocol of the parent pulse sequence.

The gradient excitation waveforms are designed to be identical $(s = \dot{g}_x = \dot{g}_y = \dot{g}_z)$. The MRI scanner therefore produces a spatially varying slew vector field ($\boldsymbol{f}$; Equation 3.5) for each pulse scaled by the time varying function:

$$s(t) = -S\cos(\omega t)$$

where S is the maximum slew rate of the gradient pulse. Each pickup coil of the WRAD observes the slew as a voltage in mutually orthogonal directions which can be combined to form a voltage vector:

$${}^{\mathsf{W}}\boldsymbol{v} = aS\cos(\omega t + \theta)\,{}^{\mathsf{W}}\boldsymbol{f} \tag{3.8}$$

where the leading superscript $\left({}^{\mathsf{W}}\cdot\right)$ denotes the WRAD observation frame and θ models timing offsets between the WRAD time frame and the gradient time frame. The spatial slew encoding vector ($\boldsymbol{f}$) is any combination of the terms ($\boldsymbol{f}^{XZ}$, $\boldsymbol{f}^{YZ}$, $\boldsymbol{f}^{Zxy}$) described in Equation 3.6 rotated into the WRAD reference frame. In the pulse sequence design presented, the simplest case is implemented where one gradient is excited at a time.

3.3.4 Signal processing

The 12-bit ADC samples the potential across the pickup coil for the entire duration of the sinusoidal play-outs discarding the data acquired between the desired acquisition windows (Figure 3.5, RY-RX, RY-RZ). The micro-controller treats the data in quarter rotations ($N_q = 4N_{\mathrm{GRT}} = 8N_{\mathrm{WRAD}}$) in a similar fashion to the pulse sequence design. A *Goertzel* filter is applied to the data in each readout window which isolates the frequency component of the designed waveform ($\frac{2\pi}{4N_{\mathrm{q}}}$). Each filter step is computed on a per sample basis (once every 5 μs) as the pickup potential is sampled. The result is therefore ready for transmission within 5 μs of the last sample of the final readout (RZ). The *Goertzel* filter is a single bin discrete Fourier transform (DFT) computing the phase and amplitude of the tone measured by the pickup coil. Applying the *Goertzel* filter to the induced potential and scaling the result from the proposed pulse sequence waveform shape (Figure 3.5) one obtains the following complex vector:

$$\frac{{}^{\mathsf{W}}\boldsymbol{v}}{aS} \xrightarrow{\mathcal{F}_\omega} {}^{\mathsf{W}}_{c}\boldsymbol{r} = \begin{pmatrix} {}^{\mathsf{W}}f_x \mathrm{e}^{i\theta_x} \\ {}^{\mathsf{W}}f_y \mathrm{e}^{i\theta_y} \\ {}^{\mathsf{W}}f_z \mathrm{e}^{i\theta_z} \end{pmatrix}$$

Translation estimates from pickup voltage To interpret the values obtained from the *Goertzel* filter the spatial encoding vector is first recovered:

$${}^{\mathsf{W}}\boldsymbol{f}_i = \mathsf{abs}\left({}^{\mathsf{W}}_{c}\boldsymbol{r}_i\right) \mathsf{csgn}\left({}^{\mathsf{W}}_{c}\boldsymbol{r}_i\right) \quad \text{for} \quad i = [x, y, z],$$

where $\mathsf{abs}(\cdot)$ is the magnitude of the complex vector and $\mathsf{csgn}(\cdot)$ is the sign of the real component of the complex vector. The 3 readouts RY, RX and RZ (Figure 3.5) produce the following system of equations:

$$
{}^{\mathsf{W}}\boldsymbol{f}^{RX} = {}^{\mathsf{W}}_{\mathsf{G}}\mathbf{R}\begin{pmatrix} z \\ 0 \\ x \end{pmatrix}, \quad {}^{\mathsf{W}}\boldsymbol{f}^{RY} = {}^{\mathsf{W}}_{\mathsf{G}}\mathbf{R}\begin{pmatrix} 0 \\ z \\ x \end{pmatrix},
$$

and

$$
{}^{\mathsf{W}}\boldsymbol{f}^{RZ} = {}^{\mathsf{W}}_{\mathsf{G}}\mathbf{R}\begin{pmatrix} -\frac{x}{2} \\ -\frac{y}{2} \\ z \end{pmatrix}
$$

where ${}^{\mathsf{W}}_{\mathsf{G}}\mathbf{R}$ is a rotation matrix, which transforms a vector from the leading subscript frame to the leading superscript frame. A 3 axis hall effect magnetometer measures the direction of the static magnetic field in the WRAD co-ordinate frame, which when normalised can be interpreted as the principal z-axis of the gradient frame:

$$
\frac{{}^{\mathsf{W}}\boldsymbol{m}}{B_0} = {}^{\mathsf{W}}\bar{\boldsymbol{z}} = {}^{\mathsf{W}}_{\mathsf{G}}\mathbf{R}\,{}^{\mathsf{G}}\bar{\boldsymbol{z}}
$$

Obtaining the x and y axes in the WRAD frame can then be achieved by using the x gradient readout:

$$
{}^{\mathsf{W}}\bar{\boldsymbol{y}} = \frac{\left[{}^{\mathsf{W}}\bar{\boldsymbol{z}}\right]_{\times}{}^{\mathsf{W}}\boldsymbol{f}^{RX}}{\|{}^{\mathsf{W}}\boldsymbol{f}^{RX}\|}, \quad {}^{\mathsf{W}}\bar{\boldsymbol{x}} = \left[{}^{\mathsf{W}}\bar{\boldsymbol{y}}\right]_{\times}{}^{\mathsf{W}}\bar{\boldsymbol{z}} \tag{3.9}
$$

or the y gradient readout:

$$
{}^{\mathsf{W}}\bar{\boldsymbol{x}} = \frac{\left[{}^{\mathsf{W}}\boldsymbol{f}^{RY}\right]_{\times}{}^{\mathsf{W}}\bar{\boldsymbol{z}}}{\|{}^{\mathsf{W}}\boldsymbol{f}^{RY}\|}, \quad {}^{\mathsf{W}}\bar{\boldsymbol{y}} = \left[{}^{\mathsf{W}}\bar{\boldsymbol{z}}\right]_{\times}{}^{\mathsf{W}}\bar{\boldsymbol{x}}. \tag{3.10}
$$

Each of which can be used to form the rotation matrix:

$$
{}^{\mathsf{W}}_{\mathsf{G}}\mathbf{R} = \left[{}^{\mathsf{W}}\bar{\boldsymbol{x}} \quad {}^{\mathsf{W}}\bar{\boldsymbol{y}} \quad {}^{\mathsf{W}}\bar{\boldsymbol{z}}\right],
$$

which gives the (over constrained) position of the WRAD in the gradient coordinate frame $\left({}^{\mathsf{G}}_{\mathsf{W}}\mathbf{R} = {}^{\mathsf{W}}_{\mathsf{G}}\mathbf{R}^{\mathsf{T}}\right)$:

$$
\begin{pmatrix} z \\ 0 \\ x \end{pmatrix} = {}^{\mathsf{G}}_{\mathsf{W}}\mathbf{R}\,{}^{\mathsf{W}}\boldsymbol{f}^{RX}, \quad \begin{pmatrix} 0 \\ z \\ x \end{pmatrix} = {}^{\mathsf{G}}_{\mathsf{W}}\mathbf{R}\,{}^{\mathsf{W}}\boldsymbol{f}^{RY},
$$

and

$$\begin{pmatrix} -\frac{x}{2} \\ -\frac{y}{2} \\ z \end{pmatrix} = {}^{\mathsf{G}}_{\mathsf{W}}\mathbf{R}^{\mathsf{W}}\boldsymbol{f}^{RZ}. \tag{3.11}$$

3.3.5 Wireless Transmission

No RF shielding of any of the electronics is implemented as conductive planes interact with the gradients causing high frequency vibration. This could be unpleasant when mounted on a volunteer's head. This affected the design of the 2.4 GHz antenna, where a ground plane for a monopole antenna was not practical. A V-shaped dipole antenna was therefore designed to fit the form factor of the bridge of the subject's nose. Due to the strict timing requirements of data transmissions, a proprietary RF protocol (*Enhanced Shockburst*, *Nordic Semiconductor*) was implemented, enabling low latency bidirectional communication between the WRAD device and a small transceiver (connected to a laptop) placed through the wave guide. The sinusoidal play-outs are inserted before the parent sequence readout (Figure 3.6). The readouts with very short echo times allow for a strong MR signal to capture using the MRI scanner's ADC and compare to the flux waveforms captured by the WRAD ADC.

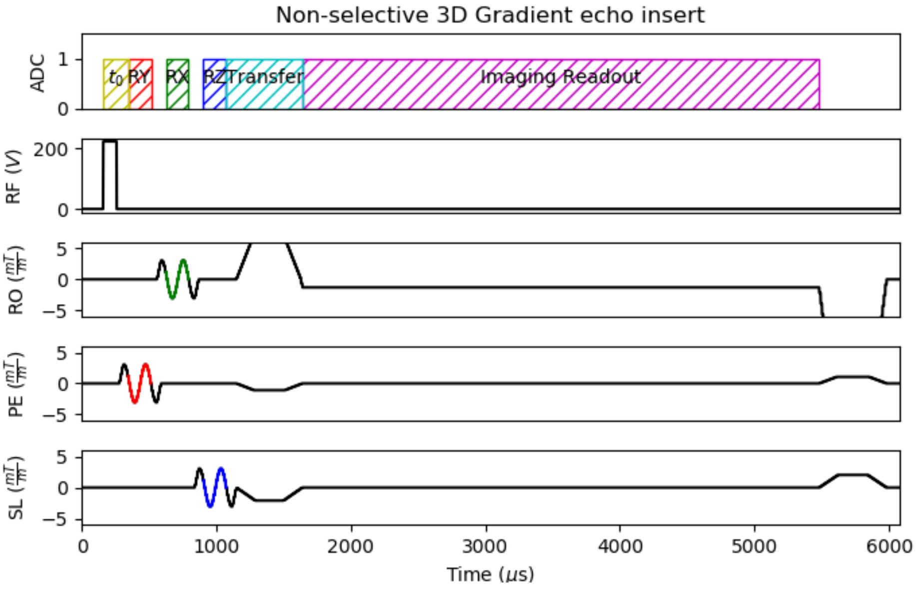

Fig. 3.6 Pulse sequence modification to the gradient echo pulse sequence. The sinusoidal blips are always aligned to the gradient frame. In this case the imaging frame is oriented so that the readout (RO), phase encode (PE) and slice (SL) directions are in the X, Y and Z directions respectively.

The time between the start of the RF pulse and first readout (t_0) is of importance in setting the WRAD RF trigger wait period. The transfer window of 570 μs over the phase encode and pre-wind gradients is sufficiently long for a 32-byte payload transfer and 2-byte acknowledge over the 2.4 GHz radio link. The acknowledge payload for each packet sets the initial wait period t_0 and the number of samples in gradient raster timing (GRT) for each quarter rotation (N_q) of the sinusoidal pulse, effectively enabling real-time adaptation of the pulse sequence parameters (delayed by one TR due to the way in which events are queued by the scanner software). For better pulse sequence co-existence short burst transmissions are preferable, therefore all signal analysis is done on the WRAD in real-time and only the results are transmitted. For debugging purposes a verbose mode was also implemented to allow real-time visualisation of the excitation waveforms, gradient timing offsets, amplitudes and magnetometer measurements; requiring the transmission of 7 packets for each line of k-space.

3.4 Results

Without any modifications/connections to the scanner hardware the WRAD could be used to visualise short snippets of the gradient flux from a variety of different pulse sequences. By implementing a simple plotting program that takes advantage of the bidirectional communication link it is possible to control the acquisition window for repetitive pulse sequences and plot the raw data in an oscilloscope like fashion. The results presented in the following sections were obtained from the modified gradient echo pulse sequence presented in Figure 3.6, enabling the evaluation and interpretation of the flux waveform phase and amplitude as previously discussed.

3.4.1 RF detect

A voltage threshold of 100 mV reliably triggers ADC events on the WRAD down to a flip angle of 12 degrees with a non-selective RF pulse. The ability to adjust detection threshold (sensitivity) allows reliable RF pulse detection over a large range of marker tuning frequencies ($f_0 \pm 10$ MHz) making this technique insensitive to drift in component values. The plot in Figure 3.7 shows the raw data captured over 100 lines of k-space while the WRAD was kept stationary within the scanner. This test presents data from a single pickup coil; orientated such that it measures flux parallel to the static magnetic field. The WRAD manages to achieve high SNR measurements of the gradient slew with exceptionally stable timing. The error bars (a-c) represent 20

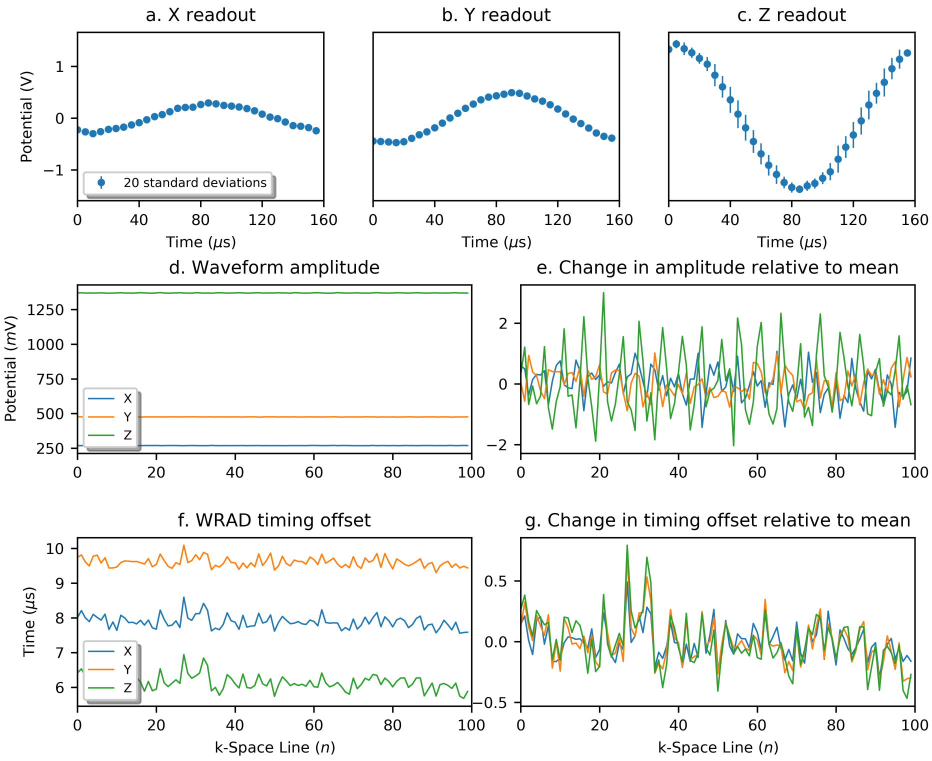

Fig. 3.7 Raw data captured by the WRAD during the play-out of the gradient echo pulse sequence with a non selective RF flip angle of 12 degrees. (a-c) show the mean of each measured potential at each time point over the 100 acquisitions. (d) the amplitude of the result from the single bin discrete Fourier transform of the raw data at each time point (Goertzel algorithm). (e) shows the deviation in amplitude of each data point from the mean in millivolt. (f) the delay estimate computed from the phase of the Goertzel fit in each of the gradient axes. (g) shows the deviation from the mean delay in each axis, more clearly showing the strong correlation between signals.

standard deviations from the mean. The amount of variance in the signals is proportional to the amplitude of the measured voltages (gradient slew), indicating that the variance is likely the result of gradient/signal chain performance as opposed to jitter in the ADC sample timing. The WRAD reliably achieves ADC synchronisation with sub-microsecond precision. The *Goertzel* filter effectively separates the sources of deviations present in the raw waveforms (a-c) with stable amplitude and phase delay measurements (d, f). The change in phase and magnitude of the digitised signals relative to the mean (e, g) indicate robust estimates of both properties when considering the 12-bit ADC resolution is 0.8 mV at a sample frequency of 5 μs. (g) Indicates that the *Goertzel* filter phase detection method can be used for precise inter-gradient delay detection. The periodic spiking fluctuations observed in (e) are well correlated to the phase encoding of the parent pulse sequence.

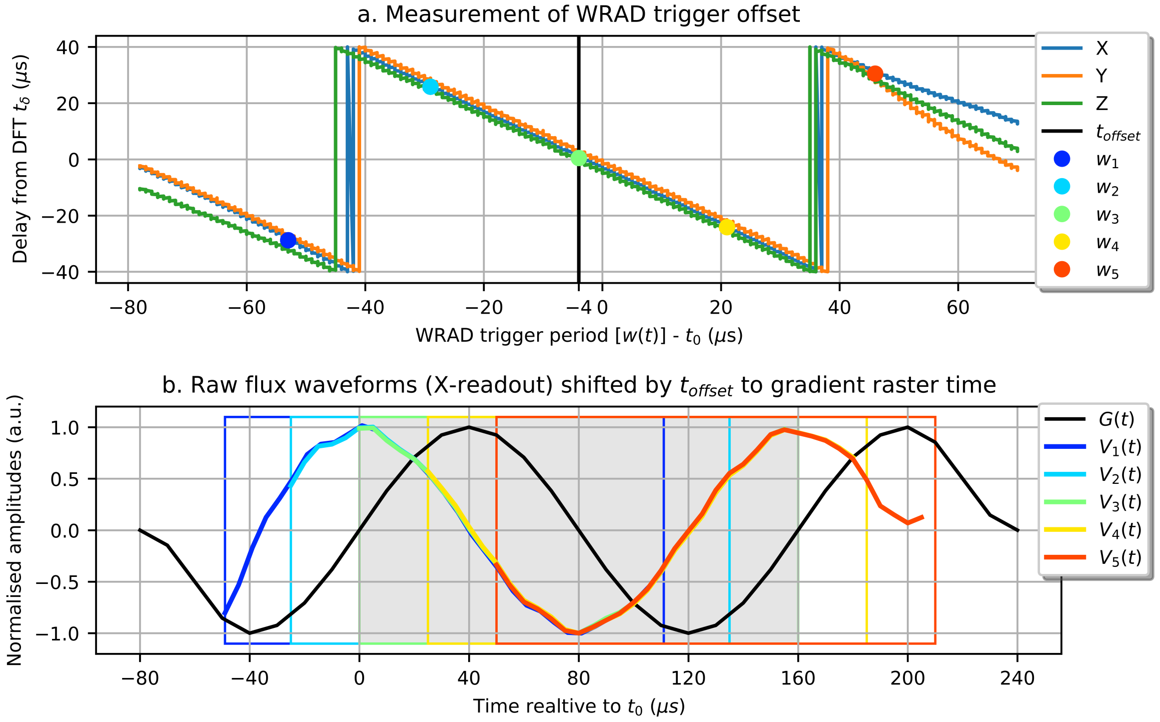

Fig. 3.8 (a) During a pulse sequence play-out the WRAD delay period was adjusted in 1 μs increments using the 2-byte acknowledge payload. (b) 5 flux waveforms (V_{1-5}) with different ADC trigger delays (w_{1-5}, respectively) plotted in the gradient raster time along with the gradient waveform ($G(t)$).

3.4.2 Setting the WRAD trigger period

It is important to ensure the WRAD samples the slew waveform during the period of the gradient pulse which is sinusoidal (non-hatched region Figure 3.5). The delay measurements estimated from the measured voltage phase begin to drift (Figure 3.8a) when the WRAD trigger offset exceeds 40 μs. The deformations of the waveforms at the start of V_1 and the end of V_5 (Figure 3.8b) indicate that the drift is due to overlap of the sinusoidal waveforms (which is expected). Within the readout windows, defined in Figure 3.5, the delay estimates are very stable, precisely tracking the trigger delay adjustments as they are stepped in 1 μs increments. Notice the step like nature of the delay signal obtained from the voltage waveform in Figure 3.8a. At a trigger period t_{offset} of 4 μs shorter than the actual pulse sequence timing (t_0), the WRAD measures a

0 μs phase shift of the pickup potential (w_3, V_3). This corresponds to the phase delay caused by the analog filter which was expected to be 6 μs by design, however passive component tolerances could have influenced the final implementation. From Figure 3.8b it is evident that the slight imperfections in the waveforms are consistent even when the the trigger period is adjusted to capture different portions of the waveform. Interestingly, they are also symmetric indicating that they are the result of small oscillations of the gradient waveform, having the form of an amplitude modulated signal (these imperfections will be revisited later). When considering the time scale of these acquisitions, and that the shape is defined using 16 discrete points, these artefacts could be expected.

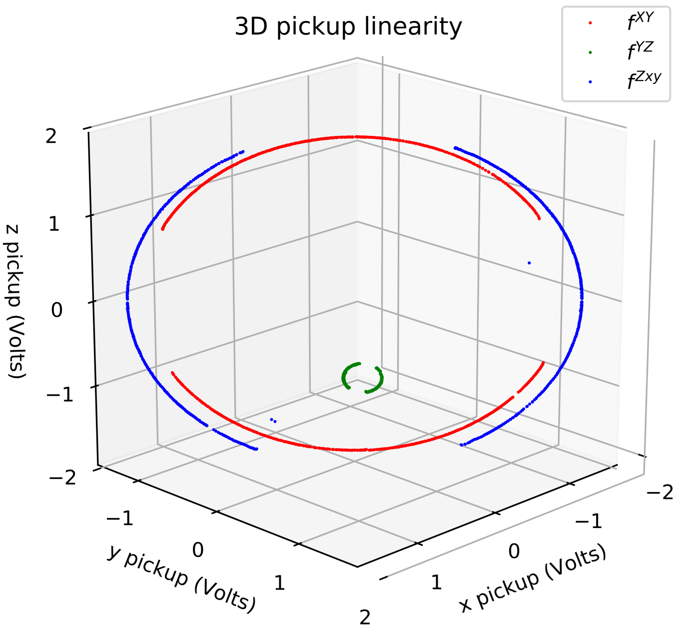

Fig. 3.9 The measured potentials for the x [red, $\left(\boldsymbol{f}^{XZ}\right)$], y [green, $\left(\boldsymbol{f}^{YZ}\right)$] and z [blue, $\left(\boldsymbol{f}^{Zxy}\right)$] gradient play outs plotted in the WRAD coordinate frame. The WRAD was rotated a full revolution about the approximate gradient y-axis at a constant, mostly z, displacement. The WRAD was oriented 45 degrees off of the gradient y-axis to project the slew vectors from each gradient pulse $\left(\boldsymbol{f}^{XZ}, \boldsymbol{f}^{YZ}, \boldsymbol{f}^{Zxy}\right)$ over all 3 pickup coils in the WRAD observation frame.

3.4.3 Linearity of the 3D pickup coil

Figure 3.9 shows very good linearity of the pickup coil assembly; tracing almost perfect circles for each (constant) slew vector. The discontinuous sections (and occasional outliers) of the datasets are regions where the cross sectional area of the planar RF detect coil orthogonal to the static magnetic field ($\vec{B_1}$) was too small to reach the comparator threshold. To quantify the pickup coil performance artificial data points were generated for each real data point using a parametric representation of a circle on the best fit plane (of the entire real dataset for that pickup coil). A linear fit of each pickup coil voltage to the synthesised (perfect) data is presented in Table 3.1. The fitted slopes (column 2) are all close to unity indicating that the 3D pickup coil sensor gives a reliable representation of the slew vector direction and would therefore enable precise orientation estimates when combined with the magnetometer.

readout	dir.	slope	intercept (μV)	stderr (μV)
f^{XY}	x	0.9979	-60.02	85.04
	y	0.9981	75.38	102.60
	z	1.0008	-280.16	68.58
f^{YZ}	x	1.0029	39.51	650.32
	y	1.0033	-30.20	539.93
	z	0.9914	-8.24	460.63
f^{Zxy}	x	0.9983	-310.58	265.26
	y	0.9985	301.91	273.31
	z	1.0037	-18.05	436.35

Table 3.1 Results of linear fits to synthesised points

3.4.4 Relationship between position and the slew vector

To test the relationship described by Equation 3.11 the WRAD device was attached to a Lego block and was first displaced along the x, then y and lastly z direction in 8 mm increments. Figure 3.10 shows the ability of the WRAD to isolate the components of the flux vector using the magnetometer measurement even though it is randomly oriented. The direction of the slew vector from the x gradient ($\boldsymbol{f}^{XY}$) and the magnetometer were used to resolve the slew vector from the y gradient ($\boldsymbol{f}^{YZ}$) into the gradient coordinate system using a rotation matrix derived from Equation 3.9. Similarly, the direction of the slew vector from the y gradient and the magnetometer were used to resolve the slew vector from the x gradient using a rotation matrix derived from Equation

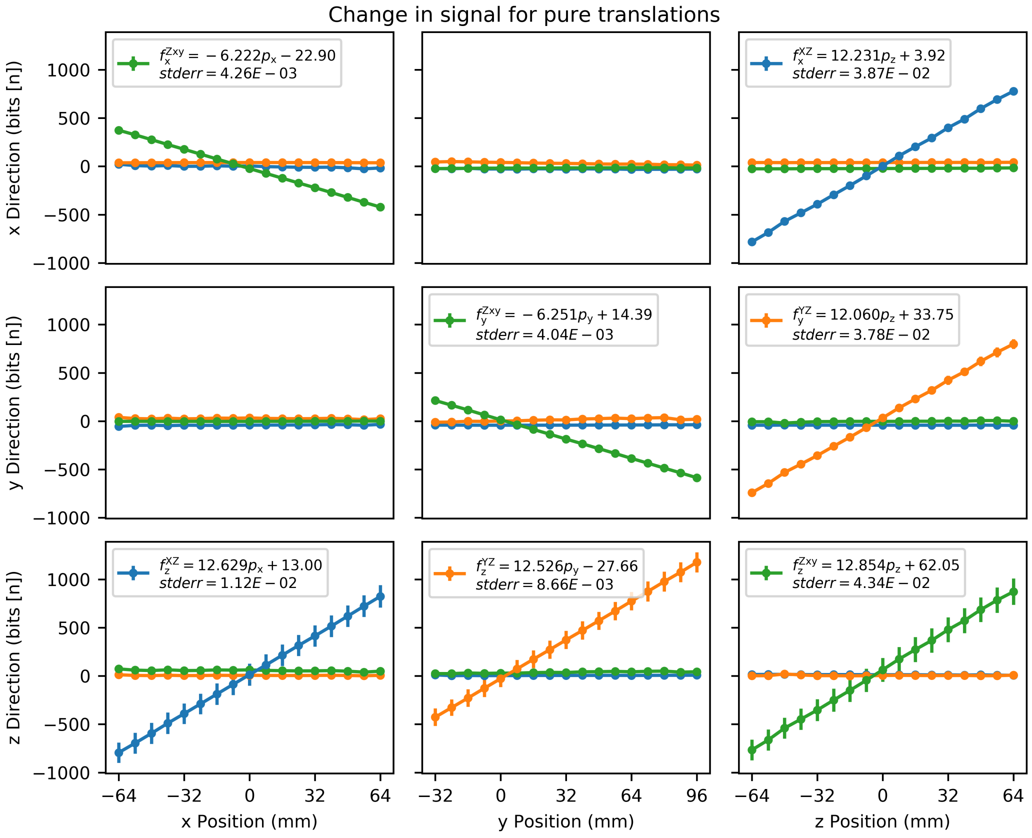

Fig. 3.10 The WRAD (randomly oriented) was independently displaced along the x (column 1), y (column 2) and z (column 3) direction in the gradient coordinate frame. The data acquired from the x (f^{XZ}), y (f^{YZ}) and z (f^{Zxy}) gradient blips are shown in blue, orange and green respectively. All error bars represent 100 standard deviations from the mean.

3.10. By resolving the slew vectors in this way non-orthogonality of the flux vectors produced by the x and y gradients are purposefully projected into the measurements. The small ($< 1\%$) correlation of the measured data with displacement not predicted by Equation 3.4 validates the assumptions made in the slew vector field derivation. Variance in the direction of the slew vectors obtained from the x and y gradients is dependant on the magnitude of the z displacement. Considering Equations 3.9-3.10 the orientation is undefined for a z displacement of 0. For a typical z displacement of 30 mm the orientation of the WRAD is stable to within 0.1 degrees about the z axis from the slew vector estimates, and 0.005 degrees about the orthogonal axes because the magnetometer estimate is exceptionally stable. A vector observation of the flux from the x and y gradients could be combined with an estimate of the direction of gravity from an accelerometer and smoothed using a method such as VectOrient [38] for a more robust implementation (defined for all z). Position estimates accurate to within 0.2 mm are expected based on scaling of the standard error of the individual linear fits (further validation is still required), combining estimates would allow for precision to within 0.1 mm.

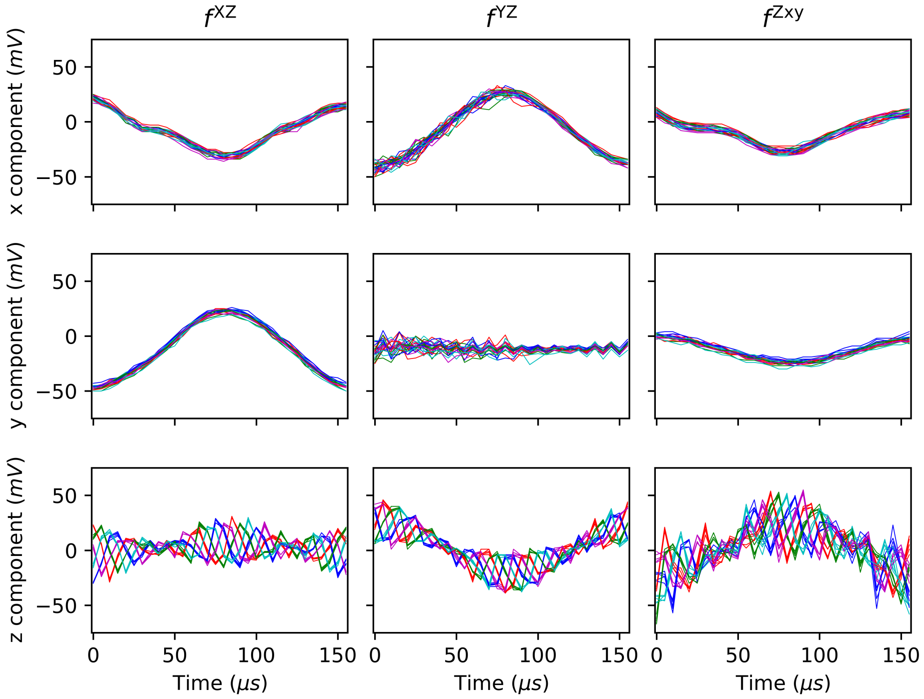

Fig. 3.11 The raw waveforms captured by the WRAD when placed within 2 mm of the iso-centre of the scanner exhibit a 40 kHz ripple originating in the gradient system. The columns represent each of the 3 readouts $\boldsymbol{f}^{XZ}$, $\boldsymbol{f}^{YZ}$ and $\boldsymbol{f}^{Zxy}$ from left to right. The x, y and z components of the slew vector in the MRI scanner coordinate frame are plotted along each row. Every 5^{th} readout is labelled with the same colour. In total 25 readouts are plotted for each of the subplots; 5 of each colour. Notice how repeatable every 5^{th} readout is, aliasing the ripple so that it appears stationary (the plots of each colour overlap with themselves). The component of the slew waveform in the MRI scanner z direction exhibits a more prominent voltage ripple, in the form of an amplitude modulated signal, than the other directions.

Slew vector oscillations predominantly in the z-direction

Figure 3.11 shows the cause of the larger variations in position estimates from the slew component parallel to the static magnetic field (Figure 3.10, bottom row [note the error bars]). All three gradients produce a magnetic field in the z direction. Conversely this means that each gradient coil will induce a current in the other two gradients proportional to the z component of the slew. The orthogonal components of the x and y gradients are uncoupled and more weakly coupled to the z gradient. The super conducting magnet producing the static magnetic field and cylindrical gradient shielding are also more strongly coupled in the z direction. These could be factors which contribute to the oscillations being most visible in the scanner z direction. The ripple was found to be independent of sequence parameters such as TR, bandwidth and slew rate, and position in the scanner bore. The oscillation frequency is 40 kHz and modulated by the requested gradient slew which is best described by the switching of the gradient drivers. The aliasing on every fifth acquisition is caused by an offset of 10 μs between the pulse sequence TR and gradient switching clock. One gradient switching period (40 kHz) corresponds to 2.5 gradient raster periods (100 kHz); the first integer overlap is every fifth shift of one gradient raster period. By ensuring the period between sinusoidal pulses is an integer multiple of 25 μs (40 kHz) the ripple appears stationary and the associated variance in the *Goertzel* filter estimate is eliminated. The gradient pulse width modulation would result in a phase ripple amplitude of 0.0006 rad and would therefore have negligible impact on image formation. The directionality of this signal could, however, be useful as a vector reference (due to its independence of location in the scanner bore) or a time frame synchronisation clock source.

3.5 Discussion

The WRAD reliably and precisely tracks the gradient slew rate using a small 3D pickup coil. The conveniently small and ‘plug and play’ nature of this technique allows researchers to easily capture a variety of signals during MRI experiments. Knowledge of the pulse sequence timing allows smarter co-existence of electronics within the MRI scanner enabling control of when data transmissions occur or powering down oscillators to avoiding overlap with ADC events. Smart sampling of high bandwidth sensors vulnerable to gradient pulses can be achieved during periods of gradient inactivity. This would be beneficial to combined MR-EEG/MR-ECG experiments. The use of the active marker as a signal source for high speed navigators is also possible, opening up sensor fusion strategies for more robust position estimates.

The 3D nature of the gradient slew encodes a wealth of information about the position and orientation of the WRAD within the gradient co-ordinate frame. The addition of a magnetometer allows a computationally efficient way of solving and interpreting the induced potentials. The orthogonal components of the slew vector produced by the gradients are cleaner than the components parallel to the static magnetic field; likely due to coupling effects. Position can be encoded with a single pulse lasting only 240 μs from the z gradient, highlighting the efficiency of position encoding using the slew vector (solving for orientation would be more challenging in this case). The pulse sequence waveforms presented are short, however there is still room for optimisation. Due to the way in which the parallel and orthogonal components of the slew vector are interpreted any slight misalignment between the magnetometer and 3D pickup coil could result in the projection of biases into the position estimate, affecting accuracy. The large amount of data obtained from the 880 μs long excitation pulse series presented, is well suited to sensor fusion techniques (eg. Kalman filter) where magnetometer biases could be tracked and corrected in real time enabling the WRAD to be used for prospective motion correction.

Accurate timing of the MRI scanner hardware is paramount to obtaining the k-space trajectories envisioned by the pulse sequence programmer. If any external hardware is introduced that modifies the way in which the gradient waveforms are played out (such as prospective motion correction), or a time sensitive signal which could affect the interpretation of the MR signal (such as a response to a stimulus in an fMRI experiment or PET MRI), it is important to maintain accurate synchronisation between the scanner and external data acquisition unit as the signal integrity can be degraded due to time frame misalignment. In this work we have presented the design and implementation of a novel self-synchronising probe for use in the MR scanner which can interrogate gradient waveform shape and timing.

Chapter 4

Combining observations of the time varying gradient and static vector fields for complete motion correction.

Abstract

In this work a Wireless Radio frequency triggered Acquisition Device (WRAD) is used for high frequency prospective motion correction in a 3D spoiled gradient echo pulse sequence. The device measures the rate of change in the gradient vector fields (slew) using a three dimensional assembly of Printed Circuit Board (PCB) inductors. The inductor potentials are sampled with an on-board Analogue to Digital Converter (ADC) that is synchronised to the pulse sequence by detecting the RF pulses of the imaging pulse sequence with a small resonant circuit. The static magnetic field is measured using a three axis Hall effect magnetometer. The slew vector encoding is more efficient than traditional MR magnitude based encoding allowing for over constrained measurements of the device's pose within the gradient coordinate frame in only 880 μs. A challenge with measuring the rate of change of the gradient vector field (slew) is the coupling between orientation and position. Small offsets in the orientation can result in large biases of the position estimates. To address this challenge a light-weight Kalman filter is designed that models changes in scaling as a small rotation between the gradient coordinate frame z axis and the static magnetic field, and constant biases as small mechanical misalignments of the gradients that wouldn't influence MR image encoding. The only calibration required is to determine the scaling factor between induced potentials and displacement for the pickup coils, which is specific to the device,

and should therefore be valid in any scanner. The results when using the device to perform prospective motion correction in 3 subjects are presented. In the first subject an increased Average Edge Strength (AES) over all the slices of 4.5% was achieved for very little motion. Next, a subject was asked to move in a way that is typical of patient discomfort. A drop in AES of only -6% was measured with motion correction on, as opposed to -33% when no motion correction was applied. The final subject was asked to move frequently (approximately 90 times) destroying the uncorrected scan (AES -47.3%). Finer cortical folding is still clear with the motion corrected scan (AES -9.4%), maintaining diagnostic value. This new approach is simple to set up and use with well defined measurement variance. Our initial results suggest that the WRAD could enable ‘plug and play’ prospective motion correction.

4.1 Introduction

Due to temporal resolution limitations in navigator based approaches researchers have developed a variety of external hardware based technologies for detecting and correcting motion in real-time. The goal is to develop a motion correction technique that does not influence the imaging pulse sequence, has no impact on the conventional imaging work-flow and does not increase the noise floor of the scanner with measurement uncertainty. Some modern prospective motion correction methods have been shown to reduce overall system uncertainty by accounting for involuntary motion associated with slow drift, increasing the system SNR if you treat this motion as noise (Schulz et al. [25]). The previously mentioned goals are, however, difficult to achieve and as a result all current state of the art approaches compromise on at least one.

Optical motion tracking based approaches ([13]) are fully sequence independent and remarkably accurate, however, they measure subject pose in an independent measurement frame, increasing the complexity of hardware set-up and removal. Although this challenge has been addressed through improved cross-calibration procedures ([15]) or smarter image reconstruction ([39]), which reduces any extra workload on MRI technologists, these methods are still inherently vulnerable to camera positioning and can degrade image quality if not properly anchored. This combined with the need to see the patient (considering the current trend in receiver coils with more channels covering more of the patient’s face) poses a hardware design challenge.

Nuclear Magnetic Resonance (NMR) field probe methods ([40]) overcome some of the cross-calibration challenges by measuring subject pose using the gradient spatial encoding and don’t require line of sight to detect the markers. By using the gradients and

MR signal these methods are inherently coupled to the pulse sequence and generally require pulse sequence modifications for robust pose encoding ([23]). However, it has recently been shown that some 3D pulse sequences possess enough pulse diversity to allow a form of pseudo self navigation that is sufficient for correction of very small patient motion ([12]). The NMR markers take advantage of an independent RF transmit and receive chain so that their position can be interrogated during short snippets of the imaging pulse sequence. This does, however, come at the cost of increased mechanical complexity, wired probes and sensitive RF electronics. Introducing an independent measurement system will also require some form of cross-calibration, where a frequency offset is equivalent to a mechanical misalignment of the sensor frame.

In this work we are concerned with measuring the rate of change of the gradient flux. The gradient time derivative (slew) is independent of the MR signal which eliminates the need for external RF pulses and can be detected using loop inductors resulting in reduced hardware complexity. Cross-calibration is simplified because the gradient spatial encoding is measured directly. This method differs from any MR signal based approach in that the full gradient spatial encoding is visible, not just the component parallel to the static magnetic field. Each ‘conventional’ gradient field used for MR spatial encoding is coupled to an equally strong, accurate and more stable (due to less inter-gradient coupling) magnetic field which encodes displacement in an orthogonal direction. In measuring the rate of change of the gradient waveform this encoding becomes visible (no longer superimposed on the much stronger static magnetic field). An implication of this is that almost any pulse sequence should have the pulse diversity required for pseudo self navigation. Although this aspect is not addressed in this work, the feasibility of achieving full 6 degree-of-freedom pose estimates with only 2 unique gradient pulses is tested. The most difficult aspect in slew vector based pose tracking lies in resolving the vector measurement into the gradient coordinate frame; the precise orientation of the device frame is required before position estimates are possible making this approach more susceptible to bias and increased measurement variance. Interpreting the voltage waveforms in an unknown frame is non-trivial and requires numerical methods to fit the data for each acquisition to a 3 dimensional gradient field map ([17]). In this work it is shown that the gradient map can be avoided by combining a 3 axis magnetometer, which resolves the orientation of a device in the gradient coordinate frame except in the degree of freedom about the axis of the static magnetic field ([38]), with a 3 axis pickup coil to fully resolve orientation and position in the gradient coordinate frame. These complementary sensors are fused using a *Kalman* filter that takes advantage of a linear gradient slew vector field model to enable line-by-line pose estimates. All sensors are incorporated into a single, small, wireless device which self synchronises to the imaging pulse sequence time domain by detecting RF pulses with a small resonant circuit. The Wireless Radio frequency triggered Acquisition Device (WRAD), uses the over-constrained nature of the vector observations to estimate system biases. In the current work 3 sinusoidal blips are inserted into the pulse sequence (lasting 880 μs, per TR) making this and the pose feedback the only pulse sequence modifications. The hardware set up required is mounting the WRAD to the subject and placing a wireless receiver through the wave guide.

4.2 Theory and Methods

A means of efficiently combining the sensor signals captured by the WRAD is important to its efficacy. The gradients and sensors are not perfect. When combining a 3D pickup coil that directly probes the gradients with a *Hall* effect magnetometer that probes the superposition of magnetic fields there is a unique opportunity to track gradient and sensor biases in real-time. The models presented are designed to be computationally light-weight to enable a low latency embedded implementation.

4.2.1 Observation frames

In prospective motion correction the change in the local frame (${}^{L}\cdot$) with respect to the (physical) gradient frame (${}^{G}\cdot$) is of interest. The local frame is the measurement frame of the WRAD (rigidly attached to the subject). The gradient frame is defined by the principle directions in which the x, y and z gradient coils manipulate the magnitude of the magnetic field for image formation. For a patient in the head first supine position, the gradient frame is oriented so that ${}^{G}\mathbf{z}$ represents head to foot (HF), ${}^{G}\mathbf{y}$ is posterior to anterior (PA) and ${}^{G}\mathbf{x}$ is right to left (RL) for our system (3T Skyra, Siemens Erlangen, Germany). For the derivation of the filter equations it is convenient to define an intermediate reference frame (${}^{M}\cdot$), which we call the magnet frame. The magnet frame is defined to have a z-axis that is perfectly aligned to the WRAD's observation of the MRI scanner's static magnetic field. The transform of a vector from the gradient frame to the local frame can then be described by the following two rotations:

$$ {}^{L}_{G}\mathbf{R} = {}^{L}_{M}\mathbf{R}{}^{M}_{G}\mathbf{R}. \tag{4.1} $$

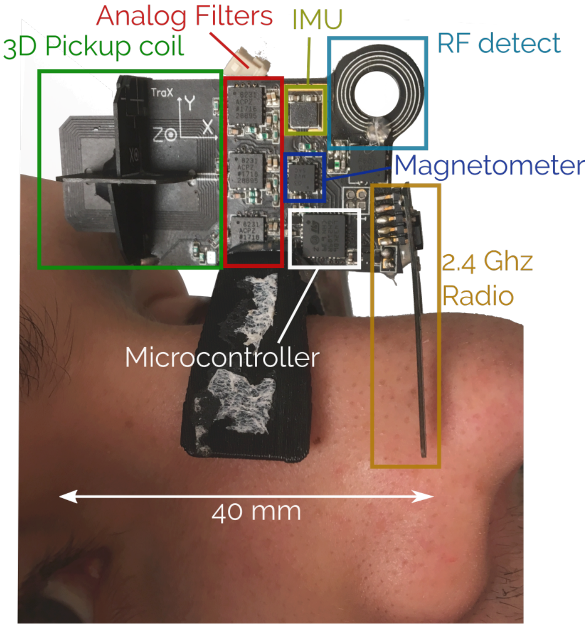

Fig. 4.1 The WRAD mounted on the bridge of a subject's nose. (RF detect) is used to synchronise to the pulse sequence time domain allowing the (microcontroller) to sample the potential induced by the time varying gradient magnetic fields in the (3D pickup coil) assembly. The signals are filtered (analog filters) before being digitised. The (IMU) integrated circuit combines an angular rate sensor and accelerometer. The *Hall* effect (magnetometer) is used to measure the direction of the static magnetic field. The (2.4 GHz radio) is used to transmit the acquired data out of the scanner bore for prospective motion correction feedback.

The gradient z-axis and MRI scanner static magnetic field are expected to be closely aligned with negligible axial deviation; the rotation ${}^{M}_{G}\mathbf{R}$ is therefore a *small* rotation about the x and y axes that models a slight curl of the static magnetic field, gradient frame misalignments and, (indirectly) magnetometer biases. This transform can be represented as a rotation vector $\boldsymbol{\alpha}$:

$$ {}^{M}_{G}\mathbf{R} = \mathbf{I} - [\boldsymbol{\alpha}_{\times}] = \mathbf{I} - \begin{pmatrix} 0 & \alpha_z & -\alpha_y \\ -\alpha_z & 0 & \alpha_x \\ \alpha_y & -\alpha_x & 0 \end{pmatrix} \tag{4.2} $$

where $\alpha_z = 0$. To define this transform a 2 dimensional state vector $\boldsymbol{m}$ is introduced:

$$ {}^{M}_{G}\mathbf{R} = \mathbf{I} - \mathbf{M}(\boldsymbol{m}), \quad \mathbf{M}(\boldsymbol{m}) = \begin{pmatrix} 0 & 0 & -m_1 \\ 0 & 0 & m_0 \\ m_1 & -m_0 & 0 \end{pmatrix} \tag{4.3} $$

The transform ${}^{L}_{M}\mathbf{R}$, as with all rotations, can be broken up into two orthogonal rotations. The Algerbraic QUAternion (AQUA) algorithm presented by [41] effectively decouples two vector observations to form an orientation estimate. Here a similar decoupling is achieved. The transform is broken up into a pure z-axis rotation ${}^{M'}_{M}\mathbf{R}$, observed by measuring the component of the changing gradient field vector orthogonal to the static magnetic field (XY plane), followed by a rotation about a vector on the xy plane ${}^{L}_{M'}\mathbf{R}$, which is observed by measuring the direction of the static magnetic field (Z), so that:

$${}^{L}_{M}\mathbf{R} = {}^{L}_{M'}\mathbf{R}\,{}^{M'}_{M}\mathbf{R}$$

where:

$${}^{M'}_{M}\mathbf{R} = \begin{pmatrix} \cos(\beta) & -\sin(\beta) & 0 \\ \sin(\beta) & \cos(\beta) & 0 \\ 0 & 0 & 1 \end{pmatrix} = \mathbf{N}(\boldsymbol{n}) + \mathbf{I}_z, \tag{4.4}$$

$$\mathbf{N}(\boldsymbol{n}) = \begin{pmatrix} n_0 & -n_1 & 0 \\ n_1 & n_0 & 0 \\ 0 & 0 & 0 \end{pmatrix}, \quad \mathbf{I}_z = \begin{pmatrix} 0 & 0 & 0 \\ 0 & 0 & 0 \\ 0 & 0 & 1 \end{pmatrix},$$

and:

$${}^{L}_{M'}\mathbf{R} = \mathcal{R}\left({}^{L}_{M'}\boldsymbol{q}\right), \quad {}^{L}_{M'}\boldsymbol{q} = \begin{pmatrix} {}^{L}_{M}q_w \\ {}^{L}_{M}q_x \\ {}^{L}_{M}q_y \\ 0 \end{pmatrix}, \tag{4.5}$$

which is more intuitively written in quaternion form (q_w is the scalar and q_{x-z} are the vector components of the unit quaternion of rotation; notice that the z vector component is 0). The operator is given by:

$$\mathcal{R}\left(\boldsymbol{q}\right) = \begin{pmatrix} q_w^2 + q_x^2 - q_y^2 + q_z^2 & 2(q_x q_y - q_w q_z) & 2(q_x q_z + q_w q_y) \\ 2(q_x q_y + q_w q_z) & q_w^2 - q_x^2 + q_y^2 - q_z^2 & 2(q_y q_z - q_w q_x) \\ 2(q_x q_z - q_w q_y) & 2(q_y q_z + q_w q_x) & q_w^2 - q_x^2 - q_y^2 + q_z^2 \end{pmatrix}. \tag{4.6}$$

4.2.2 Observation of the static magnetic field

The WRAD incorporates a 3 axis *Hall* effect magnetometer to observe the superposition of the magnetic fields within the scanner bore (${}^{L}\boldsymbol{b}$). Since this measurement is dominated by the static magnetic field, once normalised it represents the rotation of

Eq. 4.5 acting on the magnet frame z axis:

$$ {}^{L}\hat{\boldsymbol{b}} = \frac{{}^{L}\boldsymbol{b}}{B_0} = \mathcal{R}\left({}^{L}_{M'}\boldsymbol{q}\right){}^{M'}\mathsf{z}, \tag{4.7} $$

where:

$$ {}^{M'}\mathsf{z} = {}^{M}\mathsf{z} = \begin{pmatrix} 0 \\ 0 \\ 1 \end{pmatrix}, $$

because the rotation ${}^{M'}_{M}\mathbf{R}$ is a pure z-axis rotation. B_0 is the magnitude of the static magnetic field. Rewriting $\mathcal{R}\left({}^{L}_{M'}\boldsymbol{q}\right)$ using 4.6, gives the following system of equations:

$$ \begin{aligned} {}^{L}\hat{b}_x &= 2{}^{L}_{M}q_w{}^{L}_{M}q_y \\ {}^{L}\hat{b}_y &= -2{}^{L}_{M}q_w{}^{L}_{M}q_x \\ {}^{L}\hat{b}_z &= {}^{L}_{M}q_w^2 - {}^{L}_{M}q_x^2 - {}^{L}_{M}q_y^2 \end{aligned} \qquad . $$

The solution with a valid quaternion of rotation $\|\boldsymbol{q}\| = 1$ and a positive scalar component (λ) is:

$$ {}^{L}_{M}\boldsymbol{q} = \begin{pmatrix} \lambda \\ -\frac{{}^{L}\hat{b}_y}{2\lambda} \\ \frac{{}^{L}\hat{b}_x}{2\lambda} \\ 0 \end{pmatrix}, \quad \lambda = \sqrt{\frac{{}^{L}\hat{b}_z + 1}{2}} \tag{4.8} $$

The z axis of the local frame lies close to the sagittal plane (Figure 4.1) due to how the WRAD is mounted to the subject. The singularity at ${}^{L}\hat{b}_z$ = -1 would therefore only occur if the subject had rolled their head 90 degrees about the y (posterior-anterior) axis; which is highly unlikely in modern head receiver coils.

4.2.3 Observation of the time varying gradient magnetic field

The gradient fields used for image formation are 3 dimensional vector fields. The component of the gradient fields that lie parallel to the static magnetic field produce the spatial encoding used for image formation. According to *Maxwell's* equations, a linearly varying magnetic field with only a z-component doesn't exist. As a result the spatial encoding produced by the imaging gradients is more complex. Typically the non-z gradient fields have only a small influence on the magnetic field strength because their effect is drowned out by the much stronger static magnetic field, and are often ignored. For the rate of change of magnetic fields within the imaging volume the static magnetic field falls away. In this work this property is advantageous because now the non-z as well as the ‘conventional’ z spatial encoding can be measured. By assuming linear gradients and, negligible rates of change of curl and divergence one can use *Maxwell's* equations to derive the following *slew* vector field model:

$$^{G}\boldsymbol{v} = \mathbf{S}\boldsymbol{p} + \boldsymbol{c} + \boldsymbol{w}_g, \tag{4.9}$$

where,

$$\mathbf{S} = \begin{pmatrix} -\frac{s^z}{2} & 0 & s^x \\ 0 & -\frac{s^z}{2} & s^y \\ s^x & s^y & s^z \end{pmatrix}, \quad \boldsymbol{p} = \begin{pmatrix} x \\ y \\ z \end{pmatrix}, \quad \boldsymbol{c} = s^x \begin{pmatrix} 0 \\ 0 \\ o_z^x \end{pmatrix} + s^y \begin{pmatrix} 0 \\ 0 \\ o_z^y \end{pmatrix} + s^z \begin{pmatrix} o_x^z \\ o_y^z \\ 0 \end{pmatrix}.$$

The change in the x, y and z gradients produce the slew terms s^x, s^y and s^z, respectively. We refer to S as the encoding matrix which encodes position ($\boldsymbol{p}$) in the gradient coordinate frame. It is assumed that the z-component of the slew vector for each gradient should have negligible mechanical misalignment for correct image formation. The mechanical offset vector ($\mathbf{c}$) is therefore modelled as follows. The terms o_z^x and o_z^y model axial misalignments (along z) of the x and y gradient coils relative to the z gradient coil. The terms o_x^z and o_y^z model any off-axial misalignments (on the xy plane) of the z gradient coil relative to the x and y gradient coils. A current ripple artefact, likely caused by gradient switching, produces a unique noise signature of the slew vector field in the MRI scanner z axis direction. The uncertainty in the gradient pulse waveform ($\boldsymbol{w}_g$) is therefore modelled with cylindrical symmetry:

$$\boldsymbol{w}_g = \begin{pmatrix} w_\perp \\ w_\perp \\ w_\parallel \end{pmatrix}. \tag{4.10}$$

The off-axial (orthogonal) slew directions are generally smoother ($w_\perp < w_\parallel$). The WRAD, placed within the imaging volume, measures the instantaneous slew vector from the potential induced in 3 orthogonal pickup coils that define the basis set of the local coordinate frame. Each pickup coil has an independent amplification and filter circuit. The voltage induced in the pickup coils represents the encoded position of the pickup coil assembly from Eq. 4.9 scaled by a factor (κ) that is related to the gain of the amplifier circuit and geometric properties (cross sectional area of the pickup coils and number of turns):

$$ {}^{L}\boldsymbol{z} = {}^{L}_{G}\mathbf{R}\kappa\,{}^{G}\boldsymbol{v} + {}^{L}\boldsymbol{w}_{p}, \quad {}^{L}_{G}\mathbf{R} = {}^{L}_{M'}\mathbf{R}\,{}^{M'}_{M}\mathbf{R}\,{}^{M}_{G}\mathbf{R} \tag{4.11} $$

where:

$$ {}^{L}\boldsymbol{w}_{p} = w_{p}\begin{pmatrix}1\\1\\1\end{pmatrix}. $$

The term $\boldsymbol{w}_p$ represents the noise introduced by sampling each of the pickup coils. In Eq. 4.11 the potential induced across each of the pickup coils that relates to angular rate of change of the WRAD ($\boldsymbol{\omega}$) in the static magnetic field:

$$ emf = B_{0}\text{z}\cdot[\boldsymbol{\omega}\times\boldsymbol{n}], \tag{4.12} $$

is not shown. This is because these potentials are removed with temporal filtering techniques. The change in angular rate over very short readouts is close to zero, hence the angular rate emf would appear as a constant offset during a short time varying waveform. The × operator represents the vector cross product and $\boldsymbol{n}$ is the unit normal of the pickup coil scaled by a geometric scaling factor.

4.2.4 Measurement update in an intermediate reference frame

The measurement obtained from the 3D pickup coil (Eq. 4.11) is transformed into the intermediate (magnet) coordinate frame by using the transform derived from the magnetometer observation of the static magnetic field (Eq. 4.8):

$$ {}^{M'}\boldsymbol{z} = {}^{M'}_{L}\mathbf{R}\,{}^{L}\boldsymbol{z} = {}^{M'}_{M}\mathbf{R}\,{}^{M}_{G}\mathbf{R}\left(\kappa\,{}^{G}\boldsymbol{v}\right) + \boldsymbol{w}_{s}, \tag{4.13} $$

This reduces the degrees of freedom in the pickup coil measurement (note that now the z component of the pickup coil vector is now the 'conventional' gradient encoding used for image formation). The matrix ${}^{M}_{G}\mathbf{R}$ accounts for any biases in this transform. The uncertainties of Eq. 4.11 and Eq. 4.13 are combined into a single term:

$$ \boldsymbol{w}_{s} = {}^{M'}_{M}\mathbf{R}\,{}^{M}_{G}\mathbf{R}\left(\kappa\boldsymbol{w}_{g}\right) + {}^{M'}_{L}\mathbf{R}\boldsymbol{w}_{p}. $$

In the noise model the small rotation ${}^{M}_{G}\mathbf{R}$ is approximated by $\mathbf{I}$ so that:

$$ \boldsymbol{w}_{s} \approx {}^{M'}_{M}\mathbf{R}\kappa\boldsymbol{w}_{g} + \boldsymbol{w}_{p} = \kappa\boldsymbol{w}_{g} + \boldsymbol{w}_{p}, $$

where ${}^{M'}_{M}\mathbf{R}$ has no effect on $\boldsymbol{w}_g$ due to the axial symmetry. Finally, the noise is injected as normally distributed Gaussian white noise with a combined covariance matrix as follows:

$$\boldsymbol{\Sigma}_s = \kappa \begin{pmatrix} \sigma_\perp^2 & 0 & 0 \\ 0 & \sigma_\perp^2 & 0 \\ 0 & 0 & \sigma_\parallel^2 \end{pmatrix} + \sigma_p^2 \mathbf{I} \tag{4.14}$$

Eq. 4.13 is now written in terms of the matrices N (Eq. 4.3), M (Eq. 4.4) and S (Eq. 4.9) for the derivation of update equations for the *Kalman* filter:

$${}^{M'}\boldsymbol{z} = [\mathbf{I}_z + \mathbf{N}(\boldsymbol{n})][\mathbf{I} - \mathbf{M}(\boldsymbol{m})][\mathbf{S}\boldsymbol{p} + \boldsymbol{c}(\boldsymbol{o})] + \boldsymbol{w}_s. \tag{4.15}$$

The vectors $\boldsymbol{m}$ (axial misalignment), $\boldsymbol{n}$ (orientation about the magnet z-axis), $\boldsymbol{p}$ (position in the gradient frame) and $\boldsymbol{o}$ (gradient mechanical offsets) are the states required to solve for the change in subject pose during the image acquisition. The encoding matrix S and mechanical offset $\boldsymbol{c}$ from Eq. 4.9 are constructed from the time derivative of the pulse sequence waveform which is pre-determined by the pulse sequence design. By considering the partial derivative of the measurement with respect to the selected state vectors (*please note that the co-ordinate frame notation is dropped so that* ${}^{M'}\boldsymbol{z}$ is $\boldsymbol{z}$):

$$\frac{\partial \boldsymbol{z}}{\partial \boldsymbol{m}} = [\mathbf{I}_z + \mathbf{N}]\frac{\partial \mathbf{M}}{\partial \boldsymbol{m}}[\mathbf{S}\boldsymbol{p} + \boldsymbol{c}] = \mathbf{H}_m$$

$$\frac{\partial \boldsymbol{z}}{\partial \boldsymbol{n}} = \frac{\partial \mathbf{N}}{\partial \boldsymbol{n}}[\mathbf{I} - \mathbf{M}][\mathbf{S}\boldsymbol{p} + \boldsymbol{c}] = \mathbf{H}_n$$

$$\frac{\partial \boldsymbol{z}}{\partial \boldsymbol{p}} = [\mathbf{I}_z + \mathbf{N}][\mathbf{I} - \mathbf{M}]\mathbf{S} = \mathbf{H}_p$$

$$\frac{\partial \boldsymbol{z}}{\partial \boldsymbol{c}} = [\mathbf{I}_z + \mathbf{N}][\mathbf{I} - \mathbf{M}]\frac{\partial \mathbf{c}}{\partial \boldsymbol{o}} = \mathbf{H}_c \tag{4.16}$$

it is possible to project the error covariance of each state into the same measurement space. The combined measurement covariance can then be written as:

$$\boldsymbol{\Sigma} = \boldsymbol{\Sigma}_s + \mathbf{H}_m\mathbf{P}_m\mathbf{H}_m^\mathsf{T} + \mathbf{H}_n\mathbf{P}_n\mathbf{H}_n^\mathsf{T} + \mathbf{H}_p\mathbf{P}_p\mathbf{H}_p^\mathsf{T} + \mathbf{H}_c\mathbf{P}_c\mathbf{H}_c^\mathsf{T}, \tag{4.17}$$

where the error covariance of each state vector is updated independently through the *Kalman* equations. Firstly the residual is calculated:

$$\boldsymbol{y} = \boldsymbol{z} - [\mathbf{I}_z + \mathbf{N}(\boldsymbol{n})][\mathbf{I} - \mathbf{M}(\boldsymbol{m})][\mathbf{S}\boldsymbol{p} + \boldsymbol{o}], \tag{4.18}$$

then the *Kalman* gain is computed:

$$\mathbf{K}_\lambda = \mathbf{P}_\lambda \mathbf{H}_\lambda \mathbf{\Sigma}^{-1}, \quad \lambda = (m, n, p, c), \tag{4.19}$$

only requiring the inversion of a 3 by 3 matrix with a closed form solution which is well suited to real-time applications. The state vector mean and covariance are updated through:

$$\bar{\boldsymbol{\lambda}} = \boldsymbol{\lambda} + \mathbf{K}_\lambda \boldsymbol{y}, \quad \bar{\mathbf{P}}_\lambda = (\mathbf{I} - \mathbf{K}_\lambda \mathbf{H}_\lambda)\mathbf{P}_\lambda, \quad \lambda = (m, n, p, c) \tag{4.20}$$

4.2.5 Prediction

The state transition of $\boldsymbol{p}$ follows from *Newton's* equations of motion. Here we aim to take advantage of our knowledge that subject motion is relatively smooth. The position state is therefore augmented with velocity and acceleration vectors allowing for the following linear prediction model:

$$\boldsymbol{p} = \mathbf{F}_p \bar{\boldsymbol{p}} + \boldsymbol{q}_p,$$

where,

$$\mathbf{F}_p^{9\times 9} = \begin{pmatrix} 1 & 0 & 0 & \Delta t & 0 & 0 & \frac{\Delta t^2}{2} & 0 & 0 \\ 0 & \ddots & 0 & 0 & \ddots & 0 & 0 & \ddots & 0 \end{pmatrix}, \quad \boldsymbol{p} = \begin{pmatrix} x & y & z & \mid & \dot{x} & \dot{y} & \dot{z} & \ddot{x} & \ddot{y} & \ddot{z} \end{pmatrix}^\mathsf{T}, \tag{4.21}$$

and $\boldsymbol{q}_p$ represents the uncertainty in the predicted position state. The measurement matrix $\mathbf{H}_p$ of equation 4.16 is padded with zeros. Ideally the accelerometer would be used in the construction of the measurement matrix, however, sequence specific gradient interactions and biases are similar in magnitude to the real accelerations expected. As a result there is little benefit in incorporating accelerometer measurements into the position prediction or measurement model for the particular sensor used in the construction of the WRAD. The prediction uncertainty ($\boldsymbol{q}_p$) is modelled with the following covariance matrix:

$$\mathbf{Q}_p = \int \mathbf{F}_p \mathbf{Q}_a \mathbf{F}_p^\mathsf{T} \mathrm{d}t, \quad \mathbf{Q}_a = \sigma_p^2 \begin{pmatrix} \mathbf{0}^{6\times 6} & \mathbf{0}^{3\times 3} \\ \mathbf{0}^{3\times 3} & \mathbf{I}^{3\times 3} \end{pmatrix}, \tag{4.22}$$

where σ_p represents the uncertainty in the change in acceleration of the WRAD frame. The state vector $\boldsymbol{n}$ is augmented with the term ω_z that represents the angular rate of change about the z-axis (the static magnetic field). The state transition can then be approximated through:

$$\boldsymbol{n} = \mathbf{F}_n \bar{\boldsymbol{n}} + \boldsymbol{q}_n, \quad \mathbf{F}_n = \begin{pmatrix} 1 & 0 & -n_1 \Delta t \\ 0 & 1 & n_0 \Delta t \\ 0 & 0 & 1 \end{pmatrix}, \quad \boldsymbol{n} = \begin{pmatrix} \cos(\beta) & \sin(\beta) & | & \omega_z \end{pmatrix}^{\mathsf{T}}. \tag{4.23}$$

In this case the uncertainty in the predicted state ($\boldsymbol{q}_n$) is modelled with the covariance matrix:

$$\mathbf{Q}_n = \mathbf{J}_n \left(\int \mathbf{F}_\omega \mathbf{Q}_\omega \mathbf{F}_\omega^{\mathsf{T}} \mathrm{d}t \right) \mathbf{J}_n^{\mathsf{T}},$$

where,

$$\mathbf{J}_n = \frac{\partial \boldsymbol{n}}{\partial(\beta, \omega)} = \begin{pmatrix} -n_0 n_2 \Delta t - n_1 & -n_1 \Delta t \\ -n_1 n_2 \Delta t + n_0 & n_0 \Delta t \\ 0 & 1 \end{pmatrix}, \quad \mathbf{Q}_\omega = \sigma_\omega^2 \begin{pmatrix} 0 & 0 \\ 0 & 1 \end{pmatrix}, \quad \mathbf{F}_\omega = \begin{pmatrix} 1 & \Delta t \\ 0 & 1 \end{pmatrix}. \tag{4.24}$$

The term σ_ω is the uncertainty in the change of angular velocity. The WRAD incorporates a 3 axis angular rate sensor, however (similar to the accelerometer) it adds little confidence to the orientation states due to gradient disturbances that are challenging to model. The gradient mechanical offset $\boldsymbol{o}$ and static-gradient field misalignment $\boldsymbol{m}$ are expected to be constant. The prediction of these states are then:

$$\boldsymbol{o} = \bar{\boldsymbol{o}} + \boldsymbol{q}_o, \quad \text{and} \quad \mathbf{m} = \bar{\boldsymbol{m}} + \boldsymbol{q}_m. \tag{4.25}$$

Noise is injected into the system through the terms $\boldsymbol{q}_o$ and $\boldsymbol{q}_m$ that describe the confidence in this stationary assumption. They are modelled with the following covariance matrices:

$$\mathbf{Q}_o = \sigma_o^2 \mathbf{I}, \quad \text{and} \quad \mathbf{Q}_m = \sigma_m^2 \mathbf{I}. \tag{4.26}$$

4.2.6 Filter overview

Referring to Figure 4.2, the low noise observation of the direction of the static magnetic field ${}^{L}\boldsymbol{b}$ is used to transform the [3D pickup coil] potential into the intermediate frame ${}^{M'}_{L}\mathbf{R}$ (Eq. 4.5). The [slew field model] (Eq. 4.9) is used to generate the encoding matrix $\mathbf{S}$ and mechanical bias vector $\boldsymbol{c}$. Next the [measurement matrices are updated] $\mathbf{H}_{m,n,p,c}$ (Eq. 4.16) using the previous state estimates, encoding matrix and bias vector. Then the state vectors are corrected through the standard linear Kalman update Eqns

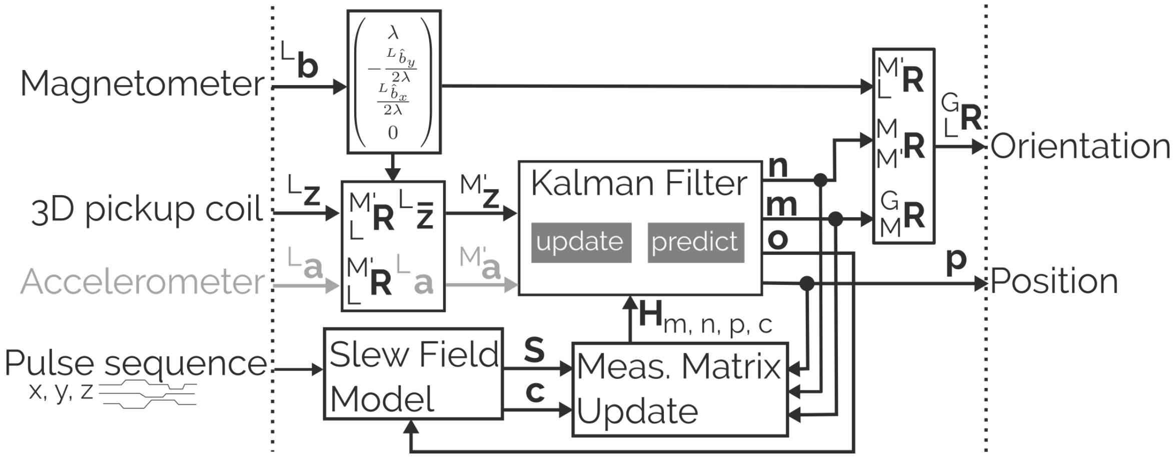

Fig. 4.2 A flow chart summarising the proposed algorithm.

4.18-4.20. The magnetometer derived transform $^{M'}_{L}\mathbf{R}$, z axis rotation $^{M'}_{M}\mathbf{R}$ and bias rotation $^{G}_{M}\mathbf{R}$ are combined to give the transform between the WRAD and gradient coordinate frames. The filter state $\boldsymbol{p}$ is the position in the gradient coordinate frame. The WRAD incorporates an accelerometer that can measure the direction of the earth's gravitational field in the local coordinate frame. This can be used as an additional observation of the filter state $\boldsymbol{n}$, as shown in Appendix A, however it was found that this adds little improvement to orientation tracking performance, hence it is shown disabled (greyed-out).

4.2.7 Pulse sequence design

The WRAD detects the RF pulse in the parent pulse sequence and then waits until the start of the sinusoidal playouts (Figure 4.3) that are inserted before the imaging readout of each line of k-space. It then samples the potential across each pickup coil during each sinusoidal pulse (32 points per sinusoid, per pickup coil, at 200 kHz). An in-line single bin discrete *Fourier* transform (DFT) is applied to the signal recursively as each point is sampled (*Goertzel* filter) centred at the pulse frequency (6.25 kHz) so that the result is ready almost immediately after the last sample point:

$$\mathscr{F}_{\omega}\left(^{L}\boldsymbol{z}\right) = {}^{L}\bar{\boldsymbol{z}}e^{i\theta},$$

in which the angle θ represents any timing offsets between the gradient and WRAD time frames. The amplitude from the DFT is free from potential sources of bias, such as an offset caused by angular rate of change (Eq. 4.12) and eddy currents. The 'pre-filtered' waveform amplitude vector ($^{L}\bar{\boldsymbol{z}}$) for each readout is used to update the *Kalman*

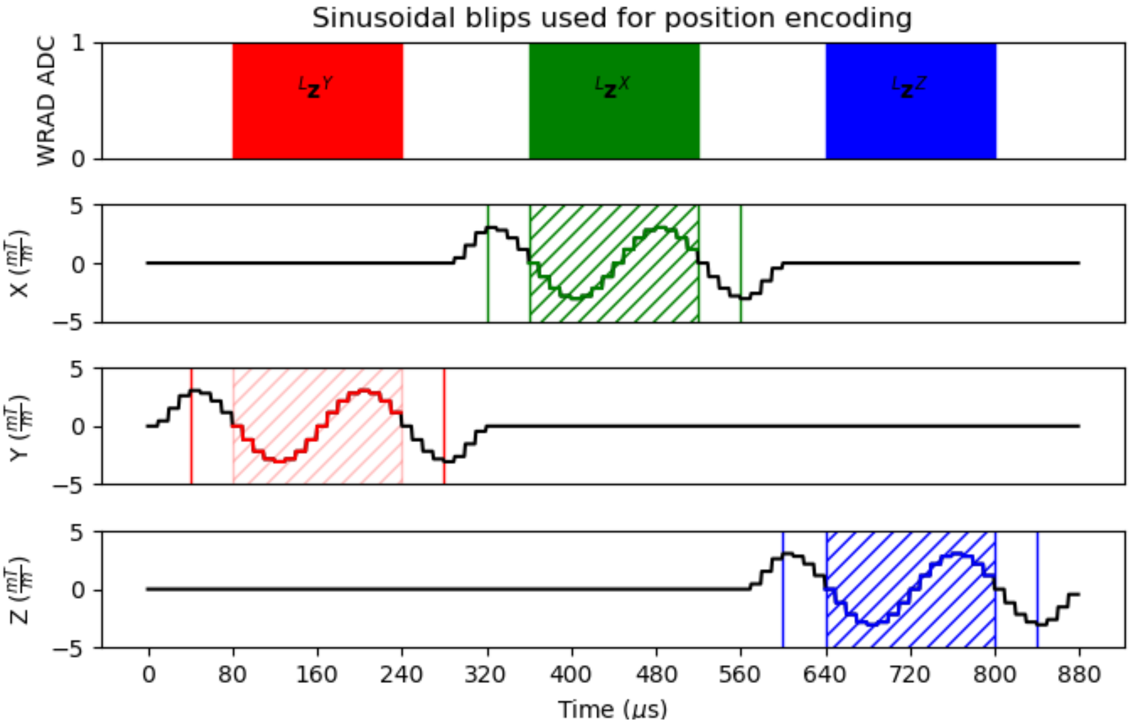

Fig. 4.3 Pulse sequence waveforms added before the first readout of the parent pulse sequence. The sinusoidal waveforms are in the gradient frame and remain fixed during the entire image acquisition.

filter (Figure 4.2). The gradient pulse shapes (Figure 4.3):

$$g(t) = -A\sin(\omega t), \quad \dot{g} = A\omega\cos(\omega t),$$

are also Fourier transformed ($\mathscr{F}_\omega(\dot{g}) = A\omega \ = s$) to produce the slew vector encoding matrices $\mathbf{S}^{x-z}$ and mechanical offset vectors $\boldsymbol{c}^{x-z}$ (Eq. 4.9) for each of the readouts:

$$\mathbf{S}^x = s\begin{pmatrix} 0 & 0 & 1 \\ 0 & 0 & 0 \\ 1 & 0 & 0 \end{pmatrix}, \quad \boldsymbol{c}^x = s\begin{pmatrix} 0 \\ 0 \\ o^x_z \end{pmatrix}; \quad \mathbf{S}^y = s\begin{pmatrix} 0 & 0 & 0 \\ 0 & 0 & 1 \\ 0 & 1 & 0 \end{pmatrix}, \quad \boldsymbol{c}^y = s\begin{pmatrix} 0 \\ 0 \\ o^y_z \end{pmatrix};$$

and,

$$\mathbf{S}^z = s\begin{pmatrix} -\frac{1}{2} & 0 & 0 \\ 0 & -\frac{1}{2} & 0 \\ 0 & 0 & 1 \end{pmatrix}, \quad \boldsymbol{c}^z = s\begin{pmatrix} o^z_x \\ o^z_y \\ 0 \end{pmatrix}; \tag{4.27}$$

4.2.8 Experiments

State Estimation

The modular nature of the filter allows the states to be independently disabled/enabled. To test the filter's efficacy at tracking biases, a sample dataset was acquired during which the subject lay motionless in the scanner. An artificial bias rotation was then used to transform the magnetometer data causing a misalignment between the gradient frame and static magnetic field. The efficacy of the filter could then be evaluated by observing its ability to return to its original position and orientation states and to track the bias transform with the state vector $\boldsymbol{m}$ that models this transform $\left({}^{G}_{M}\mathbf{R}\right)$.

Encoding pose with two gradients

The encoding matrix presented in Eq. 4.9 suggests that only the z gradient is required for 3D position encoding (*Helmholtz/Maxwell Pair*) if the orientation of the local/sensor frame with respect to the gradient frame is known. The slew vector is also used to encode the orientation state $\boldsymbol{n}$ about the axis of the static magnetic field $\left({}^{M'}_{M}\mathbf{R}\right)$. It was therefore of interest to evaluate the efficacy of the filter to track both position and the remaining degree of freedom in orientation using only two unique gradient playouts, an optimisation typically not possible in MR signal based techniques. The X and Y gradient coils (*Golay*) produce planar vector fields that encode z displacement orthogonal to the static magnetic field. This is useful for the orientation state encoding, but only when the z displacement is non-zero. The Z gradient forms a unique field that encodes the orientation state for all positions in the scanner except on the intersection of the planes $x = 0$ and $y = 0$ (a line, concentric with the bore). For the test dataset the WRAD was purposefully moved through the $z = 0$ plane, where the X and Y gradient coils give little useful information about the orientation state of the WRAD. The filter was then applied to the data using different coil pairs. It was expected that combining the Z gradient with the X or Y gradients (as opposed to using the similar X and Y gradients only) would give the best performance.

In Vivo Scans

An imaging protocol was adapted from one currently used in studies of brain morphometry. It consisted of a non-selective 3D spoiled multi-echo gradient echo pulse sequence with 1 mm^3 isotropic resolution and twofold GRAPPA acceleration. In total 7 echoes were acquired using high bandwidth (650 Hz/pixel) bipolar readouts at a

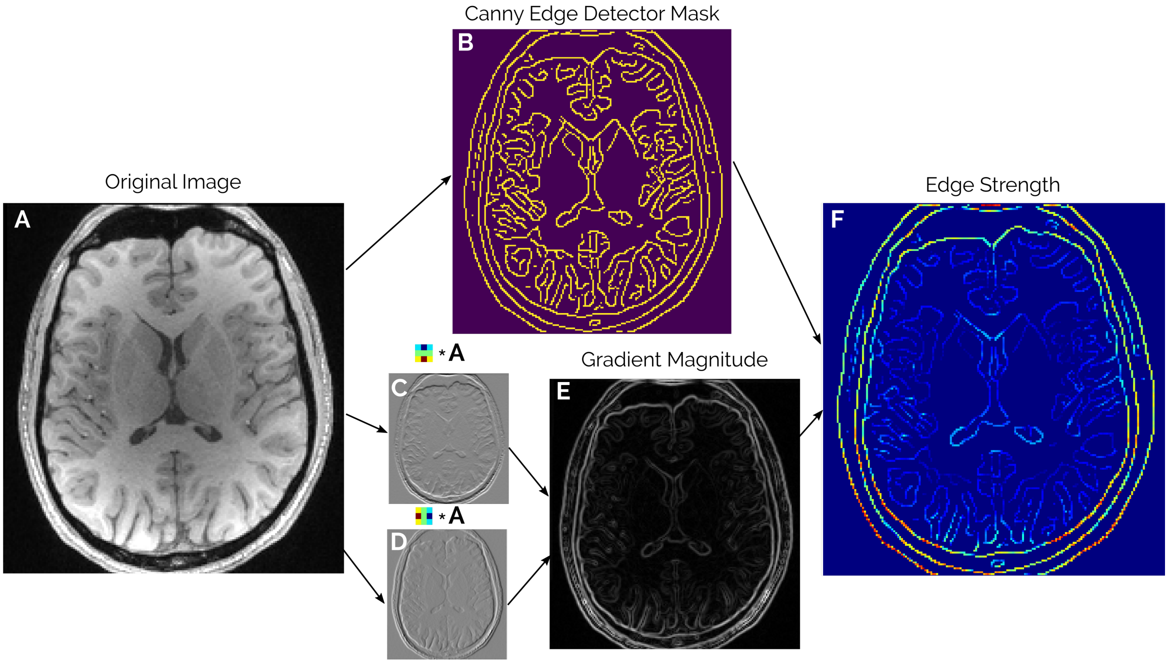

Fig. 4.4 A graphical representation of the Average Edge Strength (AES) calculation that was used as an image quality metric. Images C and D are the result of a convolution of the original image with the (3 by 3) X and Y gradient operators (*Sobel-Feldman*). Image E is the pixel-wise $\mathbf{L}^2$ norm of C and D. F is the result of masking E with the Boolean image B. B is calculated using the Canny edge detection algorithm. Finally, the AES is determined by taking the mean of the non-zero pixel values in F $\left(\frac{\sum \mathrm{F}}{\sum \mathrm{B}}\right)$.

repetition time of 20 ms. The orientation and position were calculated and transmitted out of the scanner bore before the first readout for each line of k-space. The pose estimates were applied to the following line of k-space, resulting in a latency of less than 20 ms with an update rate of 50 Hz. The echoes were combined for display by calculating the pixel-wise root mean squares.

The images of three subjects are presented. All three subjects were scanned on a 3 T Siemens Skyra using the 20-channel head/neck coil according to protocols that had been approved by the Faculty of Health Sciences Human Research Ethics Committee of the University of Cape Town. Acquisitions were repeated in each subject for no motion and motion conditions, and in each case with prospective motion correction (moco) on and off. Firstly, for Subject A, the correction of involuntary motion is shown. Next, in Subject B, the correction of moderate motion associated discomfort is evaluated. Finally, in Subject C, the correction of frequent strong motion is presented.

The WRAD was mounted on the bridge of the subject's nose using a 3D printed bracket (Figure 4.1). Due to the 32 channel head coil's compact design the WRAD could not fit on the subject's nose without making contact with the mask-like anterior coil set, this could lead to spurious readings. The WRAD was mounted on the bridge of the subject's nose using a 3D printed bracket. Two, approximately 16 mm^2, pieces of weak (spongy) double sided tape (1 mm thick) mounted on the inner surface of the bracket (one on each side) were used to fix the WRAD to the subject. We found that the natural oils of the subject's skin meant the glue did not adhere well, however, the tape offered a clean surface and the 'spongy-softness' improved comfort. The subjects were then placed in the 20 channel head and neck receive coil for image acquisitions. For the first 20 lines of k-space the filter gains were increased and no updates were applied to allow the filter bias states to converge.

The Average Edge Strength (AES) metric [39] was used to compare changes in image quality. The image volumes from the different acquisitions of each subject are first co-registered into the same 'halfway' space [31], after which the AES is calculated as shown in Figure 4.4. The Canny edge detection algorithm was run on the uncorrected 'no move' scan for Subject A and Subject C and on the 'no move' corrected scan for Subject B, because this subject moved a large amount during the first scan with correction off. One edge map is therefore defined for each subject. This reduced sensitivity to changes in tuning of the Canny detection algorithm and allowed better comparison to the highly corrupted scans.

4.3 Results

4.3.1 Filter State Estimation

The first column of Figure 4.5 shows an example data snippet where a subject lay motionless during the image acquisition; notice the typical z-axis drift. In the second and third columns a 2 degree bias rotation about the gradient x-axis was introduced at 5 seconds. With the filter state m disabled the transform introduces considerable biases into the position and orientation states (Column 2). When enabled, the filter tracks the transform (Row 3, Column 3). Once stabilised the position and orientation states are very close to those shown without a bias (Column 1), indicating robustness to deviations of the two coordinate frames. The gradient mechanical offset states are strongly influenced by whether or not the bias state is enabled, because without the bias state the remaining residual can only be explained by mechanical offsets. The offsets estimated with the bias tracking enabled are expected to be more accurate because they don't deviate if the underlying bias has changed (Row 3, Column 4).

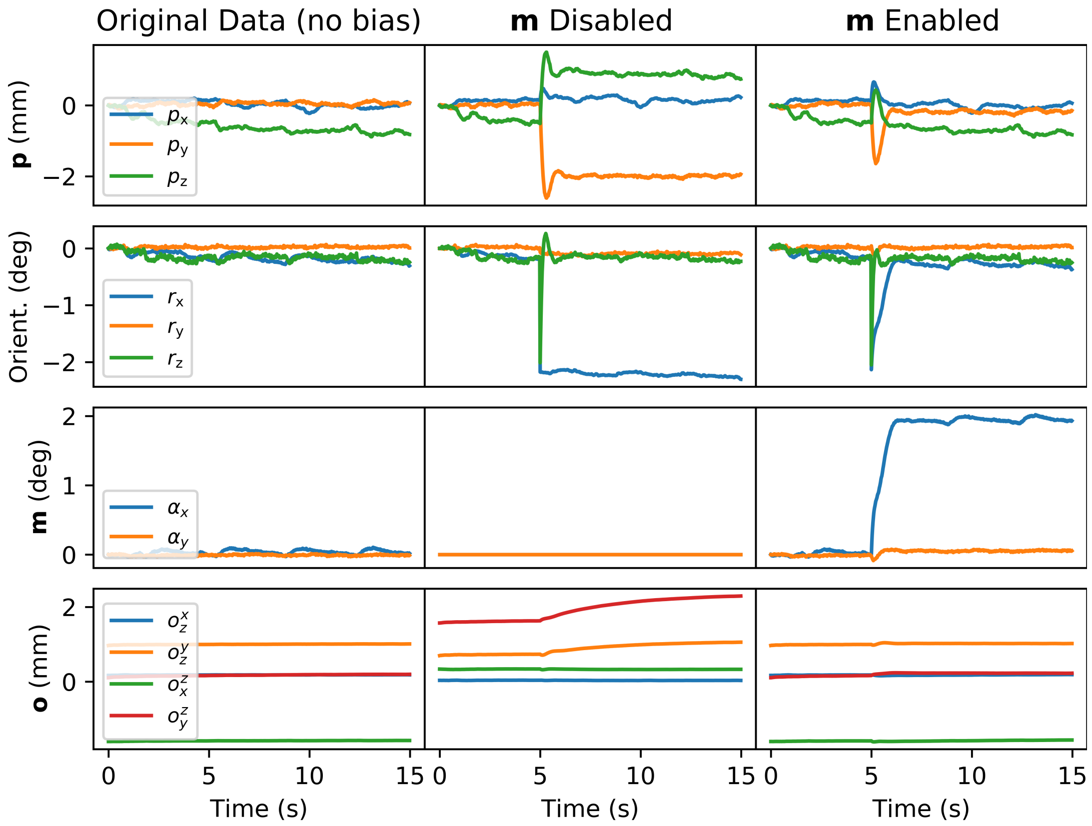

Fig. 4.5 (Column 1) State data captured by the WRAD as a patient lay still during an image acquisition. (Columns 2-3) At 5 seconds a 2 degree bias rotation about the MRI scanner x-axis is introduced into the magnetometer measurements that simulates a deviation between the static magnetic field and gradient co-ordinate frames, which is tracked by the filter state $\boldsymbol{m}$ (Row 3). (Column 2) Tracking of the bias state ($\boldsymbol{m}$) is disabled. (Column 3) The bias tracking is enabled. The top two rows are the position $\boldsymbol{p}$ and orientation of the WRAD. The state $\boldsymbol{o}$ (Row 4) models constant offsets (mechanical misalignments) of the gradient axes.

4.3.2 Pose estimates using only two gradients

The first column of Figure 4.6 is a reference dataset in which all 3 readouts are used. As was expected, in the case where only the X and Y gradient readouts are used (Column 2), the orientation estimates become unreliable when the z displacement is very small (Column 2, Row 2 [r_z-green]). By combining the two different gradient coil types (*Golay* and *Helmholtz/Maxwell Pair* [XZ], Column 3) the problem is overcome allowing reliable pose estimates with similar precision to when all 3 gradients are used. In all cases there is sufficient pulse diversity for reliable position estimates. The reduced number

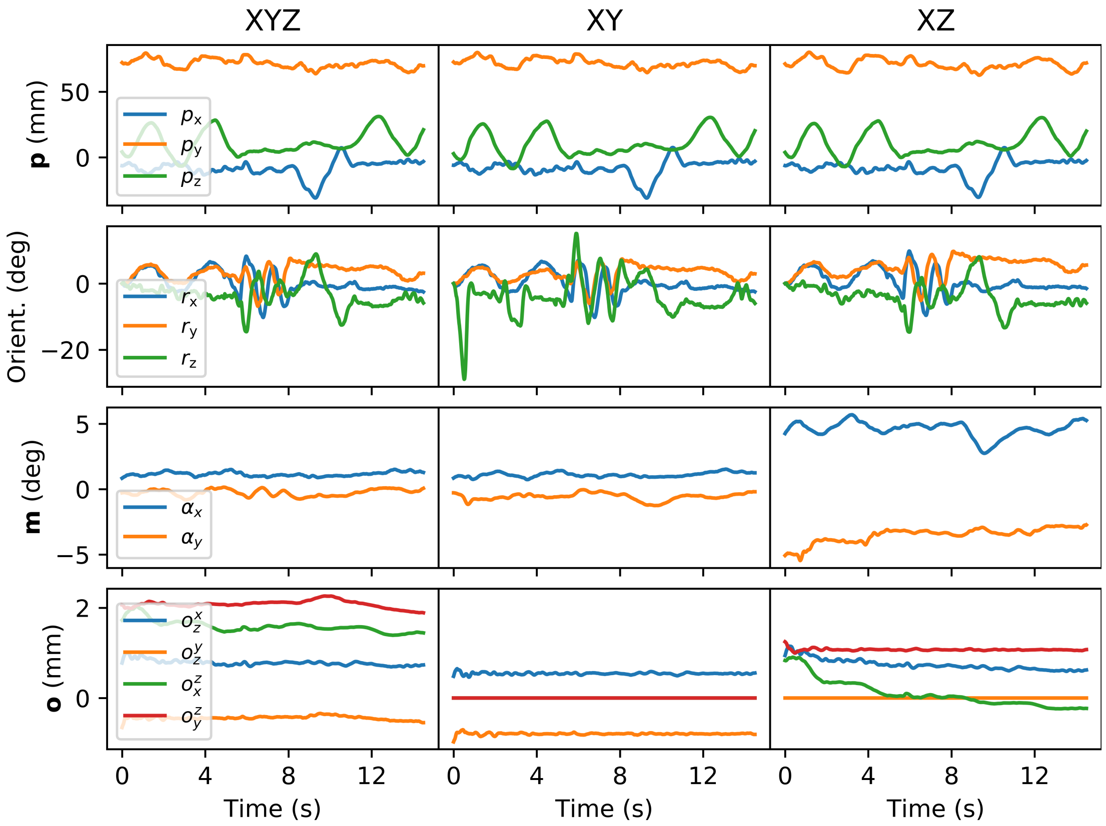

Fig. 4.6 Comparison of position ($\boldsymbol{p}$) and orientation state (r_z) obtained using two gradient play-outs instead of three; data captured with a TR of 10 ms (100 Hz). (Column 1) All gradient axes (x, y and z). (Column 2) Only the *Golay* coils (x and y). (Column 3) The x and z gradients. The third and fourth rows are the orientation and mechanical bias states.

of readouts does however influence the bias state tracking performance, because the system becomes less constrained.

4.3.3 Involuntary Motion

Due to the head coil construction the subjects drifted predominantly in the x (left-right) direction when asked to remain as still as possible. In all subjects it was found that applying feedback resulted in visibly improved edge quality irrespective of how much motion had occurred during the image acquisition. Figure 4.7 shows an example dataset where the subject moved very little. For this acquisition an average increase in AES of 4.5 % over all of the slices was achieved when motion correction was applied. The largest image improvement was in the frontal regions of the brain where the ‘lever-arm’ effect is greatest for subtle rolling movements. This is most visible on the

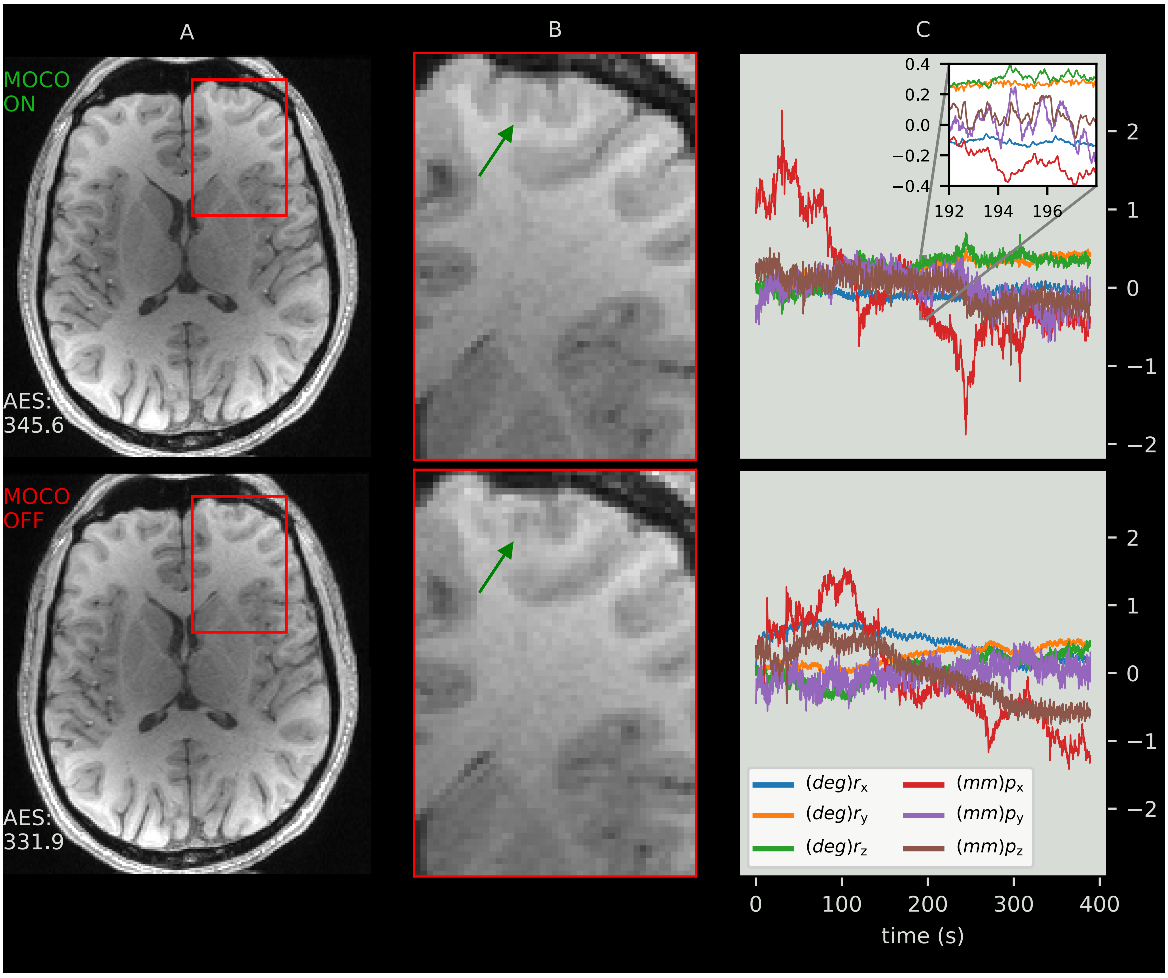

Fig. 4.7 Data captured from Subject A who moved in a way that is representative of typical involuntary motion. (Top row) shows motion correction on. (Bottom row) shows motion correction off, with measurement still active. (Column A) is a central coronal slice from the 3D volume. (Column B) is a zoomed view of each image, green arrows show finer cortical folding. (Column C) Motion data plotted relative to their respective means for better visualisation on the same axes. The orientation is in rotation vector form.

fine cortical folding (green arrows). For all the ‘no move’ scans, motion corrections resulted in higher SNR in homogeneous regions as well as improved edge sharpness. The motion data used to correct the volume for this subject were calculated without the y-gradient readout, reducing the pulse sequence insert duration to 600 μs (Figure 4.3). This is less than a third of the acquisition time (2 ms) used to acquire a typical FID navigator [42] and a tenth of the time required to acquire a collapsed fat navigator [8].

4.3.4 Deliberate Motion

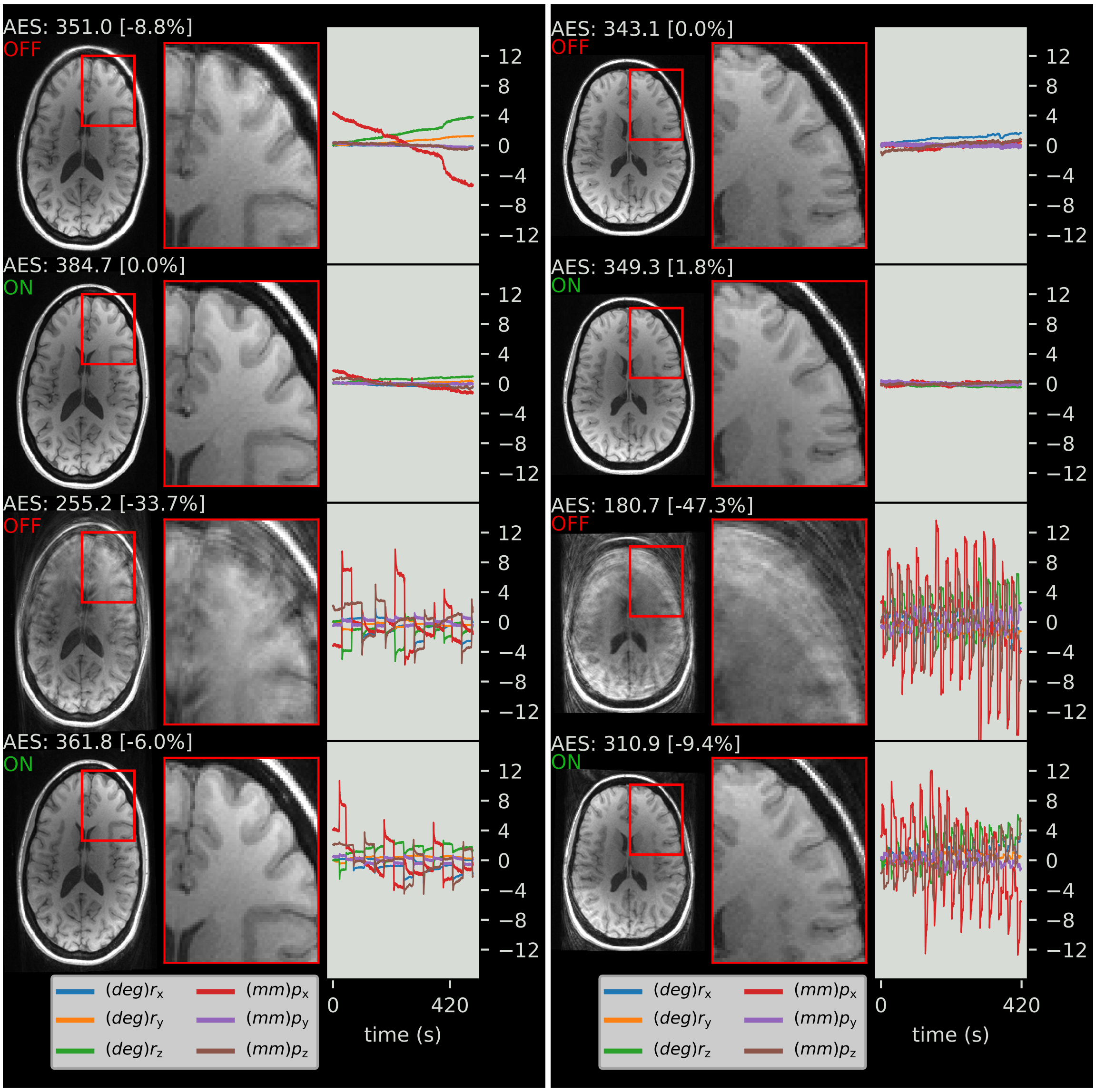

(a) Subject B - Moderate Motion

(b) Subject C - Severe Motion

Fig. 4.8 In the top two rows the subjects were asked to remain as still as possible. For the next two rows the subjects were asked to move. For the first and third rows motion correction was turned off. For the second and last rows motion correction was turned on.

Correcting larger motion is more challenging because the accuracy of the pose estimates becomes more important. In the current implementation the only calibration required is to determine the scaling factor κ in Eq. 4.11. This term is the relation between induced voltage and spatial encoding, and is expected to be similar with respect to different MRI scanners, to within the accuracy of the WRAD's pose estimates. This is therefore considered a device (WRAD) specific calibration. The bias states are designed to track scanner/sensor imperfections that cause the fields to deviate from the linear slew vector field model. Figure 4.8 shows example slices from two acquisitions during which the subjects performed deliberate motion. In Figure 4.8a the subject performed a series of small movements associated with discomfort. This included moving their limbs, adjusting their shoulders or attempting to see more of the magnet bore, all resulting in small head movements. The extreme motion profile of Figure 4.8b is atypical (approximately 90 pose changes > 8 mm), but is useful for showing the advantage of high temporal resolution prospective motion correction. The frequent strong movements combined with the slow cushion recovery meant this subject was almost continuously moving. In both cases the images acquired without motion correction (OFF) are severely corrupted. Temporal smoothing of the filter states is achieved through the prediction step. By reducing the magnitude of the uncertainty in the acceleration σ_p and the angular rate σ_ω of the local frame, it is possible to reduce the variance in the position and orientation states at the expense of reduced temporal response (filter 'smugness'). The *Goertzel* filtered 3D pickup coil measurements are very stable and as a result the measurement standard deviation could be set to 0.2 mm for $\sigma_\parallel$ and 0.15 mm for $\sigma_\perp$ (Equation 4.14), allowing the prediction uncertainties (for all the data presented) to be set to relatively large values of 20 mm$^3/s^3$ and 10 degrees/s^2 for σ_p and σ_ω respectively, while maintaining the precision required to improve image clarity in the involuntary motion scans.

4.4 Discussion

This new method of combining vector observations of the rate of change of the gradient field and the static magnetic field provides an efficient, with respect to required gradient pulse diversity, way of determining position and orientation within an MRI scanner. High enough precision was achieved to improve image quality even in still subjects. The measurements are also accurate enough to make the implemented gradient echo pulse sequence robust to moderate motion associated with subject discomfort. Finally, data were presented that is representative of severe motion, where a vast improvement in image quality was achieved, although the image was not completely free of motion artefacts.

The extra dimension of gradient spatial/vectorial encoding accessible through the use of a 3D pickup coil results in the pose of the device being over constrained in the gradient frame. To this end a linear *Kalman* filter was developed to fuse the measurements and reduce variance. In the filter design, deviations in the scaling of the measured vector potentials are explained as a small rotation between the gradient frame z-axis and direction of the static magnetic field. To explain constant biases a model of the effects of mechanical misalignment of the gradient axes is introduced. Neither of these parameters are measured directly, but are instead observed by the proposed filter. It can be appreciated that the actual underlying offsets represented by these states are challenging to measure and validate, because the selected mechanical offsets would have no influence on the image encoding and the deviation of the coordinate frames would result in very small spatial distortions. It is important to note that the mechanical bias states have no influence on the interpretation of what has been referred to as the 'conventional' z spatial encoding used for image formation, but instead model biases of the non-z spatial encoding relative to the z spatial encoding that can not be explained by a rotation between the magnet and gradient coordinate frames.

In the current implementation the prediction model is mostly used for temporal smoothing with a naive view of how the filter states evolve. In the prototype design an inertial measurement unit (IMU) was included specifically with state prediction in mind, however it was found that the particular digital sensors used were vulnerable to gradient activations. The WRAD's ability to synchronise to the pulse sequence and detect gradient slews suggests that high bandwidth analogue (or digital with externally trigger-able ADCs) accelerometers and angular rate sensors could be sampled during periods of gradient inactivity for improved signal integrity. This sampling scheme has been successfully implemented with the magnetometer even though the influence of the gradients on this measurement are very small. Low noise angular rate and acceleration measurements will enable more robust bias state estimation (through the gravity reference) and increased sensitivity (with better state prediction).

The WRAD hardware can be significantly reduced in size, and with it the size of the apparatus the subject must wear, because only one marker is required for orientation tracking. It is expected that similar performance could be achieved with a pickup coil area reduction of 16 times with the same amplifier and filter circuits.

The current pulse sequence insert is very short (880 μs) and has advantages such as inter-gradient delay estimates and high precision. To extend this technique to be pseudo self navigating, causes of biases such as angular rate of change and eddy currents would be need to be considered. With respect to the hardware, these initial results show that intelligent markers (like the WRAD) could enable plug and play, cable-free prospective motion correction without scanner specific calibration.

Chapter 5

Conclusion

5.1 Discussion

In this research an easy to use motion measurement method has been developed by taking advantage of low-cost embedded electronics. This has enabled accessible high temporal resolution prospective motion correction using external hardware. A single small wireless device was designed and constructed that can be attached to a subject and used immediately to precisely track their pose without any scanner specific calibration. The most intuitive way to achieve cross-calibration free motion measurement is to encode the subject position using the gradient fields because they define the spatial encoding of the image. The fact that the static magnetic field is much stronger (approximately 10 000 times) than the the gradient fields makes measurement of the gradient spatial encoding difficult. One of the most precise techniques for measuring magnetic field strength is through nuclear magnetic resonance. MRI scanners are specifically designed for this purpose, however this entangles the image acquisition with the pose measurement because NMR requires an RF excitation to create the signal. NMR methods also require a minimum of three unique gradient amplitudes to encode position and give little information about the direction of the magnetic field. As a result the measurement of orientation is indirect.

Alternatively, measuring the superposition of magnetic fields within the imaging volume using the Hall effect was proposed. The Hall effect requires a current carrying conductor and as a result is more susceptible to thermal noise. This technique is therefore less precise than NMR, however it is directional. Three, preferably mutually orthogonal, Hall effect sensors therefore enable the precise measurement of the magnetic field direction. It was shown that a vector observation from a three axis Hall effect magnetometer can be used as a stable vector reference during image acquisitions. This is because the gradient activations have a negligible influence on the direction of the superposition of magnetic fields. The magnetometer observation can be combined with an observation from three axis accelerometer and angular rate sensors to precisely determine the orientation of a single small device. This method is independent of the imaging pulse sequence and accurate enough for prospective motion correction without scanner specific calibration. The new method (VectOrient) is capable of quantifying orientation directly which enables higher bandwidths (> 300 Hz) than existing techniques. This could enable very low latency pulse sequence updates if direct access to the gradient amplifier mixing was made possible. The measurements are robust because there are no limitations on the measurement range and the variance is well defined because it is insensitive to external factors. This method is precise enough to track tiny changes in orientation of the subject's head that are likely caused by pressure fluctuations in their carotid arteries [43]. This could be useful at high field strengths where electrocardiograms (ECG) become less reliable. There is however a delay in this signal relative to the (ECG) R wave that could be a challenge for cardiac gating where inter-beat variability makes R wave prediction from the movement data challenging. It is however expected that this signal would be useful in the analysis of BOLD fMRI data of the brain or for binning of data during continuous cardiac imaging.

To measure patient position using the gradient spatial encoding, the precision limitations of Hall sensors and complexity of NMR approaches were overcome by measuring the rate of change of the gradient magnetic fields. Precise planar coils were constructed by taking advantage of printed circuit board manufacturing techniques. Three printed circuit boards were designed to fit into each other, allowing a very low cross-axial sensitivity (0.01%), ensuring accurate measurements of the amplitude and direction of the change in magnetic flux vector.

An important factor that still needed to be addressed is synchronisation to the pulse sequence time domain to allow correct interpretation of the induced voltages. This was achieved by rectifying the potential induced by the imaging pulse sequence RF pulses in a small resonant circuit. The high reliability of the RF pulse detection and 2.4 GHz radio link allowed a close to perfect analogue to digital conversion (ADC) and feedback rate, missing zero packets during almost all of the 3D gradient echo acquisitions presented, each of which contained tens of thousands of lines. The stability of the RF pulse detection was validated to less than a microsecond by inserting sinusoidal gradient waveforms into the imaging pulse sequence. The analysis of the voltage waveforms is done in real time and is ready for transmission within a few microseconds of the last sample point. An added benefit of the sinusoidal pulse sequence series is that it enables inter gradient delay measurements. These measurements can be used to address the distortions caused by adjusting the orientation of the field of view in EPI or non-cartesian pulse sequences. For these sequences data are acquired during gradient slews. A change in orientation results in a different linear combination of the gradients each with a different lead/lag that modifies the k-space trajectories. This is especially important when calibration data is required for image reconstruction.

The current pickup coil excitation sequence can be inserted anywhere in the pulse sequence (independent of RF) and can be made very short (600 μs) making it suitable for a variety of pulse sequences. Although sequence independence is attractive there are advantages to having purpose built gradient pulses. The variance in the motion detection is independent of the pulse sequence parameters and the waveform design can be used to measure other parameters like inter-gradient delay.

The rate of change of flux is a vector, where the amplitude and direction encode information about the pose of the device in the gradient coordinate frame. The vector is shown to be stable to within 0.1 degrees when sampling a gradient waveform for only 160 μs. Position estimates stable to within 0.1 mm are also possible, however, they are strongly influenced by any biases in the orientation measurement. To overcome this challenge a Kalman filter was developed that tracks bias states that explain deviations between the over constrained pickup coil and magnetometer measurements. This filter can be extended to combine information from different sensors to further improve robustness. In the current design the RF detection circuit can be easily modified to be a wireless active (NMR) marker. Combining the signal obtained from the marker during the sinusoidal pulses with the current vector observations could be an interesting extension of the presented Kalman filter.

This new vector based approach to prospective motion correction has shown promising results, improving the average edge strength in all images/volumes irrespective of how much the subject moved. Those who are ill depend the most on MRI for the correct diagnosis, yet they are the most likely to move. With further miniaturisation and smarter battery management we believe that this technique could make the transition from the lab to the clinic, where high frequency prospective motion correction would have the largest impact.

5.2 Future work

Existing low cost micro-electromechanical (MEMS) sensors are influenced by gradient activations which makes the detection of subtle motion challenging. To this end synchronised sampling of high bandwidth sensors during periods of gradient in-activity could be a solution. Recent improvements in MEMS technologies have allowed for the development of high-bandwidth accelerometers capable of detecting mechanical vibrations for audio recording which would be well suited to this application.

The electronics developed in this work are not limited to measuring signals relating to the subject's pose and can be used in a variety of other applications that would benefit from accurate synchronisation to the gradient activations, especially when combining MRI with positron emission tomography, electroencephalography or ultrasound. A current restriction on the minimum marker size is related to the size of the battery, however the energy usage is small (120 mW). With a design optimised for size, similar dimensions to existing optical markers (15 mm x 15 mm) should be possible with a battery life of approximately 3 hours. Alternatively, wireless power transfer could be explored. 11 W power transfer has been achieved with a decoupled coil operating at 10 MHz [44], however this does increase the complexity of the MR hardware set-up and miniaturisation may be challenging. The 'passive' nature of an energy harvesting approach is however attractive, and could help in translating this method to a clinical setting.

References

[1] Jalal B. Andre et al. “Toward Quantifying the Prevalence, Severity, and Cost Associated With Patient Motion During Clinical MR Examinations”. In: *J Am Coll Radiol* 12.7 (2015), pp. 689–695. ISSN: 1558349X. DOI: 10.1016/j.jacr.2015.03.007.

[2] James G. Pipe. “Motion correction with PROPELLER MRI: Application to head motion and free-breathing cardiac imaging”. In: *Magnetic Resonance in Medicine* 42.5 (1999), pp. 963–969. ISSN: 0740-3194. DOI: 10.1002/(SICI)1522-2594(199911)42:5<963::AID-MRM17>3.0.CO;2-L.

[3] Ola Norbeck et al. “Simultaneous multi-slice combined with PROPELLER”. In: *Magnetic Resonance in Medicine* 80.2 (2018), pp. 496–506. ISSN: 07403194. DOI: 10.1002/mrm.27041.

[4] Daniel Gallichan, José P. Marques, and Rolf Gruetter. “Retrospective correction of involuntary microscopic head movement using highly accelerated fat image navigators (3D FatNavs) at 7T”. In: *Magnetic Resonance in Medicine* 75.3 (2016), pp. 1030–1039. ISSN: 07403194. DOI: 10.1002/mrm.25670.

[5] Nathan White et al. “Prospective Real-Time Correction for Arbitrary Head Motion Correction in MRI using Image-based Tracking”. In: *Magnetic Resonance in Medicine* 63.1 (2010), pp. 91–105. DOI: 10.1002/mrm.22176.PROMO.

[6] M Dylan Tisdall et al. “Volumetric navigators for prospective motion correction and selective reacquisition in neuroanatomical MRI.” In: *Magnetic resonance in medicine* 68.2 (2012), pp. 389–99. ISSN: 1522-2594. DOI: 10.1002/mrm.23228.

[7] Aaron T Hess et al. “Real-time motion and B0 corrected single voxel spectroscopy using volumetric navigators.” In: *Magnetic Resonance in Medicine* 66.2 (2011), pp. 314–23. ISSN: 1522-2594. DOI: 10.1002/mrm.22805.

[8] Mathias Engström et al. “Collapsed fat navigators for brain 3D rigid body motion”. In: *Magnetic Resonance Imaging* 33.8 (2015), pp. 984–991. ISSN: 0730-725X. DOI: 10.1016/J.MRI.2015.06.014.

[9] J. Andrew Derbyshire et al. “Dynamic scan-plane tracking using MR position monitoring”. In: *Journal of Magnetic Resonance Imaging* 8.4 (1998), pp. 924–932. ISSN: 10531807. DOI: 10.1002/jmri.1880080423.

[10] S. Umeyama. “Least-squares estimation of transformation parameters between two point patterns”. In: *IEEE Transactions on Pattern Analysis and Machine Intelligence* 13.4 (1991), pp. 376–380. ISSN: 01628828. DOI: 10.1109/34.88573.

[11] Melvyn B Ooi et al. "Prospective motion correction using inductively coupled wireless RF coils." In: *Magnetic Resonance in Medicine* (2013). ISSN: 1522-2594. DOI: 10.1002/mrm.24845.

[12] Alexander Aranovitch et al. "Prospective motion correction with NMR markers using only native sequence elements". In: *Magnetic Resonance in Medicine* 79.4 (2018), pp. 2046–2056. ISSN: 07403194. DOI: 10.1002/mrm.26877.

[13] M Zaitsev et al. "Magnetic resonance imaging of freely moving objects: prospective real-time motion correction using an external optical motion tracking system." In: *NeuroImage* 31.3 (2006), pp. 1038–50. ISSN: 1053-8119. DOI: 10.1016/j.neuroimage.2006.01.039.

[14] Julian Maclaren et al. "Navigator accuracy requirements for prospective motion correction". In: *Magnetic Resonance in Medicine* 63.1 (2009), NA–NA. ISSN: 07403194. DOI: 10.1002/mrm.22191.

[15] Julian Maclaren et al. "Prospective motion correction using coil-mounted cameras: Cross-calibration considerations". In: *Magnetic Resonance in Medicine* 79.4 (2018), pp. 1911–1921. ISSN: 07403194. DOI: 10.1002/mrm.26838.

[16] Jens Anders et al. "Integrated active tracking detector for MRI-guided interventions". In: *Magnetic Resonance in Medicine* 67.1 (2012), pp. 290–296. ISSN: 07403194. DOI: 10.1002/mrm.23112.

[17] Erez Nevo. *Method and apparatus to estimate location and orientation of objects during magnetic resonance imaging*. 2003.

[18] Julian Maclaren et al. "Measurement and Correction of Microscopic Head Motion during Magnetic Resonance Imaging of the Brain". In: *PLoS ONE* 7.11 (2012), pp. 3–11. ISSN: 1932-6203. DOI: 10.1371/journal.pone.0048088.

[19] Maxim Zaitsev, Julian Maclaren, and Michael Herbst. "Motion artifacts in MRI: A complex problem with many partial solutions". In: *Journal of Magnetic Resonance Imaging* 42.4 (2015), pp. 887–901. ISSN: 10531807. DOI: 10.1002/jmri.24850.

[20] Michaela Soellinger et al. "3D cine displacement-encoded MRI of pulsatile brain motion". In: *Magnetic Resonance in Medicine* 61.1 (2009), pp. 153–162. ISSN: 07403194. DOI: 10.1002/mrm.21802.

[21] A J W van der Kouwe, Thomas Benner, and Anders M Dale. "Real-Time Rigid Body Motion Correction and Shimming Using Cloverleaf Navigators". In: *Magnetic Resonance in Medicine* 1019-1032.56 (2006), pp. 1019–1032. DOI: 10.1002/mrm.21038.

[22] Tobias Kober et al. "Head motion detection using FID navigators." In: *Magnetic Resonance in Medicine* 66.1 (2011), pp. 135–43. ISSN: 1522-2594. DOI: 10.1002/mrm.22797.

[23] Maximilian Haeberlin et al. "Real-Time Motion Correction Using Gradient Tones and Head-Mounted NMR Field Probes". In: *Magnetic Resonance in Medicine* 660.74 (), pp. 647–660. DOI: 10.1002/mrm.25432.

[24] Benjamin Zahneisen et al. "Fast noniterative calibration of an external motion tracking device." In: *Magnetic Resonance in Medicine* 71.4 (2014), pp. 1489–500. ISSN: 1522-2594. DOI: 10.1002/mrm.24806.

[25] Jessica Schulz et al. “An embedded optical tracking system for motion-corrected magnetic resonance imaging at 7T”. In: *Magnetic Resonance Materials in Physics, Biology and Medicine* 25.6 (2012), pp. 443–453. ISSN: 0968-5243. DOI: 10.1007/s10334-012-0320-0.

[26] B. Armstrong et al. “RGR-3D: Simple, Cheap detection of 6-DOF Pose for Tele-Operation, and Robot Programming and Calibration”. In: *Proceedings 2002 IEEE International Conference on Robotics and Automation (Cat. No.02CH37292)* 3.May (2002). ISSN: 10504729. DOI: 10.1109/ROBOT.2002.1013678.

[27] Robert Mahony, Tarek Hamel, and Jean-Michel Pflimlin. “Nonlinear Complementary Filters on the Special Orthogonal Group”. In: *IEEE Transactions on Automatic Control* 53.5 (2008), pp. 1203–1218. ISSN: 0018-9286. DOI: 10.1109/TAC.2008.923738.

[28] Sebastian O H Madgwick, Andrew J L Harrison, and Ravi Vaidyanathan. “Estimation of IMU and MARG orientation using a gradient descent algorithm”. In: *IEEE International Conference on Rehabilitation Robotics* (2011). ISSN: 19457898. DOI: 10.1109/ICORR.2011.5975346.

[29] F.L. Markley. “Attitude Determination Using Vector Observations and the Singular Value Decomposition”. In: *Journal of the Astronautical Sciences* 36.3 (1988), pp. 245–258.

[30] Yan Liu et al. “Novel Calibration Algorithm for a Three-Axis Strapdown Magnetometer”. In: *Sensors* 14.5 (2014), pp. 8485–8504. ISSN: 1424-8220. DOI: 10.3390/s140508485.

[31] Martin Reuter, H. Diana Rosas, and Bruce Fischl. “Highly accurate inverse consistent registration: A robust approach”. In: *NeuroImage* 53.4 (2010), pp. 1181–1196. ISSN: 10538119. DOI: 10.1016/j.neuroimage.2010.07.020.

[32] Mat A. Bernstein et al. “Concomitant gradient terms in phase contrast MR: Analysis and correction”. In: *Magnetic Resonance in Medicine* 39.2 (1998), pp. 300–308. ISSN: 07403194. DOI: 10.1002/mrm.1910390218.

[33] Kevin F. King et al. “Concomitant gradient field effects in spiral scans”. In: *Magnetic Resonance in Medicine* 41.1 (1999), pp. 103–112. ISSN: 0740-3194. DOI: 10.1002/(SICI)1522-2594(199901)41:1<103::AID-MRM15>3.0.CO;2-M.

[34] C. A. Baron et al. “The effect of concomitant gradient fields on diffusion tensor imaging”. In: *Magnetic Resonance in Medicine* 68.4 (2012), pp. 1190–1201. ISSN: 07403194. DOI: 10.1002/mrm.24120.

[35] David G. Norris and James M.S. Hutchison. “Concomitant magnetic field gradients and their effects on imaging at low magnetic field strengths”. In: *Magnetic Resonance Imaging* 8.1 (1990), pp. 33–37. ISSN: 0730-725X. DOI: 10.1016/0730-725X(90)90209-K.

[36] P.L. Volegov et al. “On concomitant gradients in low-field MRI”. In: *Journal of Magnetic Resonance* 175.1 (2005), pp. 103–113. ISSN: 1090-7807. DOI: 10.1016/J.JMR.2005.03.015.

[37] Jaakko O. Nieminen and Risto J. Ilmoniemi. “Solving the problem of concomitant gradients in ultra-low-field MRI”. In: *Journal of Magnetic Resonance* 207.2 (2010), pp. 213–219. ISSN: 1090-7807. DOI: 10.1016/J.JMR.2010.09.001.

[38] A Van Niekerk, A Van Der Kouwe, and E Meintjes. “A method for measuring orientation within a magnetic resonance imaging scanner using gravity and the static magnetic field (VectOrient)”. In: *IEEE Transactions on Medical Imaging* 36.5 (2017), pp. 1129–1139. ISSN: 1558254X. DOI: 10.1109/TMI.2017.2652502.

[39] Murat Aksoy et al. “Hybrid prospective and retrospective head motion correction to mitigate cross-calibration errors”. In: *Magnetic Resonance in Medicine* 67.5 (2012), pp. 1237–1251. ISSN: 07403194. DOI: 10.1002/mrm.23101.

[40] Nicola De Zanche et al. “NMR probes for measuring magnetic fields and field dynamics in MR systems”. In: *Magnetic Resonance in Medicine* 60.1 (2008), pp. 176–186. ISSN: 07403194. DOI: 10.1002/mrm.21624.

[41] Roberto G. Valenti, Ivan Dryanovski, and Jizhong Xiao. “A linear Kalman filter for MARG orientation estimation using the algebraic quaternion algorithm”. In: *IEEE Transactions on Instrumentation and Measurement* 65.2 (2016), pp. 467–481. ISSN: 00189456. DOI: 10.1109/TIM.2015.2498998.

[42] Tess E. Wallace et al. “Head motion measurement and correction using FID navigators”. In: *Magnetic Resonance in Medicine* (2018). ISSN: 07403194. DOI: 10.1002/mrm.27381.

[43] Pierre Levan et al. “Ballistocardiographic artifact removal from simultaneous EEG-fMRI using an optical motion-tracking system”. In: (2013). DOI: 10.1016/j.neuroimage.2013.02.039.

[44] Kelly Byron et al. “An RF-gated wireless power transfer system for wireless MRI receive arrays”. In: *Concepts in Magnetic Resonance Part B: Magnetic Resonance Engineering* 47B.4 (2017), e21360. ISSN: 15525031. DOI: 10.1002/cmr.b.21360.

Appendix A

Using the earth's gravitational field to update the orientation state.

The WRAD includes a 3 axis accelerometer which measures the acceleration of the WRAD frame (${}^{G}\boldsymbol{a}^{l}$) and a constant bias acceleration (${}^{G}\boldsymbol{a}^{b}$, predominantly due to the earth's gravitational field) in the local frame:

$$ {}^{L}\boldsymbol{a} = {}^{L}_{G}\mathbf{R}\left({}^{G}\boldsymbol{a}^{b} + {}^{G}\boldsymbol{a}^{l}\right) \tag{A.1} $$

as in Van Niekerk, Van Der Kouwe, and Meintjes [38] the earth's gravitational field ($\boldsymbol{g}$) can be assumed to lie normal to the scanner bed, which due to the scanner's construction is closely aligned to the gradient y-axis. Due to slight magnetism of the micro electro mechanical system (MEMS) sensor we also expect a slight bias ($\boldsymbol{a}^{s}$) in the direction of the static magnetic field so that:

$$ {}^{G}\boldsymbol{a}^{b} = \boldsymbol{g} + {}^{G}_{M}\mathbf{R}\,{}^{M}\boldsymbol{a}^{s} = g\begin{pmatrix}0\\1\\0\end{pmatrix} + {}^{G}_{M}\mathbf{R}a\begin{pmatrix}0\\0\\1\end{pmatrix}, \tag{A.2} $$

The high frequency gradient disturbances of the accelerometer are of a similar magnitude to the small accelerations the subject is likely to undergo, both with a mean value of 0. We therefore incorporate both of these terms into the uncertainty ($\boldsymbol{w}_{a}$) of the measurement rather than attempting to model them. As with the pickup potential measurement, it is beneficial to transform the acceleration observation into the intermediate reference frame (${}^{M'}\cdot$):

$$ {}^{M'}_{M}\mathbf{R}^{M}_{G}\mathbf{R}^{L}\boldsymbol{a} = {}^{M'}\boldsymbol{a} = {}^{M'}_{M}\mathbf{R}^{M}_{G}\mathbf{R}\boldsymbol{g} + {}^{M'}\boldsymbol{a}^{s} = \boldsymbol{a}_{\perp} + \boldsymbol{a}_{\parallel} = g\begin{pmatrix}-n_1\\ n_0\\ 0\end{pmatrix} + \begin{pmatrix}0\\ 0\\ a - m_0 g\end{pmatrix} \tag{A.3} $$

A light-weight update equation for the z-axis orientation state ($\boldsymbol{n}$) is then possible using the perpendicular component of the rotated acceleration vector measurement:

$$ \frac{\boldsymbol{a}_{\perp}(x,y)}{g} = \mathbf{H}_{a}\boldsymbol{n} = \begin{pmatrix}0 & -1\\ 1 & 0\end{pmatrix}\boldsymbol{n} \tag{A.4} $$

The accelerometer uncertainty is modelled as normally distributed Gaussian noise with covariance matrix:

$$ \mathbf{\Sigma}_{a} = \sigma_{a}^{2}\begin{pmatrix}1 & 0\\ 0 & 1\end{pmatrix} \tag{A.5} $$